

Use Authorization

In presenting this dissertation in partial fulfillment of the requirements for an advanced degree at Idaho State University, I agree that the Library shall make it freely available for inspection. I further state that permission to download and/or print my dissertation for scholarly purposes may be granted by the Dean of the Graduate School, Dean of my academic division, or by the University Librarian. It is understood that any copying or publication of this dissertation for financial gain shall not be allowed without my written permission.

Signature _____

Date _____

**Geologic mapping of the Ashbough Canyon quadrangle and an
investigation of the Basin and Range Blacktail fault,
southwestern Montana**

by

Brandon Crawford

A thesis

submitted in partial fulfillment

of the requirements for the degree of

Master of Science in the Department of Geosciences

Idaho State University

Summer 2017

Committee Approval

To the Graduate Faculty:

The members of the committee appointed to examine the thesis of Brandon M. Crawford find it satisfactory and recommend that it be accepted.

David M. Pearson, Major Advisor

Paul K. Link, Committee Member

Tracy Payne, Graduate Faculty Representative

Acknowledgements

I would like to extend my deepest thanks to my advisor, Dr. David Pearson for always making the time to help me and push me with this research. Thank you for all of your assistance with my writing, discussing hypotheses, providing tips for improving my field and laboratory skills, and continuing to be an enthusiastic and supportive advisor with this project. It is through your help and guidance that I became the strong geoscientist I am today.

I also would like to thank my committee member Dr. Paul Link, for all of the time and effort he has put into assisting me on this project. I thank you for taking the time to edit my thesis and help fine-tune my map for publication. For your assistance in every aspect of this project and invaluable knowledge, you were an integral person of support for this project and for my two years here at Idaho State University.

Thank you to my field assistants Evan Hartshorn and Dan Brennan. Without your help in the field, this project would not have been possible. For talking through hypotheses and helping me stay alive in the Montana wilderness. Your assistance and resulting friendships has been invaluable to me.

Thanks to all of my friends at Idaho State University, who have made these last two years incredible and made me feel as part of the Geology family. Thank you to my partner in crime and my best friend, Nathan Anderson. You've always been extremely supportive of me, and not afraid to call me out on some of my stupid ideas - it has been great! Thank you to Melissa Neiers, Kate Zajanc, and the rest of the office staff for keeping the wheels moving on my project.

Thank you to all of my instructors at Idaho State University for your role in my education, and furthering my knowledge and geologic know-how. Each and every one of you has helped support and shape the scientist I am today, and the outcome of this work. A special thanks to Dr. Glenn Thackray for helping me to understand range front geomorphology and Dr. Mike McCurry for help with petrology and petrography.

A special thank you to Dr. Jesse Mosolf at Montana Bureau of Mines, for assisting in the field and helping me complete my map. I would also like to thank my partner, Kate Wehrs for the late night discussions, endless run-throughs for presentations, edits for my thesis, and for the endless support in getting this thesis finished.

Finally I would like to thank Judy Brown, Nancy Ulrich, and the Matador Cattle Company for graciously allowing me access to their property.

This research was supported by the U. S. Geological Survey, National Cooperative Geologic Mapping Program, under USGS award number G16AC00159, the Geological Society of America, and the Idaho State University Geosciences Geslin fund.

Table of Contents

List of Figures	viii
Abstract	x
Chapter 1: Introduction	1
Chapter II: Geologic Background	9
Previous Mapping.....	9
Basement Framework.....	9
Archean and Paleoproterozoic Rocks of the Sweetwater Hills.....	12
Paleozoic Sedimentary Rocks.....	15
Mesozoic and Early Cenozoic Shortening.....	17
Basin and Range Extension.....	18
Chapter III: Methods	23
Mapping.....	23
Sample Collection.....	24
Hand Samples.....	24
U-Pb Zircon Sample Processing.....	24
(U-Th)/He Apatite Processing.....	26
U-Pb Zircon Geochronology.....	27
(U-Th)/He Apatite Thermochronometry.....	28
Geomorphic Investigations.....	30

Chapter IV: Results	32
Field Mapping.....	32
Ruby Range Gneisses.....	32
Christensen Ranch Metasedimentary Suite.....	32
Quartzofeldspathic Gneiss.....	33
Blacktail Mountains.....	35
Paleozoic Strata.....	35
Devonian.....	40
Mississippian Strata.....	41
Quaternary Sediments.....	44
Structural Geology.....	44
Basement Rocks.....	44
Lombard Limestone Deformation.....	47
Jake Canyon Fault Observations.....	50
Blacktail Fault.....	50
Isotopic Data.....	51
U-Pb Zircon.....	51
15DP-A01.....	51
15DP-A02.....	52
(U-Th)/He Apatite.....	54
Geomorphology.....	56

Chapter V: Discussion	59
Basement Geochronology.....	59
Basement Deformation.....	62
Provenance of the Flathead Sandstone.....	63
Paleozoic Units and Sevier-style Deformation.....	64
Basin and Range Extension.....	65
Jake Canyon Fault Reactivation.....	65
(U-Th)/He Apatite Thermochronometry.....	68
Geomorphic Expression of the Range Front.....	70
Timing of Initial Displacement on the Blacktail Fault.....	72
Chapter VI: Conclusions	72
Works Cited	76
Appendices	88
A. Hand Sample Locations.....	88
B. U-Pb Zircon Data.....	88
C. (U-Th)/He Apatite Data.....	92
Plates	97
Plate 1: Geologic map of the Ashbough Canyon quadrangle	97

List of Figures

Figure 1: General regional map.....	2
Figure 2: Geologic Map of the Ruby Range.....	3
Figure 3: Model for the relationship between Basin and Range and the hotspot...6	
Figure 4: Timing of initial displacement of Basin and Range faults.....	8
Figure 5: Map of basement subprovinces.....	10
Figure 6: Map of the Jake Canyon fault near the mouth of Sheep Creek.....	22
Figure 7: Schematic of (U-Th)/He apatite method.....	30
Figure 8: Schematic diagram of range front geomorphology relative to fault slip.....	31
Figure 9: Photo of folds in the Christensen Ranch Metasedimentary Suite.....	33
Figure 10: Photo of the Quartzofeldspathic Gneiss with an diabase intrusion.....	34
Figure 11: Photo of pegmatite sill intruding the contact between Aqfg and Acr.....	35
Figure 12: Correlation of mapping units.....	36
Figure 13: Photo of the great unconformity.....	38
Figure 14: Photo of Meagher Dolomite cliffs.....	39
Figure 15: Photo of Pilgrim Dolomite cliffs.....	40
Figure 16: Stereogram of foliations in Aqfg.....	45
Figure 17: Photo of isoclinal folds in Aqfg.....	45
Figure 18: Photo of isoclinally folded pegmatite intrusions.....	46
Figure 19: Stereogram of foliations in Acr.....	46
Figure 20: Photograph of folds in Mlb.....	48

Figure 21: Photograph of fault in Mlb.....	49
Figure 22: Stereogram of folds in Mlb.....	49
Figure 23: Concordia plot for sample 15DP-A01.....	52
Figure 24: Relative probability plot for sample 15DP-A02.....	53
Figure 25: Concordia plot for sample 15DP-A02.....	53
Figure 26: Map showing where apatite samples were collected.....	55
Figure 27: Chart of apatite ages vs elevation.....	55
Figure 28: Graphs showing eU vs age.....	57
Figure 29: Google Earth images showing sinuosity of Blacktail Mountains range front.....	58
Figure 30: Schematic figure showing style of Jake Canyon fault reactivation....	67
Figure 31: Schematic figure of range front based on (U-Th)/He apatite data.....	70

Abstract

This work presents a coupled field-based and geo/thermochronological study of rocks exposed in the Ashbough Canyon quadrangle, located in southwestern Montana near the town of Dillon. Mapping and U-Pb zircon geochronology within basement units suggests that the Quartzofeldspathic Gneiss exposed in the Blacktail Mountains and the central Ruby Range intruded into the structurally higher Christensen Ranch Metasedimentary Suite. A detrital U-Pb zircon analysis of the basal middle Cambrian Flathead Sandstone lacks the regionally present ~1780 Ma peak and instead records two Archean peaks at ~2501 Ma and ~2798 Ma; this suggests that the zircons are proximal sourced from nearby basement. The Mississippian Lombard Limestone is strongly deformed above the contact with the undeformed, Mississippian Kibbey Sandstone suggesting that the contact represents a décollement. Mapping in the Lombard Limestone suggests on the basis of disharmonic folding and a lack of faults in fold hinge zones that the unit is primarily deformed via detachment folding.

The northeast-dipping Jake Canyon fault is an early Cenozoic, Laramide-style reverse fault that juxtaposes Archean rocks over Paleozoic rocks near the northeastern range front of the Blacktail Mountains. Within the Ashbough Canyon quadrangle, the Jake Canyon fault was likely reactivated by the Basin and Range Blacktail fault. In the northern part of the map area, field and geomorphic observations of the Blacktail Mountain's range front indicate an active, single fault trace and a rapid to moderate slip rate. In contrast, to the southeast, multiple, synthetic normal faults occur adjacent to the main strand of the Blacktail fault and distributed slip along these faults likely contributes toward a more irregular range front. The along-strike transition in geomorphic expression

of the range front may have been controlled by the pre-existing dip angle of the reactivated Jake Canyon fault. These observations further support that the northwest strike of the Blacktail fault, and perhaps the orientations of some of the dominant faults in the northern Basin and Range, were controlled by older thrust belt structures. Apatite (U-Th)/He data were collected in a sub-vertical transect across the footwall of the Blacktail fault and indicate that rocks have not been exhumed from depths greater than ~3 km. Coupled with field and geomorphic observations, this suggests that the Blacktail fault was recently initiated. This result, combined with geomorphic evidence for rapid slip along the range front, suggests that the Blacktail fault is active and was recently activated. A relatively young activation of the Blacktail fault is consistent with a northward propagation of the Basin and Range province associated with the migration of the Yellowstone hotspot.

Chapter I: Introduction

The Ashbough Canyon quadrangle, located ~12 miles southeast of Dillon, in southwestern Montana (Figure 1), is an excellent location to study regional geologic problems ranging from field relationships among Archean gneisses, overlap of Sevier- and Laramide-style deformation, and active northern Basin and Range extension. This thesis contributes to resolution of these problems via a combination of field mapping within the Ashbough Canyon quadrangle as well as through U-Pb zircon and (U-Th)/He apatite isotopic analysis. Work conducted as a part of this thesis primarily consists of: 1) 1:24,000-scale mapping of the Ashbough Canyon quadrangle (Plate 1), which encompasses the southwestern portion of the Ruby Range (locally known as the Sweetwater Hills) and the northeast-facing, central flank of the Blacktail Mountains (Figures 1 and 2); 2) An apatite (U-Th)/He vertical transect across the central Blacktail Mountains, immediately south of the Ashbough Canyon quadrangle in the footwall of the Blacktail fault; and 3) U-Pb dating of zircons from a quartzofeldspathic gneiss in the southern Ruby Range as well as U-Pb detrital zircon geochronology of the basal sandstone from the Middle Cambrian Flathead Sandstone where it lies nonconformably atop basement rocks.

The southwestern Ruby Range exposes Archean to Paleoproterozoic metamorphic rocks with sedimentary and igneous protoliths. Located in the northwestern corner of the Wyoming craton (Chamberlain et al., 2003), these basement exposures record the Beartooth orogeny (~2.8-2.7 Ga), the Tendoy/Beaverhead orogeny (~2.4-2.5 Ga) (Jones, 2008; Cramer, 2015), and the Big Sky/Great Falls orogeny (~1.86-1.72 Ga) (Harms et al., 2004; Foster et al., 2006; Alcock and Muller, 2012; Condit et al., 2015)

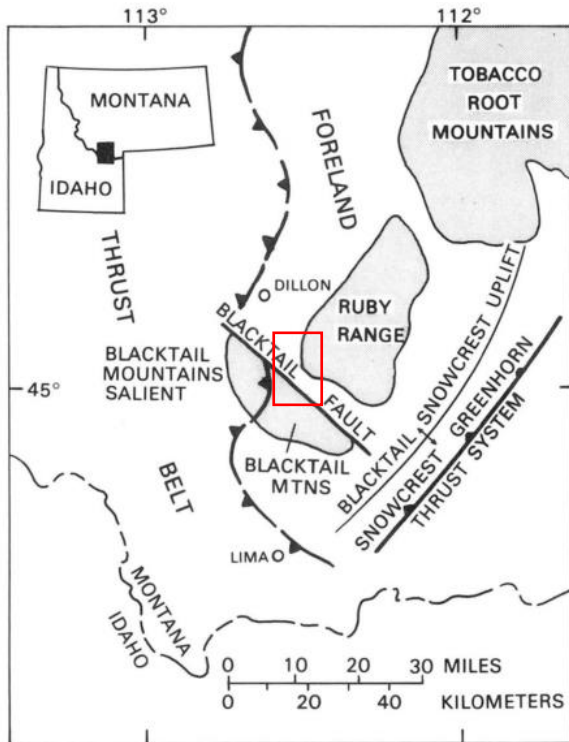


Figure 1: General regional map showing the location of the Ashbough Canyon quadrangle. Location of study area is shown by the red box. (From Tysdal, 1990).

Within the Sweetwater Hills, previous workers identified two metamorphic units that constitute the majority of the map area: the Dillon Granite Gneiss (Heinrich, 1960), and the structurally higher Christensen Ranch Metasedimentary Suite (Garihan, 1979; Karasevich et al., 1981). Various geoscientists have investigated the protoliths of these various gneisses, marbles, and metasedimentary rocks (Figure 2), including Garihan (1979), Karasevich et al. (1981), James and Hedge (1980), and James (1990).

In the Ruby Range, Heinrich (1960) originally mapped primarily quartzofeldspathic gneisses as the Dillon Granite Gneiss. However, later work in the region suggested a sedimentary (Garihan, 1979; Karasevich et al., 1981) or mixed sedimentary and igneous protolith for this unit (James and Hedge, 1980; James, 1990).

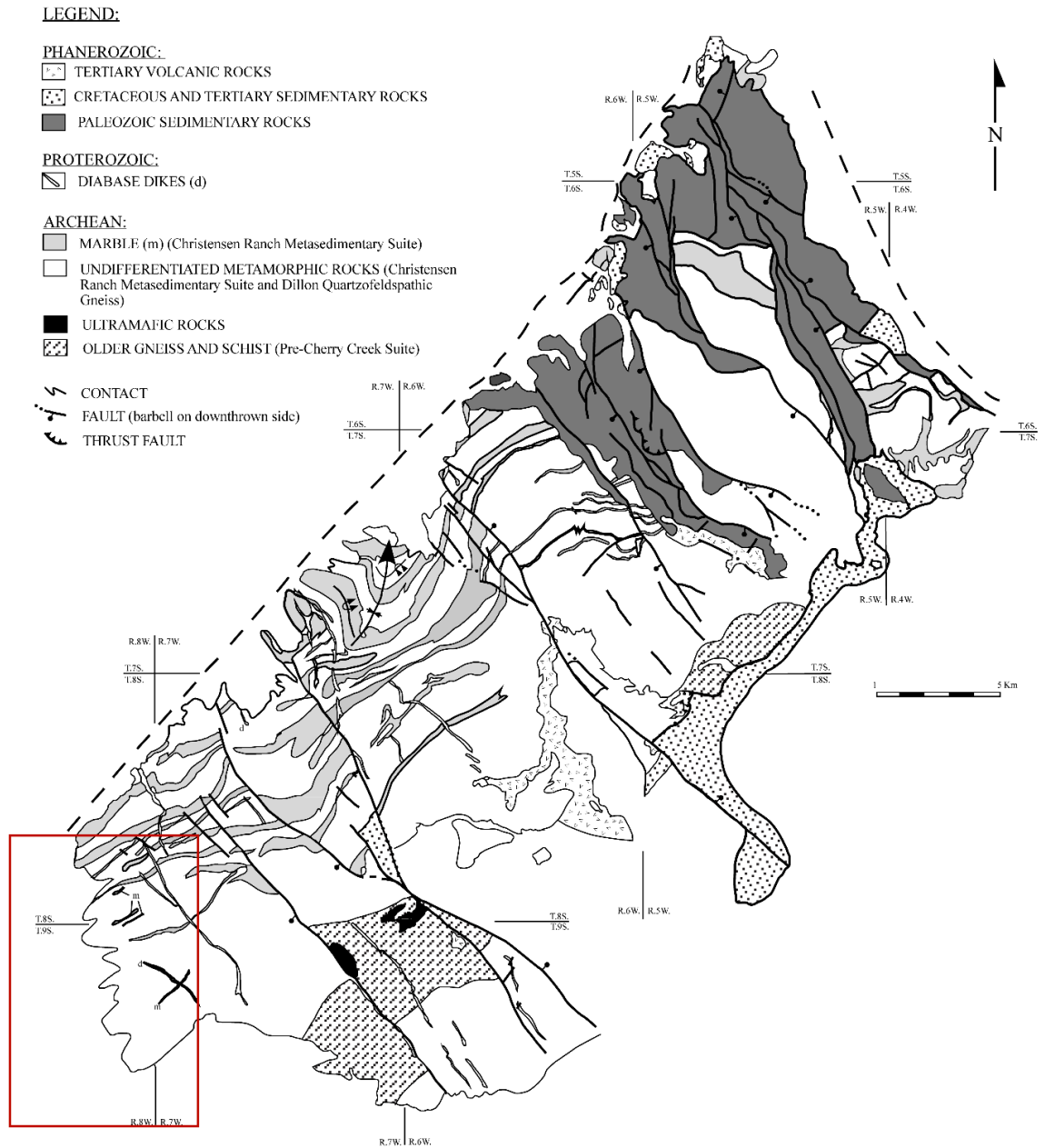


Figure 2: Geologic map of the Ruby Range in southwestern Montana. The Sweetwater Hills, which constitute the northeastern portion of the Ashbough Canyon quadrangle mapped during the present study, is shown in the red rectangle (from Jones, 2008, after Karasevich et al., 1981).

Because of the uncertainty regarding the protolith of this unit, this unit is referred to here as the Quartzofeldspathic Gneiss. Recent work, utilizing U-Pb isotopic dating of zircon

and monazite suggests that the Quartzofeldspathic Gneiss is an ~2770 Ma igneous body that intruded into older Archean country rocks (Jones, 2008; Cramer, 2015). Detailed field mapping conducted here, as well as a U-Pb zircon age from the Quartzofeldspathic Gneiss in Ashbough Canyon, will help evaluate the protolith and age of the Quartzofeldspathic Gneiss, and its field relationship with other basement exposure rocks.

Overlying the Quartzofeldspathic Gneiss in the central Blacktail Mountains is the Cambrian Flathead Sandstone. Regionally consistent detrital U-Pb zircon geochronology from the Flathead Sandstone and correlative middle Cambrian units from northeastern Utah to northern Idaho identified an anomalous ~1780 Ma age peak that is in contrast to Neoproterozoic and early Cambrian rocks along the western Laurentian rift margin that primarily record a Grenville clastic wedge provenance; this represents a major provenance change (Yonkee, 2011; Yonkee et al., 2014). Further work on these middle Cambrian rocks suggests that the ~1780 Ma U-Pb zircon age peak is widespread throughout the northern Rockies (May et al., 2013; Krohe, 2016). However, the source of the ~1780 Ma zircons is unknown. One possibility is that the zircons were derived from 1700-1800 Ma orthogneisses along the northwestern margin of the Wyoming craton in southwestern Montana, potentially from the Ruby Range. In addition, some samples collected from the base of the Flathead Sandstone from Wyoming show an older ~2900 Ma detrital zircon age-peak in addition to a smaller ~1780 Ma peak (May et al., 2013; Malone et al., 2017). This may suggest that lower sandstone records a local basement provenance and stratigraphically higher sandstones record a more distal source. The present work presents U-Pb zircon results from the Archean orthogneiss below the nonconformity as well as the basal portion of the middle Cambrian Flathead Sandstone

within Ashbough Canyon. These results will help evaluate the regional consistency of the Flathead Sandstone provenance as well as evaluate the hypothesis that local basement was a source for the basal Flathead Sandstone.

The Blacktail Mountains, which form a portion of the major, northeast-trending Blacktail-Snowcrest uplift, also expose both Sevier-style (thin-skinned) and Laramide-style (thick-skinned) thrust structures (Pecora, 1981; Tysdal, 1988a). Throughout much of the Sevier fold-thrust belt in Idaho, Utah, and Wyoming, the regional décollement of the Sevier fold-thrust belt occurs within the rheologically weak Cambrian Gros Ventre shale (Royse, 1975). In the Blacktail Mountains, several Cambrian shales are also present (Tysdal, 1988b). However, previous work in the region suggests that these shales did not serve as décollement horizons and that the regional décollement instead occurs at the base of the Mississippian Lombard Limestone (Pecora, 1987; Tysdal, 1988b). The deformation within the Lombard Limestone is thought to represent the frontal portion of the Sevier-style deformation in southwestern Montana (Tysdal, 1988a). This work will evaluate the structural style and extent of shortening in Cambrian to Mississippian rocks, below the hypothesized décollement, to contribute to the regional discussion of the primary factors controlling the style of deformation observed within the frontal-most portion of the Sevier-style deformation.

The Blacktail Mountains are bounded on their northeastern flank by the northeast-dipping, Basin and Range, Blacktail fault. Also exposed in the field area is the steeply northeast-dipping, reverse-slip, Jake Canyon fault (Tysdal, 1988b; Tysdal et al., 1990). Previous work has suggested that in the northwestern Blacktail Mountains, the Blacktail fault reactivates the Jake Canyon fault (Achuff, 1981; Tysdal et al., 1990). However, this

relationship has not been studied in detail within the Ashbough Canyon quadrangle. The current work will better define the geometry of the Blacktail fault and evaluate the hypothesis that it represents partial reactivation of the Jake Canyon fault.

This work also seeks to evaluate the timing of initiation of the Blacktail fault. In east-central-Idaho and southwestern Montana, Basin and Range extension is thought to result from thermal uplift and heating of the lower lithosphere related to the Yellowstone hotspot, which may provide gravitational potential energy that promotes extension (Pierce and Morgan, 2009) (Figure 3). Continued southwestward motion of the North American Plate is predicted to result in extension northwest of the hotspot stops supporting uplifted and heated areas.

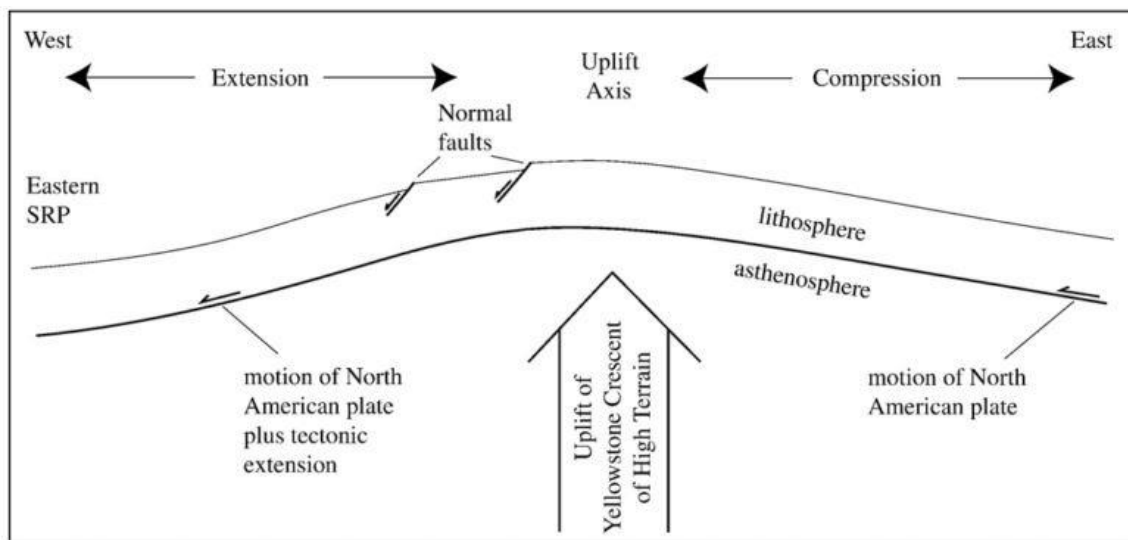


Figure 3: Model showing how uplift related to the Yellowstone hotspot could lead to Basin and Range extension. Uplift from the plume and heating of the lower lithosphere causes the overlying crust to weaken. Extension is induced by gravitational collapse and the continued motion of the North American plate once the plume is no longer supporting the uplifted area. (From Pierce and Morgan, 2009)

The Blacktail fault is located approximately halfway between the Beaverhead and Madison faults, which are estimated to have initiated at ~6 Ma and ~2 Ma, respectively

(Anders, 1994; Pierce and Morgan, 1992, 2009) (Figure 4). Given that the Blacktail fault is located between these faults, it is expected that the fault initiated extensional displacement between ~6 and ~2 Ma. To estimate an initiation age of extension-related exhumation associated with the fault, apatite (U-Th)/He thermochronometry was conducted in a vertical transect along the Blacktail fault's footwall. These results represent one of the first attempts to quantitatively constrain the timing of Basin and Range extension in southwestern Montana.

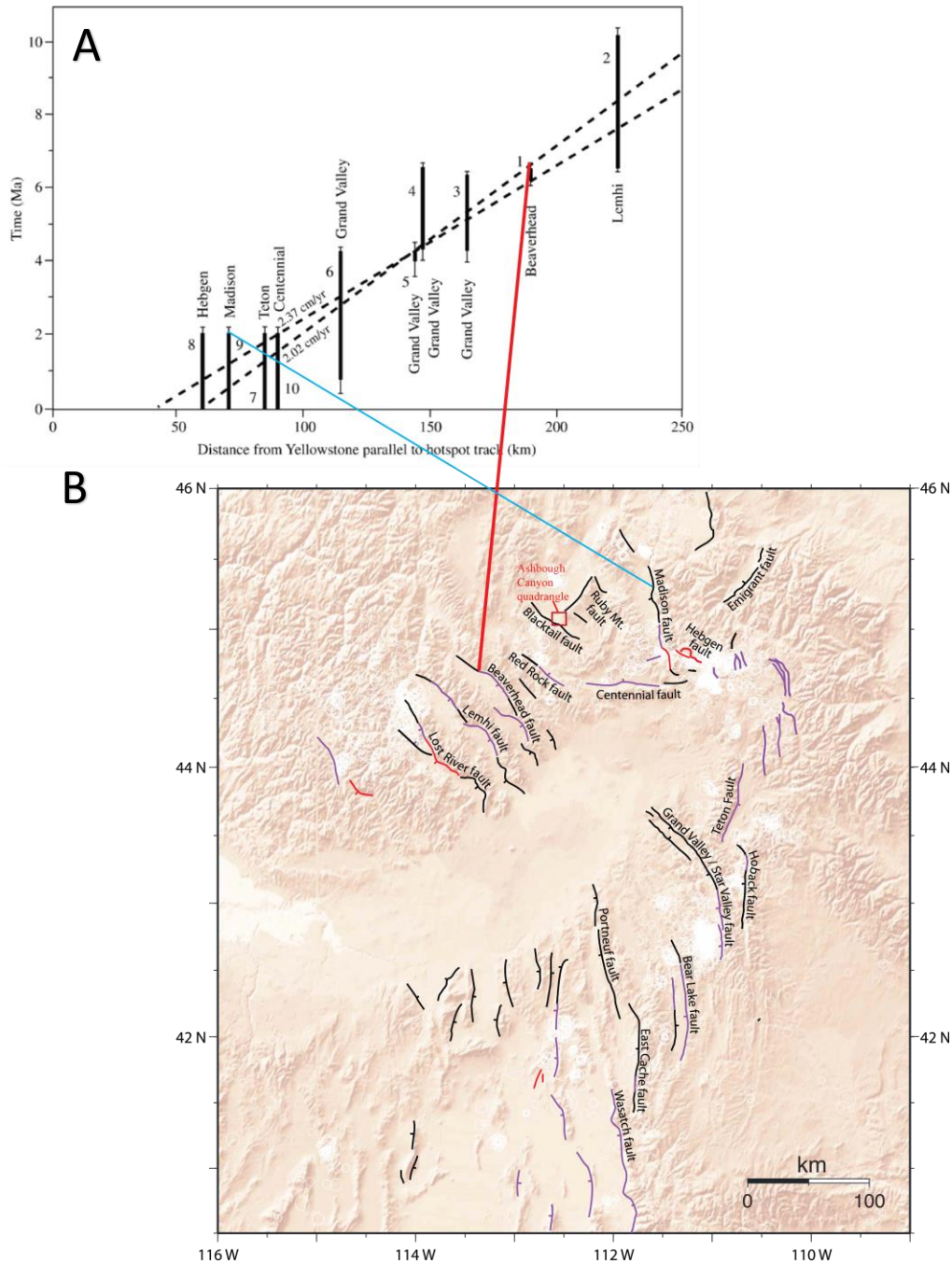


Figure 4: A) Timing of initial displacement on various Basin and Range faults estimated by Pierce and Morgan (2009) (after Anders et al., 1989). B) Map of Basin and Range faults surrounding the Snake River Plain. The Ashbough Canyon quadrangle is highlighted in red. The study area contains the Blacktail fault and is located between the Beaverhead (red line) and the Madison (blue line) faults. Based on the timing of fault activity, the Blacktail fault should have experienced initial offset between ~6 Ma and ~2 Ma. (Figure modified from Pierce and Morgan, 2009; Anders et al., 2014)

Chapter II: Geologic Background

Previous mapping

Portions of the Ashbough Canyon quadrangle have been previously mapped. Most mapping was focused on either basement structure in the Ruby Range, the Sevier-Laramide transition, or Mississippian stratigraphy in the Blacktail Mountains (Garihan, 1979; Achuff, 1981; Karasevich et al., 1981; Pecora, 1981; Wardlaw and Pecora, 1985; Pecora, 1987; Tysdal, 1988b). The mouth of Ashbough Canyon, and the region southeast of the Ashbough Canyon Quadrangle, was mapped by Clark (1987), with a focus on the protolith of the quartzofeldspathic basement exposed in the central and southeastern Blacktail Mountains. The most recent published map containing the entire map area is the 1:250,000-scale, Dillon 1'X2' quadrangle (Ruppel et al., 1993).

Basement Framework

In much of the west-central United States, Archean and Paleoproterozoic basement is obscured by Phanerozoic sedimentary rocks. However, basement rocks are exposed in southwestern Montana in a series of Laramide-style uplifts (Schmidt and Garihan, 1983). These exposures of the basement provide unique insight into the early tectonic history, and the formation of the Wyoming craton, a widespread Archean crustal block. Based on lithology, geochemical signature, and age, the Wyoming craton was subdivided into sub-provinces (Figure 5) (Chamberlain et al., 2003). Much of southwestern Montana, including the Ashbough Canyon quadrangle, is located within the Montana Metasedimentary terrane within the greater Wyoming craton (Foster et al., 2006).

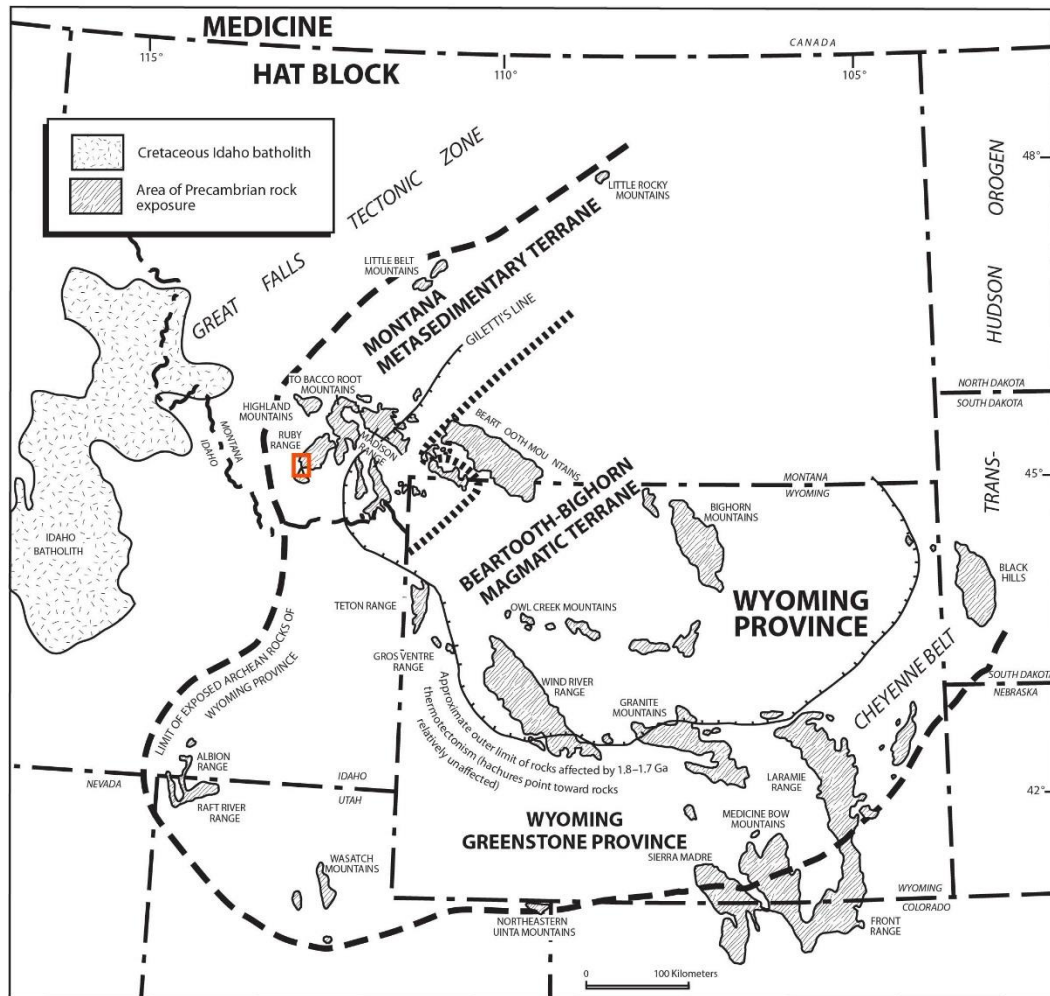


Figure 5: Map of the various subprovinces exposed within the Wyoming craton. Gray areas are locations that Laramide-style deformation has exposed Precambrian basement. Red square indicates the location of the Ashbough Canyon quadrangle (from Harms et al., 2004).

In addition to containing paragneisses, the Montana Metasedimentary terrane also contains deformed quartzofeldspathic gneisses, some of which likely had igneous protoliths (Mogk and Henry, 1988). Adjacent to the Montana Metasedimentary terrane to the southeast is the Beartooth-Bighorn Magmatic terrane (Figure 5), which is defined by ~2900 Ma plutonism (Chamberlain et al., 2003). U-Pb zircon ages from various ranges along the western boundary of the Wyoming craton indicate that other portions of the

basement adjacent to the Montana Metasedimentary province may have initially formed from ~2.4 to 1.8 Ga (Foster et al., 2006). The Montana metasedimentary terrane is distinguished from these magmatic provinces by an abundance of metasedimentary rocks and U-Pb zircon rim and monazite ages indicating that magmatism and metamorphism affected the region from ~2450-2550 Ma (Cheney et al., 2004; Jones, 2008; Harms and Baldwin, 2013; Baldwin et al., 2014; Cramer, 2015; Anderson, 2017). In southwestern Montana, this event has been interpreted to reflect orogenesis and has been variably named the Tendoy/Beaverhead orogeny (Jones, 2008; Cramer, 2015; Baldwin, personal communication, 2017). An episode of magmatism and metamorphism of a similar age was also documented in northern Utah and characterizes the Farmington zone (Mueller et al., 2011). The relationship between the Tendoy/Beaverhead orogeny and Farmington zone is unknown.

Following ~2450 Ma magmatism and metamorphism, initiation of northwest-dipping ocean-continent subduction zone between the Medicine Hat block and Wyoming craton at ~1860-1790 Ma during the Great Falls orogeny resulted in closure of the Medicine Hat Ocean (Foster et al., 2006; Mueller et al., 2016; Anderson, 2017). The magmatic belt related to this closure is oriented roughly northeast-southwest and is known as the Little Belt arc (Foster et al., 2006). Later stages of this convergence, causing most of the metamorphism within the Montana metasedimentary province, is named the Big Sky orogeny and occurred from ~1790-1720 Ma (Harms et al., 2004). Together, the northeast-southwest trending magmatism and metamorphism associated with this episode of orogenesis is called the Great Falls Tectonic zone (O'Neill and Lopez, 1985).

Work in the Ruby Range, using pressure-temperature-time path reconstructions, geochemical data, and petrography, indicate that rocks reached temperatures and pressures equivalent to upper amphibolite- to granulite-facies during peak metamorphism (Demarais, 1981). Based on the presence of cordierite, Garihan (1979) also identified retrograde metamorphism with pressures and temperatures equivalent to greenschist-facies metamorphism. More recent work that also includes geo- and thermo-chronology of monazite and zircon, suggests that prograde metamorphism occurred from ~1790-1760 Ma, and was followed by isothermal decompression and post-orogenic extension at ~1760–1710 Ma (Condit et al., 2015; Cramer, 2015).

Though some diabase dikes within the Ruby Range may have been emplaced at ~1730 Ma on the basis of biotite Ar-Ar dates (Roberts et al., 2002; Brady et al., 2004), some Ar-Ar ages of northeast-southwest trending diabase dikes suggest they were emplaced around ~1400 Ma (Wooden et al., 1978). Alteration of the dolomitic marble in the Christensen Ranch Metasedimentary Suite to talc may have also occurred during this time, which may have been associated with regional rifting associated with early stages of the formation of the Belt basin (Anderson, 1987; Anderson et al., 1990).

Archean and Paleoproterozoic Rocks of the Sweetwater Hills

The southwestern portion of the Ruby Range (locally known as the Sweetwater Hills) contains exposures of quartzofeldspathic and metasedimentary gneiss (Plate 1). The Ruby Range was previously mapped by Garihan (1979) and Karasevich (1981). Most prior workers subdivided the basement exposed in the Ruby Range into three separate units: 1) the structurally lowest Older Gneiss and Schist; 2) the

Quartzofeldspathic Gneiss at structurally intermediate levels; and 3) the structurally highest Christensen Ranch Metasedimentary Suite, which was previously referred to as the Cherry Creek Suite (James, 1990).

Thought to represent some of the oldest rocks in the Ruby Range, mixed orthogneisses, paragneisses, and schists that do not contain either banded iron formations nor marble are referred to by some authors as the Older Gneiss and Schist or Pre-Cherry Creek Group (James and Hedge, 1980; Alcock and Muller, 2012; Alcock et al., 2013). However, recent U-Pb zircon and monazite data have further suggested that the Older Gneiss and Schist in the Ruby Range is not the same as the Pre-Cherry Creek Group observed in the Madison Range (Alcock and Muller, 2012; Alcock et al., 2013). Within the Ruby Range, these rocks are referred to as the Older Gneiss and Schist due to uncertainty regarding the correlation to rocks in the Madison Range and Tobacco Root Mountains (James, 1990). These rocks are exposed immediately east of the current mapping area (Figure 2) (Karasevich, 1981).

Structurally above the Older Gneiss and Schist in the Sweetwater Hills are >4 km thick quartzofeldspathic gneisses that were initially mapped as the Dillon Granite Gneiss (Heinrich, 1949, 1960; Karasevich et al., 1981). These rocks were described as an intensely deformed leucocratic orthogneiss, and garnet-hornblende gneiss with some biotite-, garnet-, and hornblende-rich interlayers. The protolith of these quartzofeldspathic gneisses is uncertain and has been a long standing research focus in the region; for simplicity, the unit is referred to here as the Quartzofeldspathic Gneiss. Early work in the region suggested that the unit represents a primarily granitic intrusion between the Older Gneiss and Schist and structurally higher Christensen Ranch

Metasedimentary Suite to the northwest (Heinrich, 1960). This view shifted as new mapping in the region recognized compositional heterogeneity, structural concordance with adjacent strata on either side of the Quartzofeldspathic Gneiss, and the absence of contact metamorphism in adjacent units (Garihan, 1979). Later work suggested that the Quartzofeldspathic Gneiss's protolith was a package of sandstones stratigraphically below the Christensen Ranch Metasedimentary Suite protolith (Garihan, 1979; Karasevich et al., 1981). However, most workers consider the Quartzofeldspathic Gneiss to have both sedimentary and granitoid protoliths (James and Hedge, 1980; James, 1990). Geochemical analysis of a portion of the Quartzofeldspathic Gneiss in the Blacktail Mountains suggests at least some of it has an igneous protolith (Clark, 1987). Recent U-Pb zircon geochronology suggests that it is primarily a metamorphosed granite that crystallized $\sim 2775 \pm 11$ Ma (Jones, 2008). Metamorphic zircon rims and monazite geochronology suggest that the gneiss was affected by ~ 2450 Ma and ~ 1760 Ma regional metamorphism (Jones, 2008; Cramer, 2015).

Structurally overlying the Quartzofeldspathic Gneiss on the northwest is the Christensen Ranch Metasedimentary Suite, which was initially named the Cherry Creek Group due to the similarities in lithology with rocks exposed in the nearby Tobacco Root Mountains and Madison Range (Heinrich, 1960). The Cherry Creek Group was renamed to the Christensen Ranch Metasedimentary Suite because early studies correlated the unit only on the basis of proximity and the presence of dolomitic marble and banded iron formations in the unit (James, 1990). The unit contains interlayered gneisses, mica schists, marbles, sillimanite-biotite paragneisses, chlorite schists, banded iron formations, and some cross-cutting amphibolite dikes (James and Hedge, 1980). The contact of these

rocks with the underlying quartzofeldspathic gneiss is unknown and debated. The contact is roughly planar and is most likely intrusive, a nonconformity, or a fault. U-Pb zircon and monazite ages indicate that this unit was affected by ~2553-2530 Ma metamorphism (Jones, 2008). The absence of ~2780 Ma monazite ages in these rocks was suggested as evidence that the Christensen Ranch Metasedimentary Suite was deposited between ~2750-2553 Ma, and therefore lies in fault or depositional contact above the Quartzofeldspathic Gneiss (Jones, 2008). However, the limited data constraining the timing of deposition leave open an alternate possibility that will be investigated here: and lithologically similar marbles and schists in both units may indicate that the Quartzofeldspathic Gneiss intruded into the Christensen Ranch Metasedimentary Suite.

Paleozoic Sedimentary Rocks

Prior mapping in the Blacktail Mountains (Pecora, 1981; Tysdal, 1988a) recognized ~600 m of Cambrian rocks that depositionally overlie the Quartzofeldspathic Gneiss. In contrast to the thick Neoproterozoic to early Cambrian stratigraphic section in southeastern Idaho and northern Utah (Link et al., 1993), in the Blacktail Mountains, middle Cambrian Flathead Sandstone directly overlies the Quartzofeldspathic Gneiss. In southwestern Montana, this contact is thought to represent onlapping sediment onto the western Laurentian margin (Sloss, 1950). Recent work, based on similarities in detrital zircon provenance in the context of field data, has suggested that elsewhere, this unconformity represents the last stages of Rodinian rifting as the western margin of Laurentia transitioned into a passive margin (Yonkee et al., 2014).

Detrital zircon studies focused on the Flathead Sandstone and correlative middle

Cambrian units have identified a common regional ~1780 Ma age-peak (May et al., 2013; Yonkee et al., 2014; Krohe, 2016; Malone et al., 2017). The source for this peak is currently uncertain but may be the Yavapai-Mazatzal belts, located to the south in New Mexico and Arizona (Yonkee et al., 2014; Malone and Craddock, 2017). An alternative, local source is possibly the Great Falls Tectonic Zone of southwestern Montana.

In western Wyoming the ~1780 Ma zircon age peak is not expressed in the basal layers of the Flathead Sandstone (May et al., 2013; Malone et al., 2017). Instead, these studies documented prominent Archean-aged zircon peaks, which was interpreted to suggest that they had local sources in the nearby Beartooth-Bighorn Magmatic terrane (Malone et al., 2017) (Figure 5).

Cambrian rocks in eastern Washington, northern Idaho, and southwestern Montana were deposited during cycles along the passive western margin of Laurentia, termed Sauk megasequences (Bush et al., 2012). During these cycles, a sandstone or shale base was deposited as sea level rose and was subsequently overlain by carbonate layers. The Cambrian rocks deposited during these sequences in southwestern Montana have been described in detail by Thomas (2007). The Flathead Sandstone records early deposition of siliciclastic sediment onto the craton's margin, with the overlying Wolsey Shale and Meagher Dolomite representing deposition into moderate- and deep-water facies. The Park Shale represents the start of another cycle of transgressive sea level rise and subsequent deeper facies deposition onto the western Wyoming craton margin.

In the Blacktail Mountains, Cambrian rocks are overlain by >1.2 km of Devonian and Mississippian sedimentary rocks. Pecora (1981) focused on mapping and deciphering the Mississippian stratigraphy within the southwestern most part of the Ashbough

Canyon quadrangle, as well as portions of the adjacent Gallagher Mountain, Beech Creek, and Monument Hill quadrangles. This resulted in the definition of the Snowcrest Range Group, which consists of the Mississippian Kibbey Sandstone, Lombard Limestone, and Conover Ranch Formation (Wardlaw and Pecora, 1985). Pecora's (1987) work defined two distinct sections within the Lombard Limestone. The uppermost section is described as an olive-gray, fossiliferous limestone with interbeds of shale, and the lower member is olive-gray and pale-red purple, with fossils limited to concentrated beds.

Mesozoic and Early Cenozoic Shortening

The Blacktail Mountains are situated within the southwestern Montana overlap province, where both Sevier- and Laramide-style deformation occurred concurrently in Late Cretaceous and early Paleogene time (e.g., Kulik and Perry, 1988). The Blacktail Mountains and Tendoy Range to the southwest record evidence of impingement of the thin-skinned, Sevier-style thrust belt against the basement-involved, Laramide-style Blacktail-Snowcrest uplift, followed by contemporaneous shortening on thin- and thick-skinned structures (Kulik and Perry, 1988; Kulik and Schmidt, 1988; McDowell, 1997). In contrast to in southwestern Montana, the Sevier fold-thrust belt in southeastern Idaho has a more continuous basal décollement located within the Cambrian Gros Ventre shale (Royse et al., 1979). In the Blacktail Mountains, similar, rheologically weak Cambrian shales are present, but were not utilized as a décollement horizon. Within the Blacktail Mountains, the detachment is instead located at the base of the Mississippian Lombard Limestone (correlative to the Amsden Formation) (Ruppel and Lopez, 1984; Pecora, 1987; Tysdal, 1988a). Prior work suggests that above the décollement, which is thought

to be located at the base of the Mississippian Lombard Limestone, units shortened via a combination of formation of overturned fault-propagation folds and associated low-angle thrust faulting (Pecora, 1981; Tysdal, 1988b). Pecora (1981) also proposed that within the Ashbough Canyon quadrangle, the décollement is primarily within the lower section of the Lombard, but cuts down stratigraphic section to the northwest.

In addition to the décollement within Mississippian strata, Tysdal (1988b) also documented interaction between Sevier-style shortening and the steeply northeast-dipping, Laramide-style, basement-involved, Jake Canyon fault. The Jake Canyon fault juxtaposed Archean rocks northeast of the Blacktail Mountains atop Paleozoic rocks in the Blacktail Mountains (Achuff, 1981, Pecora, 1981). Tysdal (1988a, 1990) documented that Sevier-style folds and faults were folded by later movement on the Jake Canyon reverse fault. The Jake Canyon fault was examined during the 1980s to establish the timing of displacement on the fault, its temporal overlap and modification of Sevier-style shortening, and its mapped expression relative to basement stratigraphy (Pecora, 1981; Tysdal, 1988b, 1988a; Tysdal et al., 1990). Though apatite fission track data collected across the Jake Canyon fault do not definitively date fault-related exhumation (Tysdal, 1990), an Ar-Ar whole-rock age from an undeformed basalt that flowed across the fault indicates that the fault was inactive by ~48.1 Ma (Tysdal, 1990).

Basin and Range Extension

In southwestern Montana, two main phases of extension followed early Cenozoic shortening. The first episode persisted from the late Eocene until the early Miocene (Janecke, 2007). Following this early stage of extension, Basin and Range extension has

shaped the landscape of the western United States since ~17 Ma (Proffett, 1977). Basin and Range extension initiated in north-central Nevada and is estimated to have accommodated up to ~100% east-west extension (Proffett, 1977; Sonder and Jones, 1999). The northern Basin and Range province occurs in Idaho, Wyoming, and Montana. Basin and Range extension is attributed to both the development of the San Andreas transform margin and the migration of the Yellowstone hotspot, which initiated at ~17 Ma (Zoback and Thompson, 1978; Sonder and Jones, 1999; Pierce and Morgan, 1992). A commonly suggested hypothesis for extension in Nevada, Utah, and Arizona is that extension results from gravitational potential energy associated with high elevation mountains in the Sevier fold thrust belt that were destabilized as the Farallon convergent plate boundary was converted to the modern San Andreas transform boundary (Zoback and Thompson, 1978). Extension in the central Basin and Range has remained in a roughly east-west orientation throughout its evolution (Colgan, 2013).

Though extension is roughly east-west in southeastern Idaho, north of the Snake River Plain, the Basin and Range province has a different, northeast-southwest extension direction, which characterizes the Sawtooth, Beaverhead, Lost River, and Lemhi fault systems in east-central Idaho. In this region, prior workers have emphasized relationships between Basin and Range extension and Yellowstone hotspot magmatism (e.g., Pierce and Morgan, 1992, 2009; Rodgers et al., 2002). Because of the temporal coincidence of Basin and Range extension and the Yellowstone hotspot initiation, it has been suggested that these events are associated with each other (Pierce and Morgan, 1992). The current model explaining northern Basin and Range extension, synthesized by Pierce and Morgan (1992, 2009) is summarized here: 1) Upwelling above the Yellowstone plume head,

which heats the base of the lithosphere and causes regional uplift surrounding the plume;

2) As the North American Plate continues to move southwest relative to a fixed plume, the uplifted topography above the plume undergoes gravitational collapse. In the context of the current model, the east-west and northeast-southwest extension directions are thought to be bisected by the northeast trend of the Snake River Plain (Pierce and Morgan, 1992, 2009). However, normal faults in southwestern Montana do not consistently strike northwest-southeast, calling into question the ability of the current hotspot paradigm to explain the transition in extension direction. In southwestern Montana, several faults (Centennial fault, Ruby Mountains fault, Madison fault, etc.) strike in various directions that do not support the hypothesized northeast-southwest extension direction observed in northern Idaho (Colgan, 2013).

In support of the proposed linkage between the hotspot and northern Basin and Range extension, initial displacement on faults in the region was estimated from the depth and degree of tilting of Cenozoic basin fill within half graben adjacent to the Snake River Plain (Anders et al., 1989, 2014; Rodgers et al., 2002). Based upon the estimated timing of initial displacement on the Beaverhead fault in northeastern Idaho and the Madison fault in southern Montana, extension within the field area in southwestern Montana is thought to have initiated between 6-4 Ma (Anders et al., 2014). An additional constraint on the timing of basin formation comes from the Miocene Sixmile Creek Formation. Detrital zircons from the formation deposited near the Blacktail Mountains contain Eocene-Oligocene age-peaks, indicating the source of the sediment and mixed volcanic clasts was at least partially in east-central Idaho (Stroup et al., 2008a). U-Pb zircon geochronology within the Six Mile Creek near Lima, Montana, and northeast

Dillon, Montana suggest that there may be a southwest to northeast shift in the provenance of volcanic and recycled zircons (Stroup et al. 2008b). Stroup et al. (2008a) also observed the lack of Challis aged zircons in any Six Mile Creek Formation sample, suggesting that modern drainages are different than when the unit was deposited, and that grains were not primarily derived from central Idaho. Other work in the region suggests that the Six Mile Creek Formation contains zircons recycled from the nearby Beaverhead conglomerate, along with some more local magmatic sources (Sears et al., 2009). However, no ages younger than 4 Ma are observed within the Sixmile Creek Formation in the southeastern Blacktail Mountains. This has been argued to indicate that major offset on the Basin and Range, Blacktail fault must have initiated sometime after ~4 Ma (Sears et al., 2009).

Within the field area, the Blacktail fault is a northwest-southeast striking, Basin and Range fault displaying normal offset along the northeastern flank of the Blacktail Mountains. The fault was previously mapped with a single, distinct trace (Tysdal, 1988b). Previous work has suggested that the fault is active and may pose a seismic hazard to southwestern Montana (Stickney and Bartholomew, 1987; Stickney, 2007). Along most of the range front, the fault scarp is obscured by vegetation or Quaternary alluvial fans (Plate 1). However, in the southeastern portion of the Blacktail Mountains the fault scarp distinctly cuts the Quaternary surfaces (Stickney, 2007).

In the central portion of the current field area, the northeast-dipping Jake Canyon fault merges along-strike with the northeast-dipping Blacktail fault. Tysdal (1988b) suggested that this relationship may reflect reactivation of the Jake Canyon fault by the Blacktail fault.

Chapter III: Methods

Mapping

Fieldwork investigating the Ashbough Canyon quadrangle began during early May 2016, and lasted until mid-August 2016. Geologic mapping was conducted on quarter sections of the 1:24,000 Ashbough Canyon quadrangle topographic map. While in the field, geologic contacts, attitudes, faults, folds, and sample locations were recorded on the map. In addition, detailed field notes were taken. A Brunton compass was used to acquire all attitudes and lineations, and a handheld Garmin GPS unit was used for recording sample locations.

Following fieldwork, digitization of the map and field data began in September of 2016. Field maps were scanned as .tif image files, which were then placed into ESRI ArcMap and georeferenced. The georeferenced field map files were overlain on a U.S.G.S. topographic map provided by Dr. Jesse Mosolf of the Montana Bureau of Mines and Geology. Contacts, attitudes, and other field data were traced from the field maps using a geodatabase consisting of symbols from the NCGMP09 standard, also provided by the Montana Bureau of Mines and Geology. Satellite imagery from Google Earth was used to identify additional faults, folds, Quaternary units, and to refine contacts drawn in the field. Final drafting of the map utilized Adobe Illustrator.

Two geologic cross sections were drawn using the attitudes recorded from the field data. Both cross sections were initially hand-sketched and then digitized using Adobe Illustrator. The first cross section (A-A') crosses Mount Ashbough and the Blacktail fault and then bends in section in order to capture along-strike structures in the Ruby Range. The second cross section (B-B') was constructed perpendicular to the general strike of foliation in the Ruby Range. Folds within the Archean and

Paleoproterozoic units were drawn schematically and based on foliations and small-scale structures.

Sample Collection

Hand Samples

Rock samples were collected in the field for later hand sample and thin section analysis. Samples were collected in individual bags and the bags were labeled at the sample location with the latitude, longitude, and elevation (latitude and longitude collected in WGS 84). The sample numbers, location data, units, and local lithologies were also recorded in a field journal at the sample location. Immediately following the field season, samples were examined for mineralogy and kinematic indicators.

U-Pb Zircon Sample Processing

Two samples for U-Pb zircon analysis were collected from the field by Dr. David Pearson and entrusted to me for sample preparation at Idaho State University's (ISU) mineral separation lab. Mineral separation was completed between October and December of 2015. After intensive cleaning of the work area and lab materials, samples were individually crushed in a Braun Chipmunk to ~1-2 cm pieces. These pieces were then run in a rotating disc mill. Sample collected from the disc mill was then sieved to collect grains smaller than 425 μm . Grains larger than the 425 μm sieve were run through the disc mill until the entire sample was processed. Samples were then passed over with a hand magnet to remove iron filings introduced by the disc mill. Samples were then sorted for density using a Holman-Wilfley table, which runs water across a shaking board that

causes less dense grains to float off the table. The densest grains were collected in an aluminum foil “boat” and then run through the 425 μm sieve again to ensure that all grains were of a useable size. Grains that passed through the sieve were re-run through the Holman-Wilfley table and the dense sample was collected. The dense section was then dried in an oven at $\sim 55\text{ }^{\circ}\text{C}$ for six hours.

Dried samples were moved to a separate geochemistry laboratory and transferred from the aluminum foil into a clean plastic container. Samples were then processed with a hand magnet again in order to remove any highly magnetic grains or iron filings missed from the earlier processing. Grains not removed by the hand magnet were passed through a Frantz barrier field magnetic separator to further remove magnetic grains. Samples were passed through the Frantz at 0.3, 0.7, 1.0, and 1.8 amps with the final collected sample consisting of quartz, zircon, apatite, feldspars and other phases not affected by the magnet.

Grains were then suspended in methylene iodide (CH_2I_2) within a separatory funnel, which was used to sort samples via specific gravity. Samples were stirred and then allowed to settle for 20-30 seconds so that zircon could sink to the bottom of the separatory funnel. Grains were then collected onto filter paper. Samples were then cleaned of methylene iodide using acetone ($\text{C}_3\text{H}_6\text{O}$).

The cleaned grains were then observed under a microscope to ensure that the samples contained abundant zircon grains for either an igneous (15DP-A01; $n=40$) or sedimentary (15DP-A02; $n=100$) sample. From the igneous sample, 40 zircons were picked and embedded in an epoxy mount in ordered columns and rows. The sedimentary sample was placed in epoxy as well with >100 grains being poured randomly. Samples

were then imaged using an SEM with an attached cathodoluminescence (CL) detector. The samples did not display compositional zoning in CL images, and were therefore imaged at lower resolution using a backscattered electron detector.

Samples were processed at the University of Utah under the supervision of Dr. Mike Stearns. Standards were inserted into the sample mount using a small drill to make a hole and then inserting a smaller mount containing Plesovice and 91500 standards. Samples were then processed using a Laser-ablation inductively-coupled plasma mass spectrometer (LA-ICP-MS) with a spot size of 24 μm . Data processing was done by Mike Stearns at the University of Utah using the Iolite plugin for Igorpro (Paton et al., 2011). The data was then reduced using the Isoplot plugin for Microsoft Excel (Ludwig, 2012).

(U-Th)/He Apatite Processing

Apatite processing was accomplished in the same fashion as described in the U-Pb Zircon Sampling Processing section of this work up until the heavy liquids step. Once a sample was removed from the Frantz, it was placed into a separatory funnel and suspended in acetylene tetrabromide (TBE; $\text{C}_2\text{H}_2\text{Br}_4$). In the TBE, both apatites and zircons sank, whereas almost all other phases floated. After passing the sunken apatites and zircons from the TBE onto filter paper, the grains were cleaned with acetone. Cleaned samples were then placed into a clean separatory funnel containing Methylene Iodide. The sample was then stirred and the sunken grains, consisting primarily of zircon grains, were removed from the sample. The grains left floating in the methylene iodide after the removal of zircon were transferred to filter paper, cleaned, dried, and then stored within small vials. Vials were then transferred into a petri dish and examined under a

combination reflected light and cross polarizing microscope. Apatite grains were identified within each individual sample and the most euhedral, unbroken, and inclusion-lacking grains were selected. These ideal grains were then measured along their long and short axes, and then rotated 90°. After rotation, samples were again measured along length and width. Samples were then carefully packed into a small, cylindrical, niobium (Nb) container. Capsules were then sealed and placed into recessed cavity slides and clamped down with a binder clip. Cavity slides were then packed and sent in the care of Nathan Anderson to the LaserChron Center at the University of Arizona in Tucson, Arizona.

U-Pb Zircon Geochronology

Zircon (ZrSiO_4) U-Pb is a commonly used geochronometer due to its high closure temperature (>900°C, Cherniak and Watson, 2000). Uranium (^{238}U , ^{235}U) and thorium (^{232}Th) all decay to various isotopes of lead (^{206}Pb , ^{207}Pb , ^{208}Pb). Because the parents uranium and thorium decay to lead at a fixed rate, the ratio between the parent and daughter product within a zircon core can be used to calculate when the zircon was initially crystallized. Zircons that have experienced high-grade metamorphism may display compositional zoning that can record ages of metamorphism younger than the initial crystallization age. Two samples for U-Pb zircon analysis (15DP-A01, 15DP-A02) were collected by Dr. David Pearson during August of 2015. The samples were collected from the Cambrian Flathead Sandstone and the Quartzofeldspathic Gneiss in the Blacktail Mountains above Ashbough Canyon.

(U-Th)/He Apatite Thermochronometry

The apatite (U-Th)/He method uses the ratios of ^{235}U , ^{238}U , ^{232}Th , and ^{147}Sm to compare them to the amount of alpha particle decay (^4He) (Ehlers and Farley, 2003). As the parent products decay to the daughter product, they go through several steps involving alpha (^4He) decay. Typically, the He decay products within a grain diffuse out of the boundary of the grain and are not stored. However, when an apatite grain is cooled below the $\sim 75^\circ\text{C}$ closure temperature, it will begin to retain the emitted alpha particle (^4He) during decay (Reiners and Brandon, 2006).

Because apatites are not all the same size and have varying damage to their respective grain boundaries, not all grains have a $\sim 75^\circ\text{C}$ closure temperature. The zone in which some apatite grains fully retain He, while other grains will either partially or not at all retain the particle, is called the partial retention zone (Ehlers and Farley, 2003) (Figure 7). The partial retention zone occurs at depths that correspond to temperatures between 75°C and 45°C . Within the partial retention zone, samples that remain within these temperature ranges for long periods of time can experience partial release of ^4He , yielding inaccurate ages of when the grain was cooled below its closure temperature (Reiners and Brandon, 2006). When alpha decay occurs near the boundaries of grains, the ejected ^4He may be ejected from the crystal even when below the closure temperature (Flowers et al., 2007). Because grain size is a control on ^4He diffusion, the volume and surface area of the grain is estimated from measuring individual grains lengths and widths.

In normal faults, the footwall of the fault often experiences enhanced erosion, causing rapid exhumation (Figure 7). Using a surface temperature $\sim 10^\circ\text{C}$ and a

geothermal gradient of 20°C/km, the 75°C isotherm should be around 3-3.5 km deep. Many normal faults adjacent to ranges with ~1 km of vertical relief in the Nevada portion of the Basin and Range province have accommodated rapid exhumation of rocks in their footwalls from depths greater than 3 km (Stockli, 2005). This estimate of exhumation depth combined with the proposed near-vertical dip of the Blacktail fault (Tysdal, 1988a) and the ~1 km of relief, makes the Blacktail fault an ideal location to apply (U-Th)/He apatite thermochronology.

Samples were collected along a steep transect along the footwall of the fault within the Quartzofeldspathic Gneiss in order to obtain apatite grains that are hypothesized to have cooled below their closure temperature at different times during progressive exhumation-related cooling. Six samples were collected at ~200 meter (660 ft) vertically spaced intervals directly southeast of Riley Canyon within the Price Creek quadrangle. Samples were collected outside of the Ashbough Canyon quadrangle because south of the Ashbough Canyon quadrangle, the entire footwall is quartzofeldspathic gneiss, which is a desirable lithology from which to extract apatites.

Each sample was processed to determine when that footwall locality moved through the ~75°C isotherm. Because of the variability in grain size, and thus He diffusion rate, six grains were picked from each sample to be processed. All six samples contained six grains except for 16BC-VT3, from which only three apatite grains were found after processing. Samples were sent to the University of Arizona in Tucson, AZ for analysis in the laboratory of Dr. Peter Reiners.

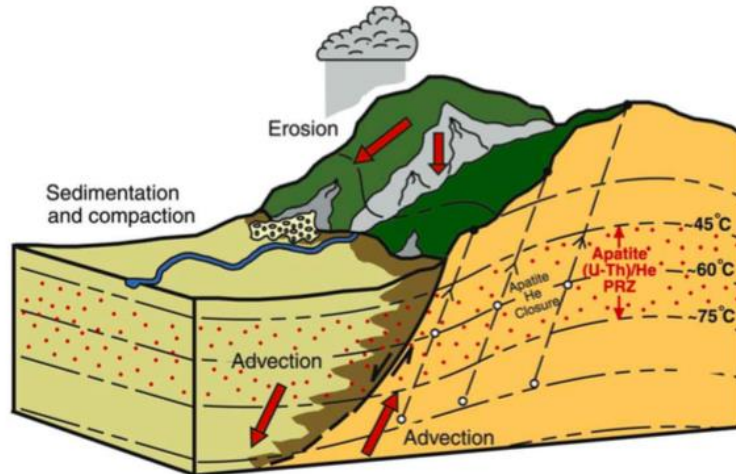


Figure 7: Schematic drawing of how apatite grains are exhumed within the footwall block of a normal fault. After the hanging wall block experiences initial displacement, the footwall block experiences enhanced erosion. This enhanced erosion causes rapid exhumation and cooling of apatite-bearing rocks. Apatites from below the partial retention zone will record fully reset ages. Apatites from either within the partial retention zone or above the zone will instead only partially reset ages and will not be indicative of the actual timing of initial displacement on the fault (from Ehlers and Farley, 2003)

Geomorphic Investigations

To place additional constraints on the slip rate of the Blacktail fault, the area was also investigated using remote sensing data. Using a combination of Worldview Imagery from ESRI and Google Earth imagery, the current work conducted a basic investigation between hill slope facets and the sizes of alluvial fans (Figure 8). Hill slope facets are the “triangular” shaped, uninterrupted slopes on the frontal portion of a range that are dissected by alluvial channels. In highly active, faulted range fronts, alluvial fans will be unable to form large surfaces and will be small relative to the sizes of hillside faces (Burbank and Anderson, 2012).

The geomorphic expression of the range-bounding fault was also evaluated using sinuosity. Sinuosity is calculated by evaluating the total length of the range front (L_r) vs the total length of the range front plus erosional embayments into the hillslope (L_{mp}).

These values are evaluated using the equation:

$$S=L_{mp}/L_r$$

Values for the lengths of the range fronts and the lengths of the range fronts and embayments were calculated from Google Earth imagery.

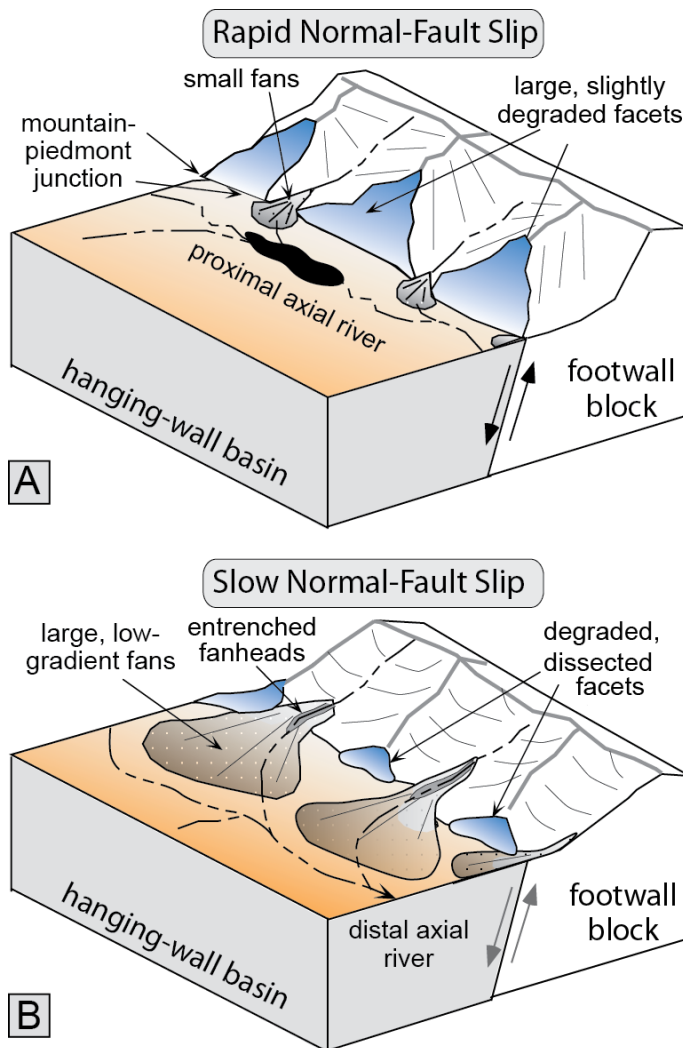


Figure 8: Schematic diagram showing the relationship among hillslope facets, alluvial fans, and the amount of displacement on range-bounding normal faults. A) Faults that experience rapid slip rates will have large hillslope facets and small, underdeveloped alluvial fans. B) Faults with slow slip rates will have small, heavily degraded hillslope facets and large, well-developed alluvial fans. (from Burbank and Anderson, 2011)

Chapter IV: Results

Field Mapping

Mapping at 1:24,000-scale resulted in a geologic map that will be submitted for publication by the Montana Bureau of Mines and Geology (Plate 1). Generally, the map area exposes moderately northwest-dipping gneisses in the southern Ruby Range and frontal Blacktail Mountains. In the Blacktail Mountains, basement rocks are overlain by gently to moderately northwest-dipping Cambrian to Mississippian sedimentary rocks. The low-elevation, central portion of the map area is primarily covered by Quaternary deposits.

Ruby Range Gneisses

Christensen Ranch Metasedimentary Suite (Acr)

Detailed field mapping within the Ruby Range identified two major northwest-dipping units: 1) the Christensen Ranch Metasedimentary Suite (Amr); and 2) the structurally lower Quartzofeldspathic Gneiss (Aqfg). The Christensen Ranch Metasedimentary Suite was observed in the northern portion of the Ruby Range and structurally overlies the Quartzofeldspathic Gneiss. The Christensen Range Metasedimentary Suite consists primarily of gray-tan to white, fine- to medium-grained, and moderately foliated quartz-plagioclase-microcline-sillimanite-biotite gneiss, with interlayered, strongly foliated, aluminous quartz-sillimanite-biotite-garnet schist (Acr), and interlayered white-gray, fine- to medium-grained dolomitic marble (Ams). All of the rocks contained within the Christensen Ranch Metasedimentary Suite (Amr) display outcrop-scale isoclinal folds (Figure 9). These rocks were cut by dikes and sills of

pegmatite, diorite, and amphibolite, which were mostly not large enough to map as distinct entities. The amphibolite and diorite sills both contain medium- to coarse-grained hornblende, with more plagioclase feldspar observed in the diorite. Pegmatite sills and dikes, consisting primarily of quartz and feldspar, were also observed to cut all units.



Figure 9: Photograph of interlayered schists and gneisses within the Christensen Ranch Metasedimentary Suite. Layers are intensely folded.

Quartzofeldspathic Gneiss (Aqfg)

The Quartzofeldspathic Gneiss (Aqfg; Plate 1) is predominantly a hornblende-garnet-biotite-plagioclase-quartz-microcline gneiss. Additional lithologies within this map unit include garnet-biotite-quartz-microcline gneiss, biotite-quartz-plagioclase-microcline gneiss, quartz-microcline-garnet-biotite gneiss, and sillimanite-quartz-plagioclase-biotite-microcline gneiss. Commonly, the gneiss is white-gray to red-pink, medium-grained, and moderately foliated. Also contained within this map unit are amphibolite, diorite, and pegmatite sills and dikes that are not large enough to map as separate units (Figure 10).

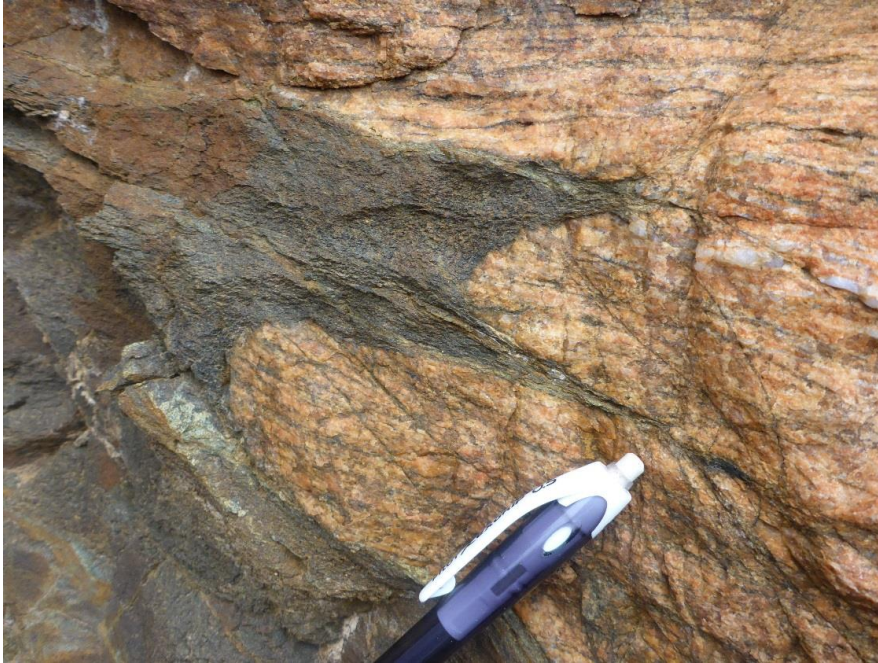


Figure 10: Diabase intrusion into Quartzofeldspathic Gneiss. This photo was taken in Ashbough Canyon, although similar intrusions were observed in the Ruby Range. (Photo by D. Pearson).

Dolomitic marbles found within the Quartzofeldspathic Gneiss were fully surrounded by the Quartzofeldspathic Gneiss within the study area but were large enough to map separately (Am). The marbles were primarily fine- to medium-grained and dolomitic, with lesser garnet-sillimanite-biotite schist directly adjacent to the contacts with the Quartzofeldspathic Gneiss. The contact between the marble and the Quartzofeldspathic Gneiss was sharp, with no contact metamorphism and no apparent shear zones. The contact between Quartzofeldspathic Gneiss (Aqfg) and the Christensen Ranch Metasedimentary Suite (Acr) is obscured by pegmatite and amphibolite intrusions (Figure 11).



Figure 11: Example of a pegmatite dike intruding the contact between the Quartzofeldspathic Gneiss (Aqfg) and the Christensen Ranch Metasedimentary Suite (Acr).

Blacktail Mountains

Paleozoic Strata

In the Blacktail Mountains, the Quartzofeldspathic Gneiss is overlain nonconformably by middle Cambrian through Mississippian sedimentary rocks that dip gently northwestward. Paleozoic rocks generally strike north-south and dip gently to the west, with the exception of the highly folded Mississippian Lombard Limestone. Presented here is a stratigraphic correlation of mapped units created from field observations during this study and previous work (Pecora, 1981, 1987; Tysdal, 1988b), and descriptions of each unit formed from field work and hand sample analysis (Figure 12). The thicknesses of these various units were taken from Tysdal (1988b).

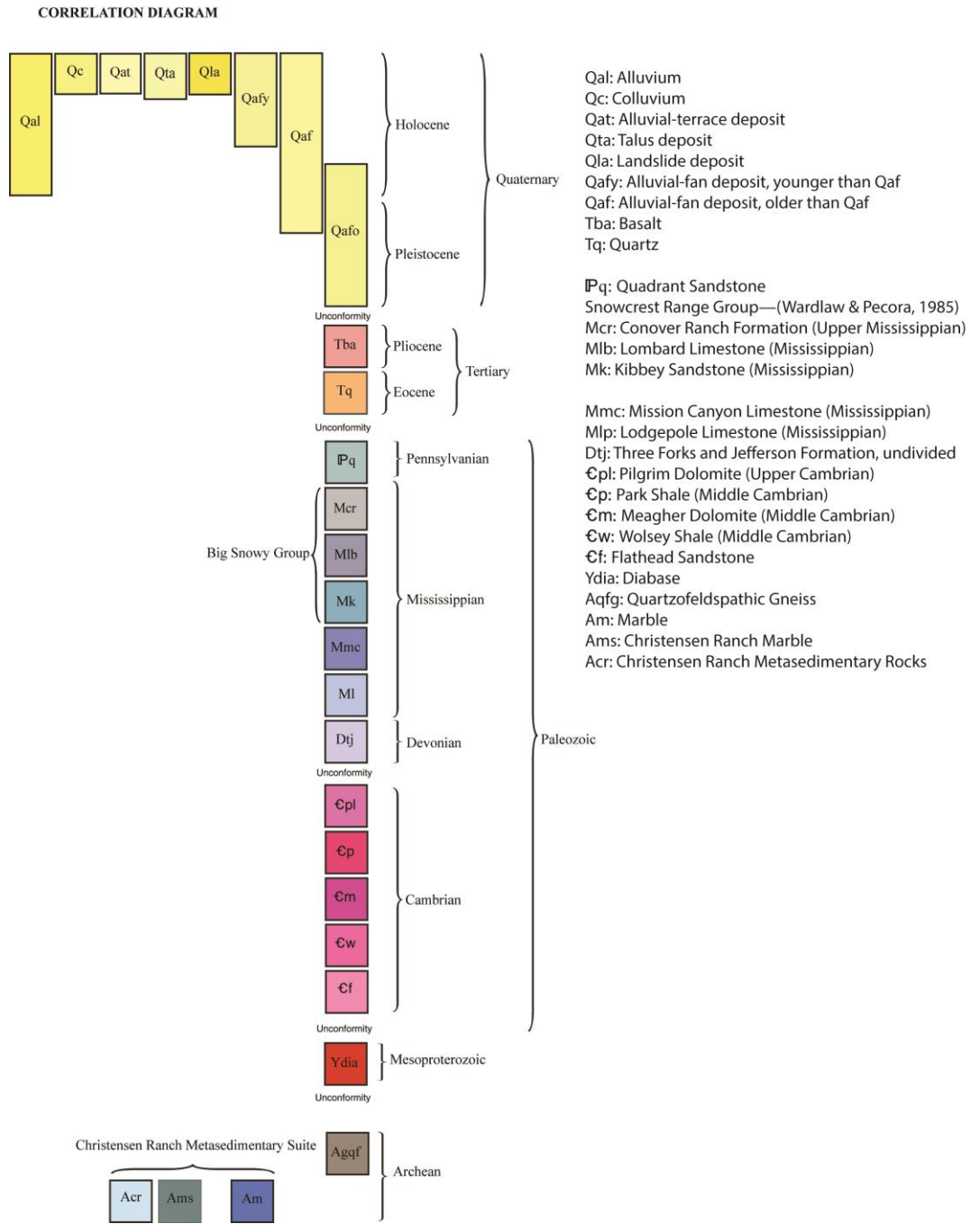


Figure 12: Correlation of mapping units for the Ashbough Canyon quadrangle.

Cf - Flathead Sandstone (Middle Cambrian)—

Upper light-yellow to tan-gray, fine- to medium-grained, moderately to poorly sorted subarkose, arkose, and quartz arenite and quartzite about 9 m (30 ft) thick,

and lower maroon to pink, fine- to coarse-grained arkosic sandstone and pebble conglomerate, with 1-5 mm sub-angular to angular quartz and feldspar clasts, about 0.6 m thick (2 ft), medium-bedded. Trough cross-bedding is present in the upper sections. Contact with underlying Quartzofeldspathic Gneiss is sharp and nonconformable, with underlying gneisses dipping 35-40° to the northwest beneath the contact. Thickness ranges from 6 m (20 ft) to 25 m (82 ft) (Tysdal, 1988b).

The lower Flathead Sandstone (€f) exposed directly above the contact with Archean gneiss is a breccia with angular to sub-angular quartz and feldspar clasts (Figure 13). A sample of these clasts was collected and examined under a reflected light microscope at Idaho State University (16BC-03; appendix A). Further examination confirmed that the clasts were primarily quartz and potassium feldspar. Above the breccia, the Flathead Sandstone grades upward to a fine- to medium-grained quartz sandstone with interbeds of arkosic sandstone.

€w - Wolsey Shale (Middle Cambrian)—

Black, gray, and olive-green argillite and micaceous shale, with minor gray slate. Poorly exposed in the mapping area; observed as float between the Flathead Sandstone and the base of cliffs of Meagher Dolomite. Conformable contact with the underlying Flathead Sandstone. Thickness is 24 m (80 ft).

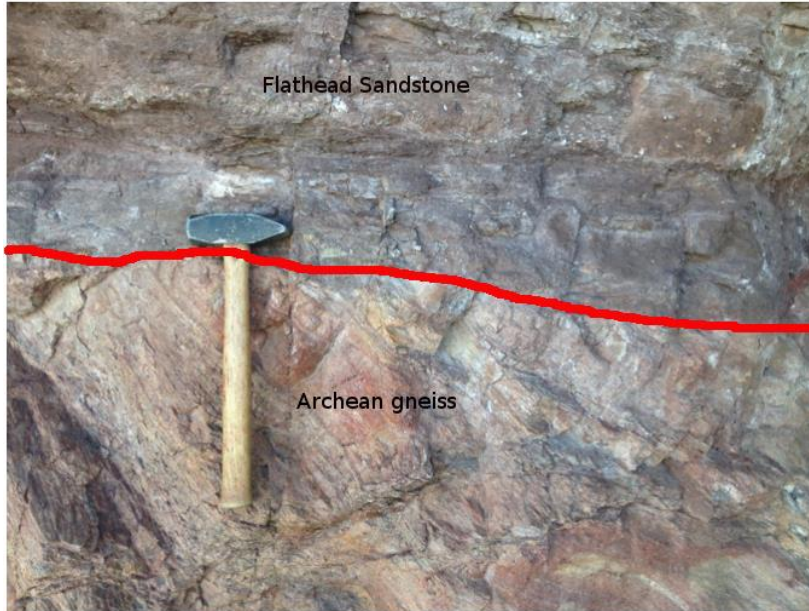


Figure 13: The contact between the Archean Quartzofeldspathic Gneiss (Aqfg) and the Cambrian Flathead Sandstone (€f), as observed in Ashbough Canyon. Photo by D. Pearson.

€m- Meagher Dolomite (Middle Cambrian)—

Orange to light-pink dolomite that is fine to medium crystalline, medium- to thick-bedded. Exhibits tan to red mottled texture oriented roughly perpendicular to bedding that may reflect bioturbation (Thomas and Roberts, 2007). Forms prominent cliffs near Ashbough Canyon. The upper 17 m is orange to gray, and contains minor, gray to green, shale interbeds. Upper layers also display trough cross-beds. The underlying contact with the Wolsey Shale is not exposed but is presumed to be conformable and gradational (Pecora, 1981). Thickness is 175 m (575 ft).

The Meagher Dolomite was a prominent cliff-forming unit near Ashbough Canyon (Figure 14). Bedding was well exposed in the unit and generally has a northeast-southwest strike and a gentle northwest dip.



Figure 14: Example of the cliffy exposures of the Meagher Dolomite (ϵm) found within Ashbough Canyon.

ϵp - Park Shale (Middle Cambrian)—

Green-gray to gray-tan, argillaceous and micaceous shale, thin- to medium-bedded. Poorly exposed slope-former; observed as float between cliffs of the Meagher and Pilgrim dolomites. Contact with the lower Meagher Dolomite is presumed to be conformable. Thickness is 30 m (100 ft).

ϵpl - Pilgrim Dolomite (Upper Cambrian)—

Gray to pink, fine- to medium-grained, sugary dolomite, medium- to thick-bedded. Forms large cliffs. Lower contact is concealed but is presumed to be conformable with the underlying Park Shale. Thickness is 60 m (200 ft).

The Park Shale (ϵp) and the Pilgrim Dolomite (ϵpl) represent two half-cycles of transgressive Sauk shoreline-related deposition (Thomas, 2007). The Park Shale has a limited exposure whereas the Pilgrim Dolomite forms prominent, west-dipping cliffs (Figure 15).



Figure 15: Example of a typical Pilgrim Dolomite (€pl) cliff exposure.

Devonian

Dtj- Three Forks Formation and Jefferson Formation undivided—

Three Forks Formation (Lower Mississippian and Upper Devonian)—Gray-blue

calcareous shale. Limited exposure in the field area; observed as float above cliffs of the Pilgrim Dolomite. Contact with underlying Pilgrim Dolomite is thought to be unconformable (Pecora, 1981).

Jefferson Formation (Upper Devonian)—Yellow-beige-red to gray-tan when weathered,

sugary dolomite with interbeds of fine calcareous shale, thin- to medium-bedded.

Forms small outcrops. Limited exposure near the mouth of Weston Canyon and on the southern boundary of Ashbough Canyon. Lower contact is not exposed but

is presumed to be unconformable with the underlying Three Forks Formation (Pecora, 1981). Poorly exposed in the map area.

The Upper Devonian Jefferson Formation was only observed in two places: a hillside on the southeastern corner of the map and near the mouth of Weston Canyon. The Three Forks Shale had even less exposure and was only observed as gray-blue calcareous shale float. The lower contact with the Pilgrim Dolomite is buried, but is thought to be unconformable, based upon early work in the region documenting major Devonian erosion of Ordovician and Silurian rocks (Sloss, 1950). The total thickness for both formations is 54 m (180 ft).

Mississippian Strata

Mlb- Lodgepole Limestone (Mississippian)—

Gray-tan, fossiliferous limestone, thin- to medium-bedded, with interbedded gray, micritic to crystalline limestone, and tan-beige calcareous siltstone, thin-bedded. Commonly slope-forming and weathers to orange, black, and purple. Upper 35 m of unit has 1-5 mm thick lenses of brown to gray calcareous shale. Unit emits a fetid smell when broken. Fossils found throughout the unit are commonly in discrete layers (1-4 cm thick) and include crinoids (>1 mm), minor fusulinids, brachiopods (>2 mm), and rugosan corals. Contact with underlying Jefferson is not observed but is presumably conformable. Thickness 220 m (720 ft).

Mmc- Mission Canyon Limestone (Mississippian)—

Gray, micritic, fossiliferous limestone, with common red-beige chert nodules and ribbons, massive-bedded. Forms prominent cliffs throughout the field area. Contains prominent fossil layers (2-8 cm thick) composed of rugosans and

brachiopods. Localized calcite veins up to 50 cm wide can be found in the upper portion of the unit. Upper section also contains a brecciated layer composed primarily of crystalline limestone fragments with some minor quartz, supported by a tan/red clay rich calcitic matrix. The contact with the underlying Lodgepole Limestone is conformable and gradational. Mapped at the first layers lacking brown to gray shale. Thickness ranges from 270 m (885 ft) to 340 m (1115 ft).

Mk- Kibbey Sandstone (Mississippian)—

Tan to yellow, very fine- to fine-grained, well-sorted quartz sandstone, thin-bedded. Lower sandstone contains black chert grains. Exposure of unit is very limited in the field area. Contact is sharp and conformable with the underlying Mission Canyon Limestone. Thickness is ~30 m (100 ft).

The Kibbey Sandstone was commonly observed as a red-brown to tan-brown soil with some sandstone fragments between the lower Mission Canyon Limestone, and the higher Lombard Limestone. The only observed outcrop of Kibbey Sandstone was found in Weston Canyon and exhibits a gentle dip to the west.

Mlb- Lombard Limestone (Mississippian)—

Upper yellow-tan to beige, fossiliferous, micritic limestone, and tan-beige, micritic limestone, with calcareous shale interbeds, thin- to thick-bedded, thickness 210 m (690 ft); and lower gray to tan-gray micritic limestone, medium-bedded to massive, thickness 140 m (500 ft). Upper part forms the cliffs and talus slopes adjacent to Mount Ashbough and contains flat, hardened, micritic layers, some up to 50 cm thick, with brachiopods and crinoids. Lower part locally forms cliffs with occasional fine to medium sand-sized fossil layers ranging from 1-4 cm

thick, but in the southeastern portion of the map, the unit becomes very subdued and is exposed in limited locations within low grassy topography. Total thickness is at least 350 m (1025 ft).

Mcr- Conover Ranch Formation (Upper Mississippian)—

Red to beige, very fine- to fine-grained, well to moderately sorted quartz sandstone. Lower exposure of this unit is a matrix-supported conglomerate containing small pebbles of chert, limestone, and lithic fragments ranging from 0.3-4 cm. Unit forms poorly exposed outcrops on low gradient slopes. Lower contact is sharp and unconformable with the underlying Lombard Limestone. Thickness ranges from 6-9 m (20-30 ft).

IPq- Quadrant Sandstone (Pennsylvanian and Upper Mississippian)—

Tan to pale-yellow, fine-grained quartz sandstone. Some weathered surfaces have a red to light pink tint. Limited exposure on the southeastern edge of the map. The contact between the Quadrant Sandstone and underlying Conover Ranch Formation is sharp and conformable. Thickness is 210 m (690 ft).

The only Pennsylvanian-aged unit in the study area is the Quadrant Sandstone (IPq). This unit had limited exposure and was observed in small outcrops and tan sandstone float on the top of hillsides in the southwestern mapping area.

Quaternary Sediments

Quaternary units were mapped using a combination of field observations and satellite imagery. Quaternary surficial deposits constitute the central portion of the mapping area. Three episodes of alluvial fan formation have been identified based on their stratigraphic relationships to other Quaternary units. The oldest alluvial fan (Qafo)

was deposited in the northwestern corner of the map and is heavily obscured, buried, and incised by all other Quaternary units. The two younger fan surfaces (Qaf and Qafy) were identified based on the gradients of their surfaces, the amount of incision by creeks (Qat), and the relationship with Blacktail Deer Creek. The oldest alluvial fan surface is incised by the active Blacktail Deer Creek, which is the site of active deposition of alluvium (Qal). Quaternary fans (Qaf) contain material shed off the northeastern flank of the Blacktail Mountains. Active Quaternary terrace (Qat) deposits are deposited along the banks of small drainages that incise through these fans and carry material to the Blacktail Deer Creek.

Structural Geology

Basement Rocks

The Quartzofeldspathic Gneiss (Aqfg) was very well exposed in the Ruby Range, allowing for many foliations (n=402) to be collected during mapping. These foliations show a remarkably similar regional strike and dip, with an average strike of 226° and a dip of 48° northwest (Figure 16). Along with foliation data, many of these outcrops provide insight into the folding and style of deformation in the Ruby Range. Outcrop-scale isoclinal folds were observed in several locations, which may be concordant with the regional-scale folding that affected basement in the Ruby Range (Figure 17). These smaller scale isoclinal folds were also observed in some of the pegmatite dikes intruded into the Quartzofeldspathic Gneiss (Figure 18). Outcrop-scale observations of the pegmatite dikes and sills indicate that many display foliations in the same orientation as the regional foliation in the Ruby Range.

Foliations recorded from the gneisses and schists within the Christensen Ranch Metasedimentary Suite (n=170) center around an average strike of 230° and a dip of 46° to the northwest (Figure 19).

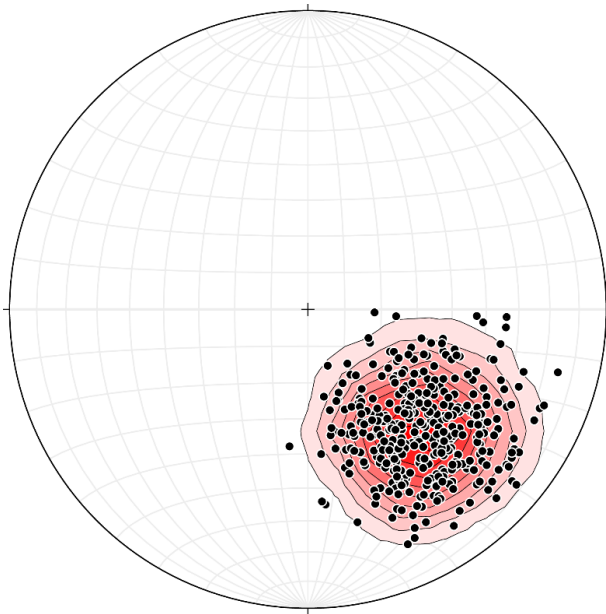


Figure 16: Stereogram showing poles to foliation for the Quartzofeldspathic Gneiss (n=405). Kamb contours for this plot have an interval of 5 with darker colors indicating higher contours. From these foliations, an average pole to foliation with a trend of 137° , and a plunge of 41° is defined.

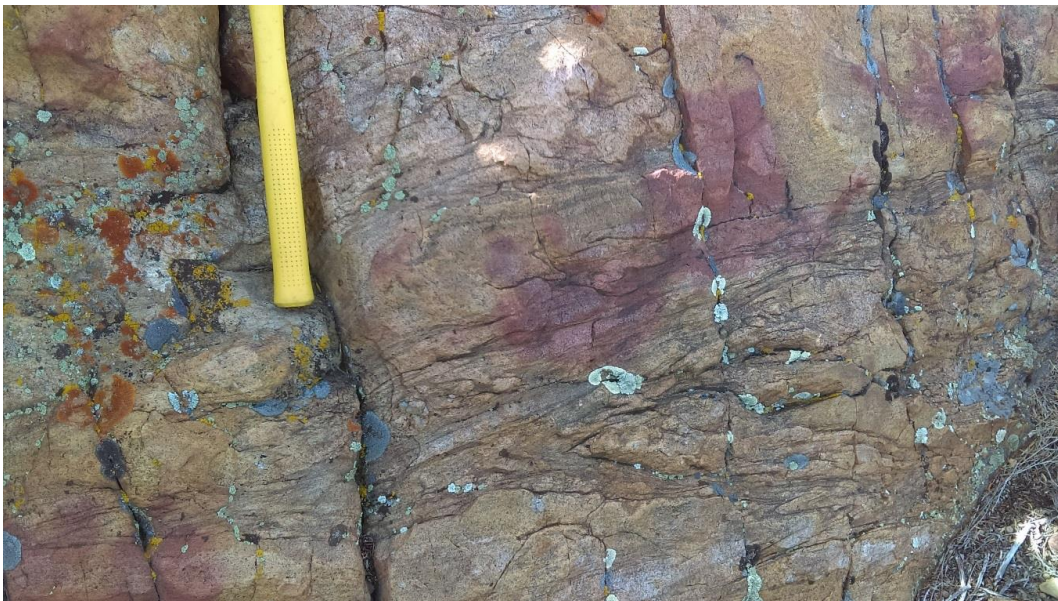


Figure 17: Isoclinal fold exposed within an outcrop of Quartzofeldspathic Gneiss (Aqfg).



Figure 18: Examples of isoclinally folded pegmatite intruding the Quartzofeldspathic Gneiss (Aqfg).

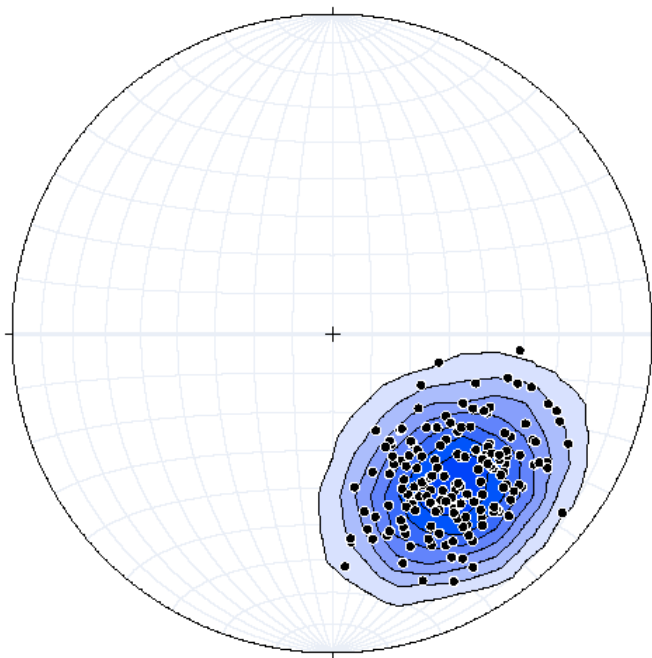


Figure 19: Stereogram showing the poles to foliation of gneisses and schists within the Christensen Ranch Metasedimentary Suite (n=170). Kamb contours use a contour interval of 5 with darker colors indicating higher contours. The average trend is 140° , and average plunge is 37° .

Lombard Limestone Deformation

The Paleozoic section exposed below the Lombard Limestone (Єf to Mk; Plate 1) strikes roughly northeast-southwest and in general dips gently to the northwest-west. In contrast, bedding within the Lombard Limestone is highly variable, and the unit displays significant folding and minor faulting (Figure 20; Figure 21).

Folds within the Lombard Limestone occur as both outcrop- and map-scale structures (Figure 20). Folds commonly occur as broad anticlines, with tight, V-shaped synclines, which verge to the east-northeast, have fold axes that trend north-northeast, and have west-dipping axial surfaces (representative value: $186^{\circ}, 17^{\circ} \text{ W}$) (Figure 22). Within the larger folds, parasitic anticlines and synclines have the same fold vergence and axial plane orientations. Additionally, these smaller scale folds display disharmonic folding.

Deformation within the Lombard Limestone (Mlb) was also accommodated locally via thrust faulting (Figure 21). Thrusting was identified at two locations during mapping (Plate 1). Examination of the bedding at one of these locations suggested that a hanging wall ramp overlies a footwall flat.



Figure 20: Example of a fold in the Lombard Limestone (Mlb) observed southwest of Mount Ashbough. Pictured is the left limb of a broad anticline. The folds pictured here are parasitic folds within that larger anticline, with smaller scale anticlines having broad hinges while synclines are tight and V-shaped.



Figure 21: Fault observed in the Lombard Limestone displaying a thrust sense of displacement. Bedding in the hanging wall is oriented roughly with the ridgeline. Bedding in the footwall is roughly parallel to the plane of the fault. Because of these cutoff relationships, this location is interpreted as a hanging wall ramp on a footwall flat.

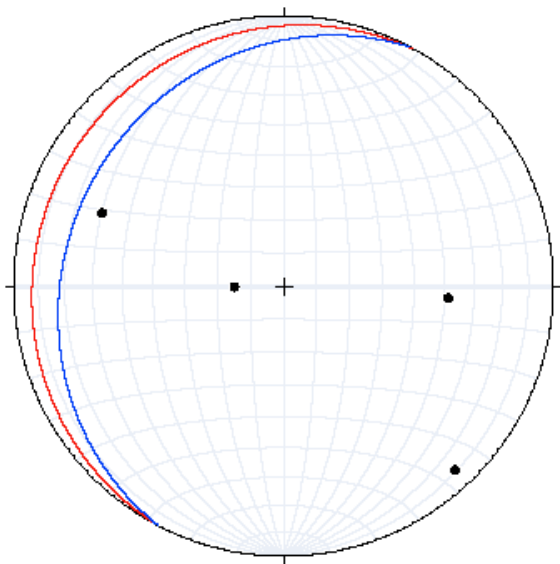


Figure 22: Poles to bedding (black dots), and associated axial planes (red and blue great circles) of two well-defined, representative, folds within the Lombard Limestone (Mlb). The red line shows a plane that strikes 209° and dips 8° W. The blue line shows a plane that strikes 208° and dips 20° W. These planes are similar to the broader-scale folds observed in the field (see Figure 25).

Jake Canyon Fault Observations

The Jake Canyon fault is poorly exposed in the Ashbough Canyon quadrangle. It was identified at the mouth of Ashbough Canyon (Tq) on the basis of silicification that was previously shown by Tysdal (1988b) to be associated with the fault (Tysdal, 1990). The silicified outcrop consisted of large red to white quartz clasts supported by a siliceous matrix. Previous work suggested that this quartz replaced Archean Quartzofeldspathic Gneiss (Aqfg) via hydrothermal fluids related to activity on the Jake Canyon fault (Tysdal, 1988b; Tysdal et al., 1990). In addition, exposures of Quartzofeldspathic Gneiss structurally overlying Mississippian rocks have been described in the northwestern Blacktail Mountains and in Sheep Creek (Achuff, 1981; Tysdal, 1988b). On the range front in the northwestern Blacktail Mountains within the Ashbough Canyon quadrangle, prior mapping documented Quartzofeldspathic Gneiss (Aqfg) thrust over Mississippian strata (Tysdal, 1988b). This work confirmed the prior Archean-over-Mississippian field relationship. The Jake Canyon fault generally strikes northwest-southeast and dips steeply to the northeast (Tysdal, 1988a). Near Ashbough Canyon the fault appears to merge along strike with the Basin and Range Blacktail fault.

Blacktail Fault

The range-bounding, Basin and Range, Blacktail fault strikes northwest-southeast and dips at a high angle to the northeast. While usually buried by Quaternary alluvial fans, terraces, and landslides, there was one location 0.4 km southeast of Ashbough Canyon where the fault scarp cuts an actively forming alluvial fan (Qaf; Plate 1).

Satellite imagery shows a different surface expression of the Blacktail fault north and south of Ashbough Canyon. North of Ashbough Canyon, the fault is adjacent to the range front and is contained along a single range-bounding fault. South of Ashbough Canyon, the Blacktail fault appears to splay into several northwest-southeast striking normal faults.

Isotopic data

U-Pb Zircon

15DP-A01

Sample 15DP-A01 was collected from the Quartzofeldspathic Gneiss unit (Aqfg) to evaluate its age and to investigate it as a potential provenance source for the overlying Cambrian Flathead Sandstone (€f). Following mineral separations at Idaho State University, the sample was analyzed at University of Utah with an intended 40 igneous zircon cores and rims on large enough grains to be analyzed. Three grains provided concordant ages (with discordance less than 15%) at 2576 ± 17 Ma, 2501 ± 17 Ma, and 2769 ± 24 Ma. Plotting all of the data together suggests a crystallization age older than ~2600 Ma (Figure 23).

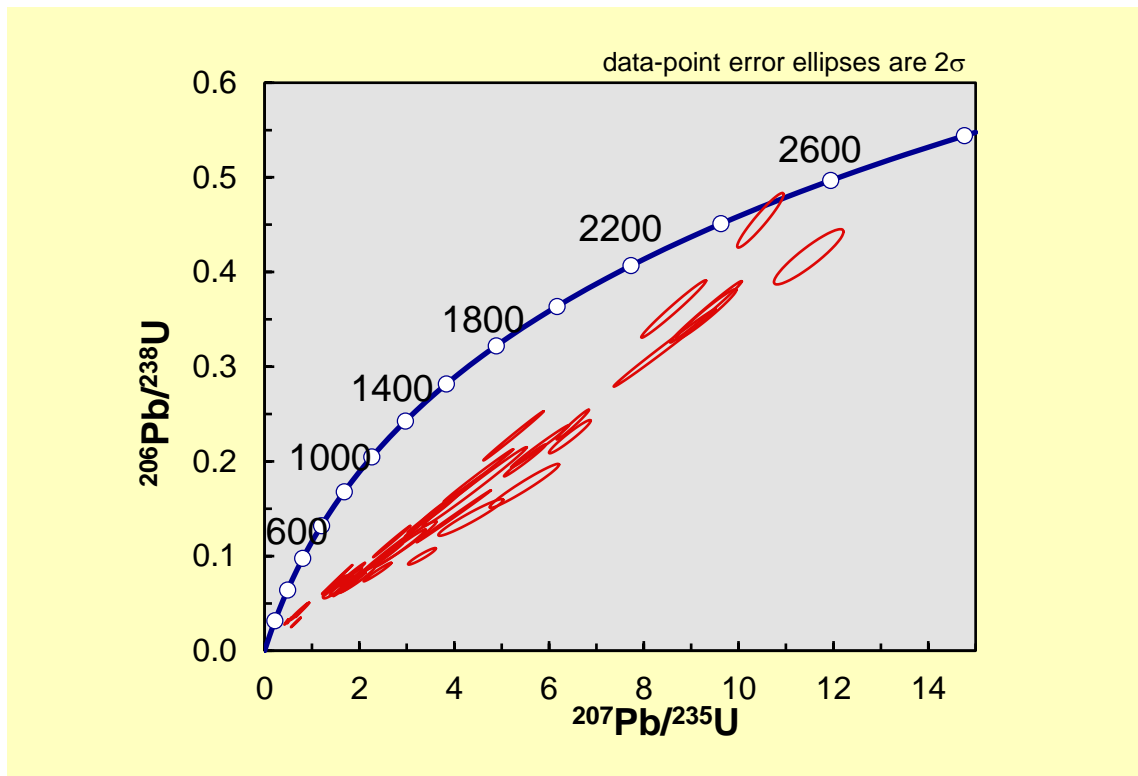


Figure 23: Wetherill concordia plot showing the data from sample 15DP-A01. U-Pb zircon analysis shows a concordant age at $2496 \text{ Ma} \pm 42 \text{ Ma}$. Red ellipses represent the 2σ error associated with each analysis. Discordant grains that plot directly below and to the right of the upper intercept age show that there must be an older crystallization age for the gneiss than $\sim 2600 \text{ Ma}$.

15DP-A02

Sample 15DP-A02 was collected from the Cambrian Flathead Sandstone in Ashbough Canyon directly above the contact with the Quartzofeldspathic Gneiss (Aqfg). This sample included the dating of 124 zircon grains, with 40 grains displaying concordant ages (discordances $<10\%$). Concordant grains yielded two main age-peaks at $2501 \pm 49 \text{ Ma}$, and $2798 \pm 58 \text{ Ma}$, with lesser older Archean ages (Figure 24). A concordia diagram of all data suggest a potential older ($\sim 3800 \text{ Ma}$) provenance not strongly represented by the concordant data (Figure 25).

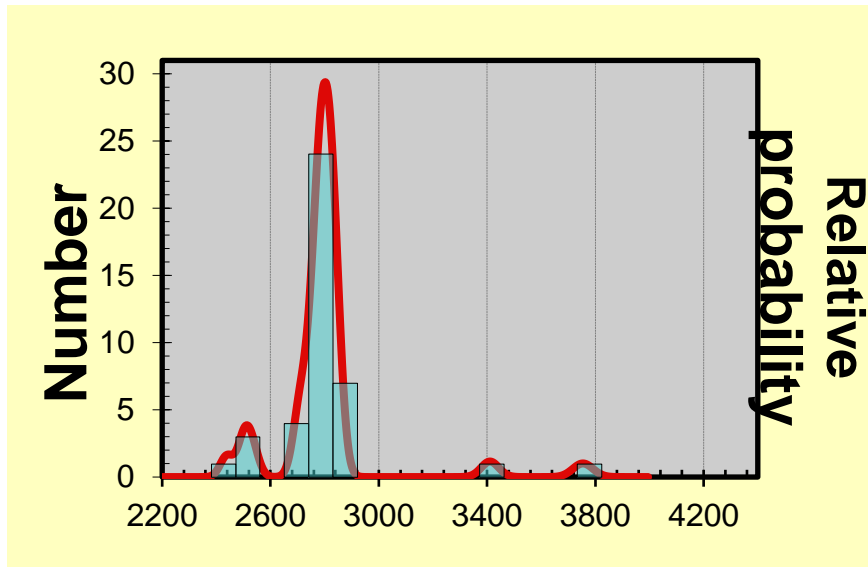


Figure 24: Relative probability plot of zircon ages from sample 15DP-A02. Sample was collected from the Flathead Sandstone directly above Archean gneiss. The two primary U-Pb age peaks occur at ca. 2501 ± 49 Ma and 2798 ± 58 Ma. The x-axis represents age (Ma) and the y-axis represents the number of grains. The heights of the blue boxes represent the total number of zircons that fall within the age range represented by the box.

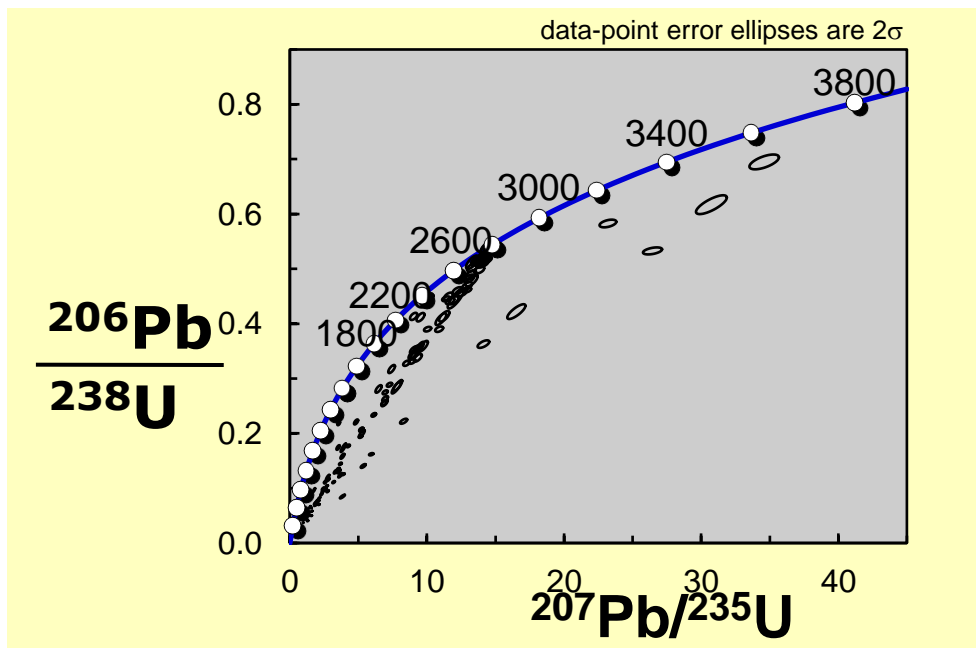


Figure 25: Concordia plot for sample 15DP-A02 from the Quartzofeldspathic Gneiss (Aqfg). Ellipses represent 2σ errors. Locations where ellipses cross the dark blue line indicate that grains have concordant ages. The U-Pb zircon peaks observed in the relative probability plot (Figure 29) are represented by locations with abundant concordant grains. Some discordant grains plot along a different upper intercept path than the oldest observed major peak (2798 ± 58 Ma).

(U-Th)/He Apatite

(U-Th)/He apatite data were acquired from five samples collected directly south of the Ashbough Canyon quadrangle (Figure 26) (Appendix C). Six samples were collected but sample 16BC-VT6 had no apatite grains available for analysis. 16BC-VT1 was collected from the top of the vertical transect (elevation = 9241 ft). Six apatite grains were analyzed and recorded dates ranging from 25.32 ± 0.51 Ma to 152.97 ± 2.88 Ma (Figure 27). 16BC-VT2 was collected from an elevation of 8660 ft, and had five apatite grains for analysis (Figure 27). Dates from this sample ranged from 30.14 ± 1.08 Ma to 54.50 ± 1.16 Ma. 16BC-VT3 had six grains and was collected from an elevation of 7994 ft (Figure 27). Grains record dates ranging from 14.77 ± 0.34 Ma to 46.35 ± 0.77 Ma. 16BC-VT4 had five grains analyzed and was collected from an elevation of 7477 ft (Figure 27). Grains record dates ranging from 44.53 ± 0.62 Ma to 109.54 ± 1.58 Ma. 16BC-VT5 had four grains and was collected from the lowest elevation in the transect (6960 ft) (Figure 27). Grains had dates ranging from 42.51 ± 0.73 Ma to 69.49 ± 1.05 Ma. Because of the scatter in dates, it is difficult to apply estimated exhumation ages to these samples. During collection of samples along the vertical transect, a previously unmapped, northeast-dipping normal fault was identified between 16BC-VT4 and 16BC-VT3 (Figure 26).



Figure 26: Location of samples collected in the vertical transect south of the Ashbough Canyon quadrangle. Dots show locations where samples were collected. A previously unmapped fault between sample 16BC-VT3 and 16BC-VT4 was observed (shown in black). Sample 16BC-VT6 did not have any apatite grains and was not analyzed.

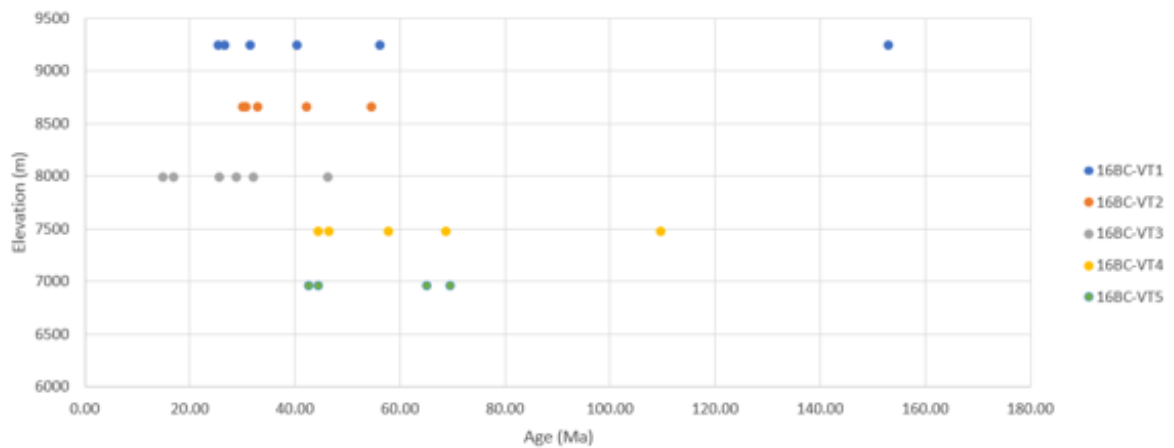


Figure 27: Chart showing the ages of individual grains within each sample compared to the elevation at which the samples were collected.

Because the ages recorded at each sample elevation were so variable, the potential for radiation damage in the grains was investigated. Laboratory work suggests that He retentivity in apatite can be affected by radiation damage in a grain (Flowers et al., 2007). This laboratory work also suggests that this relationship is best observed as a correlation between the effective uranium ($eU = U + (0.235 * Th)$) and the recorded apatite age. Plots investigating this relationship for each sample were produced, although none show strong positive or negative correlation between eU and age (Figure 28). This indicates that it would be difficult to extract further information on the thermal histories of each sample.

Geomorphology

Range front geomorphology of the Blacktail Mountains within the Ashbough Canyon quadrangle showed a distinct change between the northwestern and southeastern sections. Within the northwestern section, only small active fans are present, with large, unimpeded hillslope facets; in contrast, the southeastern range front has a much lower gradient, and more varied topography (Figure 29). In addition, the trace of the Blacktail fault appears to occur at the slope break at the front of the range. The southeastern portion has much more eroded hillslopes with large, actively-forming alluvial fan surfaces. Sinuosity calculations for the northwestern and southeastern range fronts display a relationship consistent with the geomorphic observations (Figure 29). Sinuosity calculations provide a value which allows for estimates of the slip rate on range bounding faults (see Methods). Sinuosity values closer to 1 commonly indicate a rapid slip on the range-bounding fault, whereas values of 2 or higher indicate a slow fault slip rate (Burbank and Anderson, 2012). The northwestern section has a sinuosity value of 1.11, while the southeastern has a value of 1.94.

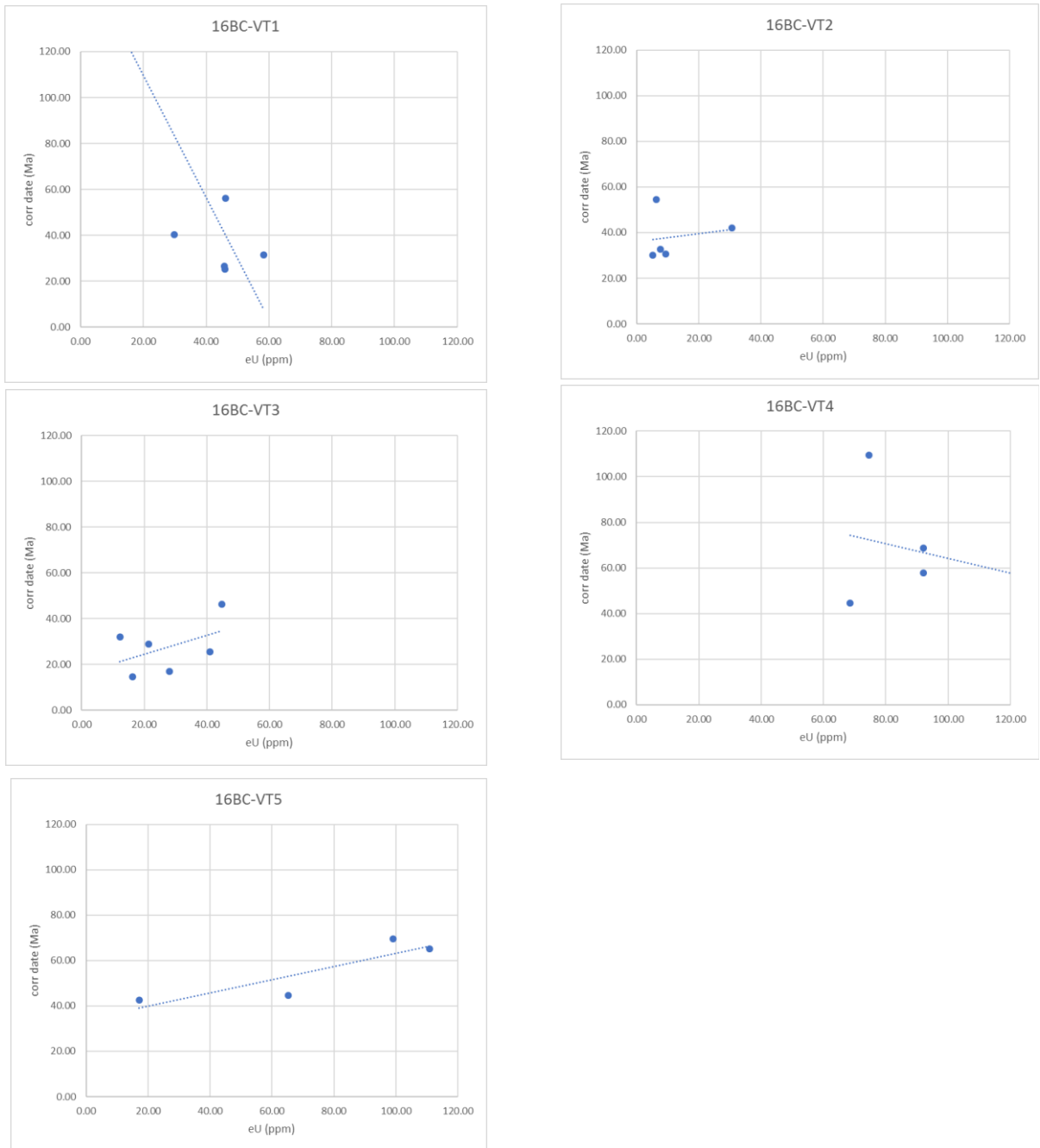


Figure 28: Effective uranium ($eU = U + (0.235 \cdot Th)$) vs. age plots for each (U-Th)/He apatite sample. No samples show a strong visual correlation between eU and age.



Figure 29: Google Earth images of the northern and southern portions of the Blacktail Mountains range front contained within the Ashbough Canyon quadrangle. The northern portion of the range front has a calculated sinuosity value of 1.11. The southern portion of the range front has a sinuosity value of 1.94.

Chapter V: Discussion

Basement Geochronology

The protolith of the Quartzofeldspathic Gneiss exposed in the Ruby Range and Blacktail Mountains and its relationship to the structurally higher Christensen Ranch Metasedimentary Suite have been long-standing research questions in southwestern Montana. Field observations of the compositionally and texturally similar marbles and surrounding metasedimentary rocks in both basement units, one U-Pb zircon sample from this study, and previous zircon and monazite geochronology suggests that the contact is intrusive, and the protolith of the Quartzofeldspathic Gneiss is a granite.

Marble layers and adjacent aluminous gneisses within the Quartzofeldspathic Gneiss unit are interpreted here to be preserved as intensely folded screens. The marbles are exposed as elongated northeast-southwest trending bodies within the Quartzofeldspathic Gneiss; foliations within these rocks strike parallel to the regional foliation. The marble layers contained in the Christensen Ranch Metasedimentary Suite (Ams) and the marble (Am) surrounded by the Quartzofeldspathic Gneiss are virtually identical in hand sample. Both samples contain abundant dolomite that ranges in size from fine- to medium-grained. The marble within the Quartzofeldspathic Gneiss is surrounded by aluminous garnet-biotite-schist in some locations that has a sharp contact with adjacent Quartzofeldspathic Gneiss. Similar aluminous schists are preserved adjacent to the dolomitic marble layers of the Christensen Ranch Metasedimentary Suite.

Within the Ruby Range previous workers identified two metasedimentary units, the Older Gneiss and Schist (previously the Pre-Cherry Creek), and the Christensen Ranch Metasedimentary Suite (Amr) (Garihan, 1979; Karasevich et al., 1981; James,

1990). In contrast to the Christensen Ranch Metasedimentary Suite, the Older Gneiss and Schist unit does not contain any marble. This suggests that the dolomitic marble preserved as screens in the Quartzofeldspathic Gneiss is best correlated with the Christensen Ranch Metasedimentary Suite. The presence of these marbles in the Quartzofeldspathic Gneiss, combined with the sharp contacts, and oblong-shaped map expression, suggest that the marbles with the Quartzofeldspathic Gneiss (Am) are preserved, folded, screens of Christensen Ranch Metasedimentary Suite marble (Ams).

Previous work analyzing U-Pb zircon and monazite ages from the Quartzofeldspathic Gneiss in the Ruby Range suggests an intrusive age of 2775 ± 11 Ma related to the Beartooth orogeny, and a subsequent metamorphic event at ~ 2440 - 2470 Ma (Jones, 2008). New U-Pb zircon results from one sample of the Quartzofeldspathic Gneiss exposed in the Blacktail Mountains (sample 15DP-A01) yielded three concordant analyses, which record ages between ~ 2500 - 2770 Ma. The most concordant analysis has an age of ~ 2500 Ma, with older discordant analyses suggesting an older crystallization age. The discordant data display several groupings of grains, which are interpreted to reflect multiple lead loss events that affected the Quartzofeldspathic Gneiss. Some groups of discordant grains have ages that plot adjacent to or below ~ 2600 Ma on the Concordia diagram, suggesting that there is an older crystallization age of the rock. Although interpretations from discordant data are not ideal, the data appear to align along a path suggesting an upper intercept between ~ 2700 - 2800 Ma. These data, coupled with field observations, are consistent with the hypothesis that the Quartzofeldspathic Gneiss was initially a ~ 2775 Ma granitic intrusion during the Beartooth orogeny; a concordant date at ~ 2500 Ma may indicate subsequent metamorphic zircon growth during the

Beaverhead/Tendoy orogeny (Jones, 2008; Cramer, 2015).

Rocks within the Christensen Ranch Metasedimentary Suite (Acr) were identified as metasedimentary. Previous workers came to this conclusion based on distinguishable compositional layering within interlayered aluminous gneisses, schists, and dolomitic marbles (Karasevich et al., 1981; James, 1990). This study agrees with this hypothesized sedimentary protolith. Based on a single U-Pb monazite age (~2552 Ma), and the lack of Beartooth orogenic signatures in accessory monazite (2750 Ma), it was suggested that the Christensen Ranch Metasedimentary Suite was deposited between 2552-2750 Ma (Jones, 2008). However, the limited geochronological data, field observations, and the U-Pb data from this study (Aqfg: sample 15DP-A01), suggests that the Christensen Ranch Metasedimentary Suite was instead intruded by the Quartzofeldspathic Gneiss (Aqfg). This interpretation calls into question the younger age of the Christensen Ranch Metasedimentary Suite (Acr). Thus, if the Christensen Ranch Metasedimentary Suite (Acr) is older, monazite did not grow during intrusion of the adjacent Quartzofeldspathic Gneiss (Aqfg). Alternatively: 1) the screens of marble and schist within the Quartzofeldspathic Gneiss (Aqfg) may represent an older, previously undefined metasedimentary unit; 2) or the marble layers could have been structurally incorporated into the Quartzofeldspathic Gneiss (Aqfg) during later deformation.

Because the contact between these two basement units in the Ruby Range was so heavily obscured by pegmatite dikes and sills, it was impossible to definitively determine if the contact is intrusive. The two possibilities are that the contact represents a nonconformity between the units, or that the contact is intrusive. However, in some locations pegmatites and amphibolites primarily exposed in the Christensen Ranch

Metasedimentary Suite were preserved as thin layers within the Quartzofeldspathic Gneiss, suggesting that the gneiss intruded these layers. From these observations, I suggest that the Quartzofeldspathic Gneiss intruded the Christensen Ranch Metasedimentary Suite (Amr) at the contact between the units.

Basement Deformation

Foliations in the Quartzofeldspathic Gneiss (Aqfg) and the Christensen Ranch Metasedimentary Suite (Acr) in the Ruby Range are statistically indistinguishable (Figures 16 and 18). The foliation in the Quartzofeldspathic Gneiss has an average strike of 228°, and a dip of 48° northwest (n = 405) and the Christensen Ranch Metasedimentary Suite foliations have an average strike of 230° and a dip of 51° northwest (n = 170). The similar orientation of the foliations in both units suggests that they were deformed together. Work in the Tobacco Root Mountains of southwestern Montana 70 km to the northeast of the Ruby Range defined similarly-oriented ductile deformational fabrics and amphibolite facies metamorphism (Harms et al., 2004). These workers suggested that deformation occurred during northwest-southeast convergence that culminated during the northeast-trending the Big Sky orogenic belt (~1.7-1.8 Ma). In addition, recent U-Pb zircon and monazite geochronology in the Ruby Range, Tobacco Root Mountains, and Madison Range, further suggest this zone of ductile deformation occurred in a large area along a northeast-southwest trend (Condit et al., 2015). The similarity in foliation orientation, isoclinal folds, and grade of metamorphism recorded in the Ruby Range suggest that the rocks in the field area were ductilely deformed during the Big Sky orogeny.

Provenance of the Flathead Sandstone

U-Pb detrital zircon results from the lower section of the Flathead Sandstone (sample 15DP-A02; Figure 24 and Figure 25) exposed above the contact with Archean gneisses has two age-peaks at ~2798 Ma and ~2501 Ma. The sample does not record the regionally pervasive ~1780 Ma age-peak recorded in the Flathead Sandstone and other correlative middle Cambrian units in eastern Idaho, western Wyoming, and Utah (May et al., 2013; Yonkee et al., 2014; Krohe, 2016).

The two age peaks are similar to the ages of local basement, which are ~2500 and ~2800 Ma (James and Hedge, 1980; James, 1990; Jones, 2008; Cramer, 2015; this work). Derivation of grains in the basal layers of the Flathead Sandstone from proximal basement sources was also observed in western Wyoming (May et al., 2013; Malone et al., 2017). Work in the Wind River Mountains in western Wyoming examining the Flathead Sandstone found that the lower section lacked a prominent ~1780 Ma peak, but the peak was preserved in the uppermost section of the unit (May et al., 2013). Further work investigating the Flathead Sandstone in other ranges in Wyoming noted the lack of major ~1780 Ma peaks in the Flathead Sandstone, but a prominent ~2888 Ma peak likely derived from nearby basement sources (Malone et al., 2017). Malone et al. (2017) used the lack of a prominent ~1780 Ma peak in western Wyoming, and east to west paleocurrent data to suggest that grains were primarily derived from a distal southeastern source in the Cheyenne Belt or Yavapai Province rocks. From this hypothesis, they suggested that the distal source for these grains was blocked during the early deposition of the Flathead Sandstone in western Wyoming, which may explain why no prominent ~1780 Ma peak is recorded in the Flathead Sandstone exposed in Ashbough Canyon.

The two age-peaks (~2798 Ma, ~2501 Ma) recorded in the Flathead Sandstone from Ashbough Canyon do not match any of the previous data published for the Flathead Sandstone (Yonkee et al., 2014; Krohe, 2016; Malone et al., 2017). However, U-Pb zircon and monazite from the Quartzofeldspathic Gneiss from the Ruby Range and Blacktail Mountains, suggests it was intruded during the Beartooth orogeny from ~2800-2750 Ma, which could have provided a local source for the older zircons (Jones, 2008; Cramer, 2015; this study). The ~2500 Ma age-peak may have been derived from a proximal magmatic source related to the ~2450-2550 Ma Beaverhead/Tendoy orogeny (Jones, 2008; Cramer, 2015; this work). This interpretation is supported by recent work suggesting that the basal Flathead Sandstone in western Wyoming was also derived from proximal basement sources prior to the influx of ~1780 Ma grains (Malone et al., 2017)

Paleozoic units and Sevier-style deformation

Paleozoic sedimentary units in the Blacktail Mountains generally strike northeast-southwest and dip gently to the west-northwest with the exception of the Mississippian Lombard Limestone. The Lombard Limestone is intensely deformed via a combination of folds and faults above the contact with the undeformed Mississippian Kibbey Sandstone. Stratigraphically lower Cambrian through Mississippian units display minimal folding and deformation indicating they did not accommodate major shortening. This immediate change in the intensity of deformation in the Lombard Limestone at the lithologic contact with the underlying units is interpreted to indicate a Sevier-style décollement horizon at the base of the unit.

Folds within the Lombard Limestone are not restricted to any interval and are

observed from directly above the contact with the Kibbey Sandstone to the southern boundary of the study area. Previous workers in the Lombard Limestone adjacent to Mount Ashbough mapped a series of low angle reverse faults as opposed to the folds mapped in this study (Pecora, 1981; Tysdal, 1988b). These authors suggested that folds within the Lombard Limestone have minor thrust faults within their hinge zones, which is indicative of a combination of fault propagation folding and bedding plane detachments. However, mapping associated with this thesis (Plate 1) did not observe thrust faults in the hinge zones of many of the folds. Field observations suggest that the Lombard Limestone is primarily deformed via detachment folding. This interpretation is supported by observed disharmonic folding (Mitra, 2003). Folds in the Lombard Limestone are asymmetrical and verge to the east, with open anticlines and tight synclines that have axial planes that strike roughly north-south and dip west. Coupled with prior documentation of rare fault propagation folds (e.g., Tysdal, 1988b), these observations suggest a combination of detachment and fault-propagation folds, which are typically observed at the frontal edge of the fold-thrust belt (Mitra, 2003; Yonkee and Weil, 2015). These folds and faults in the Lombard Limestone likely record east-west shortening of Sevier-style deformation in southwestern Montana (Schmidt and Garihan, 1983).

Basin and Range Extension

Jake Canyon Fault Reactivation

The Jake Canyon fault is a northwest-southeast-striking, northeast-dipping, late Mesozoic to early Cenozoic, Laramide-style reverse fault (Tysdal, 1988a). A 48.1 ± 0.3 Ma Ar-Ar whole rock age for a basalt that overlies the fault's trace indicates an Eocene or

older age of displacement on the fault (Tysdal et al., 1990). The Basin and Range Blacktail fault also strikes northwest-southeast along the range front. These faults appear to merge along strike near Ashbough Canyon. Previous mapping in the Blacktail Mountains by Tysdal (1988b) and Achuff (1981) identified locations on the Blacktail Mountains range front in the immediate footwall of the Blacktail fault where Archean Quartzofeldspathic Gneiss structurally overlies Mississippian Limestones. This same relationship of older basement overlying Mississippian layers was also observed during this study near the mouth of Sheep Creek (Plate 1). In addition, a sliver of a silicified body of Archean gneiss was found along the range front west of Ashbough Canyon. Based on the older over younger structural relationship and the parallel strike of the Blacktail and Jake Canyon faults, Tysdal (1988a, 1990) suggested that the Blacktail fault reactivated portions of the Jake Canyon fault at depth. Satellite imagery and field observations from this study agree with this hypothesized fault relationship, and further suggest that the Jake Canyon fault is fully reactivated as the Blacktail fault northwest from the mouth of Ashbough Canyon (Figure 30).

I hypothesize that whether the Blacktail fault reactivated the Jake Canyon fault at the surface or at depth may be related to the pre-Basin and Range dip angle of Jake Canyon fault. Tysdal (1988a) estimated that the Jake Canyon fault dips at 45° to 75° where the footwall is within Paleozoic rocks to the northeast, and 40° to 60° where the footwall is Archean gneiss in the southeastern Blacktail Mountains. Tysdal (1988b) estimated these dip angles from field observations in locations where Archean rocks overlie Paleozoic layers. Tysdal (1988a) also suggested that the Blacktail fault has a near-vertical dip. These observations suggest that the pre-Basin and Range dip angle of the

Jake Canyon fault may have been a control on the style of reactivation by the Blacktail fault. In the northwestern Blacktail Mountains, where the Jake Canyon fault has a steeper dip, the Blacktail fault reactivates the prior plane completely (Figure 30). In contrast, in the southeastern Blacktail Mountains, the Jake Canyon fault has a shallow dip, and the Blacktail fault does not reactivate the fault at the surface.

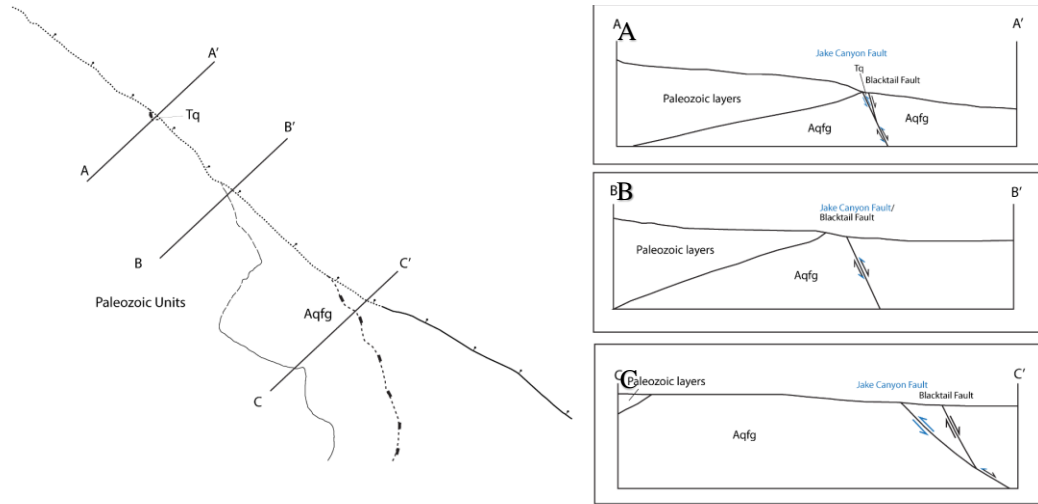


Figure 30: Schematic figure of the relationship between the dip of the Late Cretaceous Jake Canyon fault and how the Basin and Range Blacktail fault reactivates the earlier fault plane. The dip of the Jake Canyon fault was taken from estimates by Tysdal (1988a), and from observed relationships from this study. A) Cross section A-A' shows a sliver of silicified Quartzofeldspathic Gneiss (Tq) in the hanging wall of the Jake Canyon fault, and footwall of the adjacent Blacktail fault. The dip of the Jake Canyon fault is shown as 60°. B) Cross section B-B' shows a location where the Blacktail fault fully reactivates the Jake Canyon fault. The dip of the Jake Canyon fault is shown as 60°. C) Cross section C-C' shows a location where the Jake Canyon fault and the Blacktail fault diverge along strike. The dip of the Jake Canyon fault is shown at 45°. The Blacktail fault still likely reactivates the Jake Canyon fault, although not until greater depth.

The suggested reactivation of the prior Laramide-style fault by Basin and Range extension implies that the geometry of preexisting thrust faults within the Sevier-Laramide fold-thrust belt could affect the orientation of Basin and Range structures. South of the Snake River Plane, Basin and Range faults have a north-south strike, indicating an east-west extension direction, whereas Basin and Range faults north of the

Snake River Plain generally strike northwest-southeast, indicating a northeast-southwest extension direction. The current prevailing hypothesis for the northwest-southeast strike of northern Basin and Range faults suggests that extension result from uplift and heating of the lower lithosphere by the Yellowstone hotspot, providing gravitational potential that promotes extension northwest of the hotspot. However, the reactivation of the Jake Canyon fault by the Basin and Range Blacktail fault may suggest that the geometry of Basin and Range extension north of the Snake River Plain was instead controlled by the prior geometry of the Sevier-Laramide fold-thrust belt (Schmidt and Garhman, 1983; Colgan, 2013).

The orientation of northern Basin and Range extension coincides well with the shape of the preexisting Late Cretaceous fold-thrust belt. In southwestern Montana, the fold-thrust belt has a concave to the east bend in map view termed the Montana reentrant. The Blacktail fault is adjacent to a northwest-southeast striking limb of the Montana reentrant, further suggesting it may have a geometric relationship to preexisting faults. This could help explain the strike of several other Basin and Range faults that do not strike northwest-southeast such as the east-west striking Centennial fault or the northeast-southwest striking Ruby Mountains fault.

(U-Th)/He Apatite Thermochronometry

Six (U-Th)/He apatite samples were collected along a vertical transect in the Blacktail Mountains in an attempt to quantitatively constrain the timing of initial displacement on the Blacktail fault. All of the samples from the vertical transect record exhumation ages older than typical post-Miocene, Basin and Range extension, and apatite

grains in each sample record a spread of dates that are not within-error (Figure 31, see Figure 27). This spread of dates and the lack of a recorded inflection point on the age-elevation plot suggest that rocks in the footwall of the Blacktail fault were exhumed from within the partial retention zone. Based on a reasonable regional geothermal gradient (10°C surface temperature, 20°C/km), we can expect a ~75°C closure temperature to occur at ~3 km, and the partial retention zone to occur between 3-1.5 km. These apatite dates thus suggest that the footwall of the Blacktail fault was exhumed from shallower depths than ~3 km. The high relief observed at the range front may suggest that the Blacktail fault has a moderate to high slip rate (discussed in detail in section 5.5). The suspected shallow exhumation depth of the footwall combined with the estimated rapid slip rate suggests that the Blacktail fault initiated recently.

During sample collection, a previously unmapped normal fault was discovered between the collection site for 16BC-VT3 and 16BC-VT4 within the Quartzofeldspathic Gneiss (Figure 31). The significance of this fault was unknown and it was presumed that it would have a minor effect on the data. However, the data appear to show two distinct age trends, with a break at the identified fault. For the two deepest samples, the deeper sample's youngest grains are younger than the higher elevation sample. Similar, the upper three samples may also define an upward younger to older trend, with the youngest grains generally yielding younger ages than the lowest elevation samples. A preliminary interpretation of these observations is that the lower trend (16BC-VT4-16BC-VT5) was exhumed from deeper within the partial retention zone than the younger trend (16BC-VT1-16BC-VT3). The two trends are separated by the previously unmapped normal fault located between sample locations 16BC-VT3 and 16BC-VT4, suggesting

that the fault was active during exhumation of the range front.

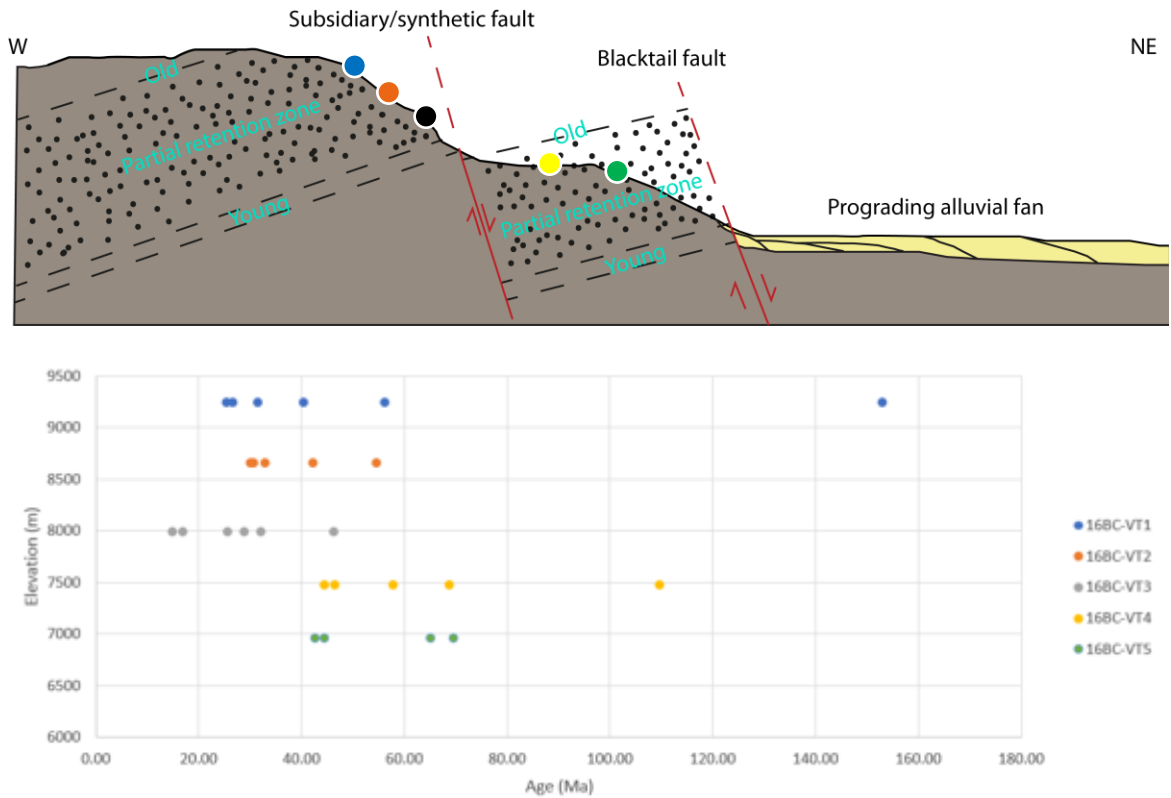


Figure 31: Schematic drawing of vertical transect sample collection elevations, and plot of the age of individual grains relative to the elevation they were collected at (see Figure 32). See text for discussion.

Geomorphic Expression of the Range Front

A geomorphic examination of the Blacktail Mountains range front was used to constrain the relative slip rates on the range-bounding Blacktail fault in the northern vs. southern Blacktail Mountains. Sinuosity calculations, which compare the length of the range front, to the length of the range front and actively eroding fans, were used to assign a value which is used as an estimate for the slip rate along range-bounding faults (Burbank and Anderson, 2012). The sinuosity values recorded for the northern ($S=1.11$) and the southern ($S=1.94$) range front of the Blacktail Mountain suggest that slip along

the southern range front is distributed among several synthetic faults adjacent to the Blacktail fault.

Observations from satellite imagery of the southeastern range front, combined with field observations during the vertical transect collection, show that there are several synthetic normal faults located in the footwall of the Blacktail fault, south of Ashbough Canyon, where the calculated sinuosity is higher ($S=1.94$). The observation that these subsidiary faults cut the active Quaternary alluvial fan surface suggests that they are also active. The presence of these active faults in the Blacktail fault's footwall, when combined with the observation that subsidiary faults are recorded in the (U-Th)/He apatite data (section 5.4), suggests that these faults may also be synthetic to the Blacktail fault.

Previous work on the Blacktail fault has indicated that the southern section of the fault has a faster slip rate than the northern (Stickney, 2007; Stickney and Bartholomew, 1987). The discrepancy between the sinuosity value calculated in this study and the suggested higher activity slip indicated by previous work may be explained by the presence of the synthetic normal faults documented here. These synthetic faults, along with the main Blacktail fault, may share the slip of Basin and Range extension across multiple fault strands south of Ashbough Canyon.

Other work within this study has suggested that there are along-strike changes from north to south in how the Blacktail fault reactivates the Jake Canyon fault (Figure 30). The change in sinuosity from low values in the north, to high values in the south occurs at the same point near Ashbough Canyon, that the Blacktail fault reactivates the Jake Canyon fault at depth. Potentially, this indicates that there is a relationship between

the geomorphic expression of the range front and the style of fault reactivation.

Timing of Initial Displacement on the Blacktail Fault

Though (U-Th)/He apatite thermochronology did not constrain the timing of initial displacement on the Blacktail fault, the dates indicate that footwall was exhumed from within the partial retention zone, and was not exhumed from depths greater than 3 km. The low calculated sinuosity value in the northern Blacktail Mountains suggests that the fault has a moderate to rapid slip rate. The high sinuosity value in the southern Blacktail Mountains is explained by the synthetic faults are observed within the footwall of the Blacktail fault from both satellite data and field observations. In addition, there is observed offset of alluvial surfaces by the Blacktail fault indicating that the fault is active. These data therefore suggest that the Blacktail fault recently initiated, is currently active, has a moderate- to rapid-slip rate, and poses a seismic hazard to southwestern Montana. The recent initiation of the Blacktail fault may be consistent with the estimated initiation time of 6-2 Ma, which was hypothesized on the basis of the migration of the Yellowstone hotspot (Pierce and Morgan, 2009).

Chapter VI: Conclusions

- Field mapping within the Ruby Range in southwestern Montana and U-Pb zircon geochronology suggest that the Quartzofeldspathic Gneiss intruded into the Christensen Ranch Metasedimentary Suite. U-Pb zircon data suggest a crystallization age older than ~2600 Ma. This older crystallization age may coincide with a previous published crystallization age of 2775 Ma (Jones, 2008).

- Mapping within the Ruby Range distinguished between two Archean basement units: a Quartzofeldspathic Gneiss, and the structurally higher Christensen Ranch Metasedimentary Suite. The presence of identical marbles surrounded by similar metasedimentary layers within both units, and the highly-intruded contact between the two units, suggests that the Quartzofeldspathic Gneiss represents a granitic intrusion into the Christensen Ranch Metasedimentary Suite
- The Flathead Sandstone overlies Archean Quartzofeldspathic Gneiss nonconformably in the Blacktail Mountains, with exposures in Ashbough Canyon. U-Pb detrital zircon analysis of the base of the Flathead Sandstone indicates that it was derived from local basement formed during the Beaverhead/Tendoy orogeny (~2501 Ma) and the Beartooth orogeny (~2798 Ma). The sample also lacks the persistent ~1780 Ma peak observed in a variety of other middle Cambrian units exposed throughout southeastern Idaho and Utah, which is consistent with local provenance of older stratigraphy within the unit.
- Cambrian through Mississippian rocks dip gently to the west, except for the Mississippian Lombard Limestone, which is highly folded and deformed. Because of the intense deformation within the Lombard Limestone, compared to the other Paleozoic units, the contact between the Kibbey Sandstone and the Lombard Limestone is interpreted as a Sevier-style décollement.
- Rocks within the Mississippian Lombard Limestone are highly deformed through a variety of detachment folds and associated faults. Folding is typically observed as broad anticlines with adjacent v-shaped synclines. Disharmonic, parasitic folds

associated with these larger structures display the same style of folding, namely detachment folding, with lesser fault propagation folding.

- The Jake Canyon fault has limited exposure within the study area but generally strikes northwest-southeast and dips at high angles to the northeast. Near Ashbough Canyon, the Jake Canyon fault merges along-strike with the Blacktail fault. The Basin and Range, Blacktail normal fault, bounds the northern range front of the Blacktail Mountains and merges along strike with the Jake Canyon fault north of Ashbough Canyon. These observations support the reactivation of the Jake Canyon fault by the Blacktail fault. This suggests that the geometry of Basin and Range faults north of the Snake River Plain may be controlled by preexisting thrust faults. The structural relief of hanging wall gneisses in the southern Ruby Range relative to Paleozoic strata in the Blacktail Mountains suggests that the majority of reverse displacement along the Jake Canyon fault has not been recovered.
- (U-Th)/He apatite samples collected from the footwall of the Blacktail fault were not fully reset. Based on a reasonable geothermal gradient, this indicates the footwall of the fault was not exhumed from depths greater than ~3 km. An apparent break observed on age-elevation plots is attributed to a previously unmapped, synthetic normal fault that was observed during sample collection. The synthetic fault is hypothesized here to be active because it drops rocks exhumed from deeper within the partial retention zone down relative to more reset samples.

- Previous work has suggested that slip on the Blacktail fault is faster to the south (Stickney, 2007). Remote sensing and geomorphic investigations of the Blacktail Mountains range front yielded sinuosity values of 1.11 for the northwestern section and 1.94 for the southeastern section. This change in sinuosity occurs at Ashbough Canyon where the Blacktail fault no longer fully reactivates the Jake Canyon fault, suggesting that there is a geomorphic expression associated with the style of fault reactivation. Satellite imagery also showed that several synthetic faults cut topography southeast of Ashbough Canyon, where the sinuosity value is higher. The presence of these synthetic faults, combined with the suggested faster slip rate, indicates that extension on the Blacktail fault is diffuse along several fault strands south of Ashbough Canyon.

Works cited

- Achuff, J., 1981, Folding and faulting in the northern Blacktail Range, Beaverhead County, Montana: University of Montana, M.S. Thesis, 64 p.
- Alcock, J., and Muller, P., 2012, A Paleoproterozoic sedimentary basin within the Wyoming craton exposed in the Ruby Range, SW, Montana: identified by field relations and geochronology: *Northwest Geology*, p. 47–62.
- Alcock, J., Muller, P., and Jercinovic, M., 2013, Monazite ages and pressure–temperature–time paths from anatexites in the southern Ruby Range, Montana, USA: evidence for delamination, ultramafic magmatism, and rapid uplift at ca. 1780 Ma: *Canadian Journal of Earth Sciences*, v. 50, p. 1069–1084, doi: 10.1139/cjes-2013-0035.
- Anders, M., 1994, Constraints on North American plate velocity from the Yellowstone hotspot deformation field: *Nature*, v. 369, p. 53–55.
- Anders, M., Geissman, J., Piety, L., and Sullivan, J., 1989, Parabolic distribution of circumeastern Snake River Plain seismicity and latest Quaternary faulting: Migratory pattern and association with the Yellowstone hotspot: *Journal of Geophysical Research*, v. 94, p. 1589, doi: 10.1029/JB094iB02p01589.
- Anders, M., Rodgers, D., Hemming, S., Saltzman, J., DiVenere, V., Hagstrum, J., Embree, G., and Walter, R., 2014, A fixed sublithospheric source for the late Neogene track of the Yellowstone hotspot: Implications of the Heise and Picabo volcanic field: *Journal of Geophysical Research: Solid Earth*, v. 119, p. 5814–5829,

doi: 10.1002/2013JB010483.

Anderson, N., 2017, The Bloody Dick and Maiden Peak gneisses, southwest Montana: Implications for Archean and Paleoproterozoic basement framework: Idaho State University, M.S. Thesis, 120 p.

Anderson, D., 1987, Timing and mechanism of formation of selected talc deposits in the Ruby Range, Southwestern Montana: Montana State University, M.S. Thesis, 90 p.

Anderson, D., Mogk, D., and Childs, J., 1990, Petrogenesis and timing of talc formation in the Ruby Range, southwestern Montana: *Economic Geology*, v. 85, p. 585–600, doi: 10.2113/gsecongeo.85.3.585.

Brady, J.B., Mohlman, H.K., Harris, C., Carmichael, S.K., Jacob, L.K., and Chaparro, W.R., 2004, General geology and geochemistry of metamorphosed Proterozoic mafic dikes and sills, Tobacco Root Mountains, Montana, *in* Brady, J.B., Burger, H.R., Cheney, J.T., and Harms, T.A., eds., *Precambrian geology of the Tobacco Root Mountains, Montana: Geological Society of America Special Paper 377*, p. 89–104.

Burbank, D., and Anderson, R., 2012, *Tectonic Geomorphology*: Wiley-Blackwell, 454 p.

Bush, J., Thomas, R., and Pope, M., 2012, Sauk megasequence deposition in northeastern Washington, northern Idaho, and western Montana, *in* J. R. Derby, R. D. Fritz, S. A. Longacre, W. A. Morgan, and C. A. Sternbach, eds., *The great American carbonate bank: The geology and economic resources of the Cambrian – Ordovician Sauk*

- megasequence of Laurentia: AAPG Memoir 98, p. 751 – 768.
- Cherniak, D.J., and Watson, E.B., 2001, Pb diffusion in zircon: *Chemical Geology*, v. 172, p. 5–24, doi: 10.1016/S0009-2541(00)00233-3.
- Chamberlain, K., Frost, C., and Frost, B., 2003, Early Archean to Mesoproterozoic evolution of the Wyoming Province: Archean origins to modern lithospheric architecture: *Canadian Journal of Earth Sciences*, v. 40, p. 1357–1374, doi: 10.1139/e03-054.
- Cheney, J.T., Webb, A.A.G., Coath, C.D., and McKeegan, K.D., 2004. In situ ion microprobe $^{207}\text{Pb}/^{206}\text{Pb}$ dating of monazite from Precambrian metamorphic suites, Tobacco Root Mountains, Montana. In *Precambrian geology of the Tobacco Root Mountains, Montana*. Edited by J.B. Brady, H.R. Burger, J.T. Cheney, and T.A. Harms: Geological Society of America, Special Paper 377, pp. 151-180.
- Colgan, J., 2013, Reappraisal of the relationship between the northern Nevada rift and Miocene extension in the northern Basin and Range Province: *Geology*, v. 41, p. 211–214, doi: 10.1130/G33512.1.
- Condit, C., Mahan, K., Ault, A., and Flowers, R., 2015, Foreland-directed propagation of high-grade tectonism in the deep roots of a Paleoproterozoic collisional orogen, SW Montana, USA: *Lithosphere*, p. 625–645, doi: 10.1130/L460.1.
- Cramer, M., 2015, Proterozoic tectonometamorphic evolution of the Ruby Range, SW Montana, USA: Insights from phase equilibria modeling and in situ monazite petrochronology: University of Montana, M.S. Thesis, 120 p.

- Desmarais, N., 1981, Metamorphosed Precambrian ultramafic rocks in the Ruby Range, Montana: *Precambrian Research* v.16, pp. 67-101
- Ehlers, T., and Farley, K., 2003, Apatite (U-Th)/He thermochronometry: Methods and applications to problems in tectonic and surface processes: *Earth and Planetary Science Letters*, v. 206, p. 1–14, doi: 10.1016/S0012-821X(02)01069-5.
- Flowers, R., Shuster, D., Wernicke, B., and Farley, K., 2007, Radiation damage control on apatite (U-Th)/He dates from the Grand Canyon region, Colorado Plateau: *Geology*, v. 35, p. 447–450, doi: 10.1130/G23471A.1.
- Foster, D., Mueller, P., Mogk, D., Wooden, J., and Vogl, J., 2006, Proterozoic evolution of the western margin of the Wyoming craton: implications for the tectonic and magmatic evolution of the northern Rocky Mountains: *Canadian Journal of Earth Science*, v. 43, p. 1601–1619, doi: 10.1139/e06-052.
- Garihan, J., 1979, Geology and structure of the central Ruby Range, Madison County, Montana: *Bulletin of the Geological Society of America*, v. 90, p. 695–788, doi: 10.1130/GSAB-P2-90-695.
- Harms, T., Brady, J., Burger, H., and Cheney, J., 2004, Advances in the geology of the Tobacco Root Mountains, Montana, and their implications for the history of the northern Wyoming province: *Geological Society of America Special Paper*, v. 377, p. 227–243, doi: 10.1130/0-8137-2377-9.227.
- Heinrich, E., 1949, Pegmatites of Montana: *Economic Geology*, v. 44, p. 307–335.
- Heinrich, E., 1960, *Geology of the Ruby Mountains and nearby areas in southwestern*

- Montana, *in* pre-Beltian geology of the Cherry Creek and Ruby Mountains areas, southwestern Montana: Montana Bureau of Mines and Geology Memoir 38, p. 15–38.
- James, H., 1990, Precambrian geology and bedded iron deposits of the southwestern Ruby Range, Montana: USGS Professional Paper, v. 1495, p. 1–39.
- James, H., and Hedge, C., 1980, Age of the basement rocks of southwest Montana.: Geological Society of America Bulletin, v. 91, p. 11–15.
- Janecke, S., 1994, Sedimentation and paleogeography of an Eocene to Oligocene rift zone, Idaho and Montana: Geological Society of America Bulletin, v. 106, p. 1083–1095, doi: 10.1130/0016-7606(1994)106<1083:SAPOAE>2.3.CO;2.
- Janecke, S., 2007, Cenozoic extensional processes and tectonics in the northern Rocky Mountains: southwest Montana and eastern Idaho: Northwest Geology, v. 36, p. 111–132.
- Jones, C., 2008, U-Pb geochronology of monazite and zircon in Precambrian metamorphic rocks from the Ruby Range, SW Montana: Deciphering geological events that shaped the NW Wyoming province: Kent State University, M.S. Thesis, 119 p.
- Karasevich, L., Garihan, J., Dahl, P., and Okuma, A., 1981. Summary of Precambrian metamorphic and structural history, Ruby Range, southwest Montana: Montana Geological Society Field Conference and Symposium Guidebook to Southwest Montana, p. 225-237.

- Krohe, N., 2016, Structural Framework and Detrital Zircon Provenance of the Southern Portion of the Clayton Quadrangle Custer County, Idaho: Idaho State University, M.S. Thesis, 107 p.
- Kulik, D., and Perry, W., 1988, Evidence for the overlap province in southwestern Montana, *in* Schmidt, C. and Perry, W. eds., Interaction of the Rocky Mountain Foreland and the Cordilleran Thrust Belt, Geological Society of America Memoir 171, v. 171, p. 291–306.
- Kulik, D., and Schmidt, C., 1988, Region of overlap and styles of interaction of Cordilleran thrust belt and Rocky Mountain foreland, *in* Schmidt, C. and Perry, W. eds., Interaction of the Rocky Mountain Foreland and the Cordilleran Thrust Belt, Geological Society of America Memoir 171, v. 171, p. 75–98.
- Ludwig, K., 2012. User's manual for Isoplot version 3.75–4.15: a geochronological toolkit for Microsoft Excel: Berkley Geochronological Center Special Publication No. 5.
- Malone, D., Craddock, J., and Kenderes, S., 2017, Detrital zircon geochronology and provenance of the Middle Cambrian Flathead Sandstone, Park County, Wyoming: *The Mountain Geologist*, v. 52, p. 86–103.
- May, S., Gray, G., Summa, L., Stewart, N., Gehrels, G., and Pecha, M., 2013, Detrital zircon geochronology from the Bighorn Basin, Wyoming, USA: Implications for tectonostratigraphic evolution and paleogeography: *Geological Society of America Bulletin*, v. 125, p. 1403–1422, doi: 10.1130/b30824.1.

- McDowell, R., 1997, Evidence for synchronous thin-skinned and basement deformation in the Cordilleran fold-thrust belt: the Tendoy Mountains, southwestern Montana: *Journal of Structural Geology*, v. 19, p. 77–87, doi: 10.1016/S0191-8141(96)00044-2.
- Mitra, S., 2003, A unified kinematic model for the evolution of detachment folds: *Journal of Structural Geology*, v. 25, p. 1659–1673, doi: 10.1016/S0191-8141(02)00198-0.
- Mogk, D. and Henry, D., 1988, Metamorphic petrology of the Northern Archean Wyoming Province, southwestern Montana: evidence for Archean collisional tectonics, *in* Ernst, W.G., ed., *Metamorphism and Crustal Evolution of the Western United States*, vol. 7. Prentice-Hall, p. 362-382.
- Mueller, P., Wooden, J., Mogk, D., and Foster, D., 2011, Paleoproterozoic evolution of the Farmington zone: Implications for terrane accretion in southwestern Laurentia: *Lithosphere*, v. 3, p. 401–408, doi: 10.1130/L161.1.
- Mueller, P.A., Mogk, D.W., Wooden, J., and Spake, D., 2016, U-Pb ages of zircons from the Lower Belt Supergroup and proximal crystalline basement: implications for the early evolution of the Belt Basin, *in* MacLean, J.S., and Sears, J.W., eds., *Belt Basin: Window to Mesoproterozoic Earth: Geological Society of America Special Paper*, v. 522, p. 283–303.
- O'Neill, J.M., Lopez, D.A., 1985, Character and significance of Great Falls tectonic zone, east-central Idaho and west-central Montana: *American Association of Petroleum Geologists Bulletin*, v. 69, p. 437–447.

- Paton, C., Hellstrom, J., Paul, B., Woodhead, J., and Hergt, J., 2011, Iolite: freeware for the visualisation and processing of mass spectrometric data. *Journal of Analytical Atomic Spectrometry*, v.26, p.2508-2518.
- Pecora, W., 1981, Bedrock geology of the Blacktail Mountains, south-western Montana, M.S. thesis, Wesleyan University, M.S. Thesis, 203 p.
- Pecora, W., 1987, Geologic map of frontal fold and thrust zone in the Blacktail Mountains, Beaverhead County, Montana: scale 1:24,000.
- Pierce, K., and Morgan, L., 1992, The track of the Yellowstone hot spot: Volcanism, faulting, and uplift, *in* Link, P.K., Kuntz, M.A., and Piatt, L.B. eds., *Regional Geology of Eastern Idaho and Western Wyoming*, Geological Society of America Memoir, v. 179, p. 1–54.
- Pierce, K., and Morgan, L., 2009, Is the track of the Yellowstone hotspot driven by a deep mantle plume? — Review of volcanism, faulting, and uplift in light of new data: *Journal of Volcanology and Geothermal Research*, v. 188, p. 1–25, doi: 10.1016/j.jvolgeores.2009.07.009.
- Proffett, J., 1977, Cenozoic geology of the Yerington district, Nevada, and implications for the nature and origin of Basin and Range faulting: *Geological Society of America Bulletin*, v. 88, p. 247–266.
- Reiners, P., and Brandon, M., 2006, Using thermochronology to understand orogenic erosion: *Annual Review of Earth and Planetary Sciences*, v. 34, p. 419–466, doi: 10.1146/annurev.earth.34.031405.125202.

- Roberts, H., Dahl, P., Kelley, S., and Frei, R., 2002, New 207 Pb-206 Pb and 40 Ar-39 Ar ages from SW Montana, USA: Constraints on the Proterozoic and Archaean tectonic and depositional history of the Wyoming Province: *Precambrian Research*, v. 117, no. 1–2, p. 119– 143.
- Rodgers, D., Ore, H., Bobo, R., McQuarrie, N., and Zentner, N., 2002, Extension and subsidence of the eastern Snake River Plain, Idaho, *in* Bonnichsen, B., White, C.M., and McCurry, M., eds., *Tectonic and Magmatic Evolution of the Snake River Plain Volcanic Province: Idaho Geological Survey Bulletin*, v. 30, p. 121–155.
- Royse, F., Jr, Warner, M.A., and Reese, D.L., 1975, Thrust belt structural geometry and related stratigraphic problems Wyoming-Idaho-northern Utah: *Rocky Mountain Association of Geologists, 1975 Symposium, Rocky Mountain Association of Geologists*, p. 41–54.
- Ruppel, E.T., and Lopez, D.A., 1984, The thrust belt in southwest Montana and east-central Idaho: *Geological Survey Professional Paper*, v. 1278, p. 41.
- Ruppel, E.T., Lopez, D.A., and O'Neill, J.M., 1993, *Geologic map of the Dillon 1° by 2° Quadrangle, Idaho and Montana: Scale 1:250,000.*
- Schmidt, C., and Garihan, J., 1983, Laramide tectonic development of the Rocky Mountain foreland of southwestern Montana, *in* Lowell, J. and Gries, R. eds., *Rocky Mountain foreland basins and uplifts Rocky Mountain Association of Geologists, Rocky Mountain Association of Geologists*, p. 271–294.
- Sears, J., Hendrix, M., Thomas, R., and Fritz, W., 2009, Stratigraphic record of the

- Yellowstone hotspot track, Neogene Sixmile Creek Formation grabens, southwest Montana: *Journal of Volcanology and Geothermal Research*, v. 188, p. 250–259, doi: 10.1016/j.jvolgeores.2009.08.017.
- Sloss, L., 1950, Paleozoic Sedimentation in Montana Area: *Bulletin of the American Association of Petroleum Geologists*, v. 34, p. 423–451.
- Sonder, L., and Jones, C., 1999, Western United States extension: how the west was widened: *Annual Review of Earth and Planetary Sciences*, v. 27, p. 417–462, doi: 10.1146/annurev.earth.27.1.417.
- Stickney, M., 2007, Historic earthquakes and seismicity in southwestern Montana: *Northwest Geology*, v. 36, p. 167–186.
- Stickney, M., and Bartholomew, M., 1987, Seismicity and late Quaternary faulting of the northern Basin and Range province, Montana and Idaho: *Bulletin of the Seismological Society of America*, v. 77, p. 1602–1625.
- Stockli, D., 2005, Application of low-temperature thermochronometry to extensional tectonic settings: *Reviews in Mineralogy and Geochemistry*, v. 58, p. 411–448, doi: 10.2138/rmg.2005.58.16.
- Stroup, C., Link, P., and Fanning, C., 2008a, Provenance of Late Miocene fluvial strata of the Sixmile Creek Formation, southwest Montana: Evidence from detrital zircon: *Northwest Geology*, v. 37, p. 69–84.
- Stroup, C., Link, P., Janecke, S., Fanning, C., Yaxley, G., and Beranek, L., 2008b, Eocene to Oligocene provenance and drainage in extensional basins of southwest

- Montana and east-central Idaho: Evidence from detrital zircon populations in the Renova Formation and equivalent strata, *in* Spencer, J.E., and Titley, S.R., eds., Circum-Pacific tectonics, geologic evolution, and ore deposits: Arizona Geological Survey Digest 22, p. 529–546.
- Thomas, R., 2007, A field guide to the Cambrian section at Camp Creek, southwest Montana: Northwest Geology, v. 36, p. 231–244.
- Thomas, R., and Roberts, S., 2007, A summary of the stratigraphy and depositional setting of Paleozoic rocks in the Dillon area: Northwest Geology, v. 36, p. 35–56.
- Tysdal, R., 1988a, Deformation along the northeast side of Blacktail Mountains salient, southwestern Montana, *in* Schmidt, C.J. and Perry, W.J. eds., Interaction of the Rocky Mountain Foreland and the Cordilleran Thrust Belt, Geological Society of America Memoir 171, v. 171, p. 203–216.
- Tysdal, R., 1988b, Geologic map of the northeast flank of the Blacktail Mountains, Beaverhead County, Montana: scale 1:24,000.
- Tysdal, R., Zimmermann, R., Wallace, A., and Snee, L., 1990, Geologic and Fission-Track Evidence for Late Cretaceous Faulting and Mineralization, Northeastern Flank of Blacktail Mountains, Southwestern Montana: U.S. Geological Survey Bulletin, v. 1922.
- Wardlaw, B., and Pecora, W., 1985, New Mississippian-Pennsylvanian stratigraphic units in southwest Montana and adjacent Idaho, *in* Sando, W.J. ed., Mississippian and Pennsylvanian stratigraphy in southwest Montana and adjacent Idaho, U.S. Geologic

Survey Bulletin, v. 1656, p. B1–B9.

Wooden, J., Vitaliano, C., Koehler, S., and Ragland, P., 1978, The late Precambrian mafic dikes in the southern Tobacco Root Mountains, Montana Geochemistry, Rb-Sr geochronology, and relationship to Belt tectonics: *Canadian Journal of Earth Sciences*, v. 15, p. 467-479.

Yonkee, W., Dehler, C., Link, P., Balgord, E., Keeley, J., Hayes, D., Wells, M., Fanning, C., and Johnston, S., 2014, Tectono-stratigraphic framework of Neoproterozoic to Cambrian strata, west-central U.S.: Protracted rifting, glaciation, and evolution of the North American Cordilleran margin: *Earth-Science Reviews*, v. 136, p. 59–95, doi: 10.1016/j.earscirev.2014.05.004.

Yonkee, W., and Weil, A., 2015, Tectonic evolution of the Sevier and Laramide belts within the North American Cordillera orogenic system: *Earth-Science Reviews*, v. 150, p. 531–593, doi: 10.1016/j.earscirev.2015.08.001.

Appendix A: Locations of collected hand samples

Sample	Unit	Lat	Long	Notes
16BC-02	Aqfg	45.018	122.5678	Diorite sill within the quartzofeldspathic gneiss
16BC-03	Cf	45.01816	122.56797	Clasts from the breccia at the base of the Flathead Sandstone
16BC-05	MIb	45.01945	112.6082	Gray/Black fossil bearing limestone from the northwest side of Mt. Ashbough
16BC-06	MIb	45.01887	112.60197	Gray/Red limestone with calcite veins parallel to bedding
16BC-07	MIb	45.01625	112.61433	thinly bedded limestone and calcitic shale containing large brachiopods
16BC-08	Mmc	45.05001	112.61633	Clasts from the breccia within the Mission Canyon Limestone
16BC-09	Pq	45.04686	112.62297	Quadrant sandstone collected near Sheep Creek
16BC-20	Aqfg	45.05755	112.5137	Quartzofeldspathic Gneiss collected near the Blacktail-deer Creek
16BC-21	Am	45.05993	112.51537	Aluminous schist adjacent and interlayered with dolomitic marble
16BC-23	Am	45.05991	112.51539	Dolomitic marble
16BC-24	Aqfg	45.01002	112.55543	garnet-biotite gneiss southeast of the mouth of Ashbough Canyon
16BC-25	Acr	45.10088	112.52342	sillimanite gneiss interlayered with sillimanite and biotite schist
16BC-26	Acr	45.09956	112.54048	Amphibolite sill within the Christensen Ranch
16BC-27	Ams	45.1039	112.52106	Dolomitic marble
16BC-28	Amr	45.11763	112.50732	Aluminous schist within the Christensen Ranch
16BC-29	Amr	45.1037	112.54341	Pegmatite
16BC-30	Amr	45.11227	112.54221	Pegmatite with biotite sheets
16BC-30a	Aqfg	45.09568	112.50397	Quartzofeldspathic Gneiss
16BC-31	Amr	45.10118	112.54301	Pegmatite

Appendix B: U-Pb Zircon Data

Appendix B includes the U-Pb zircon analysis results from samples 15DP-A01 and 15DP-A02. Sample 15DP-A01 was collected from the Quartzofeldspathic Gneiss (Aqfg) within Ashbough Canyon. Sample 15DP-A02 was collected from the base of the Flathead Sandstone within Ashbough Canyon.

Sample ID	Lat (N)	Long (W)
15DP-A01	45.018611	-112.565556
15DP-A02	45.018333	-112.567778

15DP-A01

Sample/Analysis	238/206	207/206	207 corr. age	206/238 age error	207/235 age	207/206 Age	% discordance	U (ppm)	2 sig err.	Th (ppm)	2 sig err U/Th									
X15DP_A01_01	6.68963711	0.297176249	0.1785	0.00150436	0.900	783.5	33.8	898	40	1565	72	2639	22	42.60475887	BA0	9.74E+04	2.40E+03	2711	16.3	5.9E+01
X15DP_A01_02	2.720083102	0.095252968	0.172099	0.00048261	1.001	1861.4	63.9	1987	67	2300	75	2567	7	13.60023476	CO0D	12100	680	346	16.3	5.0E+01
X15DP_A01_03	4.188851821	0.112918732	0.19232	0.00058318	0.942	1209.2	31.6	1381	37	2046	44	2762	8	52.50033552	BA0	15330	410	389.4	9.8	3.9E+01
X15DP_A01_04	2.19252234	0.037022569	0.1644	0.00110304	1.046	2381.1	68.3	2416	63	2476	47	2501	17	2.435722298	CO0D	621	110	40.1	4.1	1.5E+01
X15DP_A01_05	12.77159208	0.636894004	0.1668	0.00160357	0.869	423.9	48.2	486	24	1054	54	2526	24	53.88276503	BA0	10770	320	365	18.2	9.5E+01
X15DP_A01_06	12.88659794	1.03359827	0.1585	0.00140368	0.868	1802.2	54.8	1960	60	2370	58	2446	22	5.0959319	BA0	20940	550	569	18.3	7.5E+01
X15DP_A01_07	2.813731007	0.08620727	0.18321	0.00060151	0.998	820.2	33.4	882	39	1027	54	2426	9	17.28524081	BA0	4899	95	303.6	7	1.6E+01
X15DP_A01_08	6.451612903	0.509950887	0.1705	0.00180331	0.903	1133.4	34.9	929	73	1593	134	2563	27	41.67748248	BA0	5.02E+04	1.70E+03	648	37	7.7E+01
X15DP_A01_09	4.42282176	0.140272558	0.1976	0.00120667	0.936	1820.4	83.9	1914	42	2279	119	2806	17	35.51563311	BA0	1.14E+05	3.90E+03	2057	52	5.52E+01
X15DP_A01_10	3.125	0.16399381	0.17998	0.00078838	0.981	1632.4	83.9	1990	94	2279	119	2806	12	45.3658505	BA0	8.24E+04	2.70E+03	962	28	8.57E+01
X15DP_A01_11	7.535795026	0.29267571	0.17369	0.00060041	0.893	702.5	26.5	803	31	1469	54	2594	9	12.49370764	CO0D	3200	130	146.9	5.2	1.8E+01
X15DP_A01_12	2.403268445	0.068819923	0.1931	0.00170451	1.028	2083.2	61.6	2243	64	2563	67	2769	24	14.9370764	CO0D	8.05E+04	1.50E+03	755	22	1.07E+02
X15DP_A01_13	5.780346821	0.575431387	0.1722	0.00190321	0.911	909.9	87.6	1029	102	1718	175	2579	29	40.12581812	BA0	4.63E+04	1.00E+03	1488	31	3.1E+01
X15DP_A01_14	14.83679825	1.082755638	0.1581	0.00430119	0.864	370.2	26.6	420	31	930	68	2435	66	54.80671787	BA0	39450	630	1127	38	3.50E+01
X15DP_A01_15	14.14427157	0.641109493	0.15801	0.00069739	0.865	388.0	17.3	440	20	947	42	2434	11	53.49354688	BA0	5.06E+04	2.40E+03	1127	67	3.50E+01
X15DP_A01_16	15.3609831	0.704576556	0.149	0.00150353	0.863	362.1	16.3	407	19	878	37	2334	20	53.68748579	BA0	5.06E+04	2.40E+03	1127	67	3.50E+01
X15DP_A01_17	5.745825388	0.313865824	0.2195	0.00270366	0.912	852.9	45.5	1035	57	1897	104	2977	37	45.47148392	BA0	27070	730	5560	190	4.87E+00
X15DP_A01_18	10.03009027	0.359423672	0.2391	0.00300391	0.878	485.1	17.2	613	22	1486	54	3114	39	58.76534712	BA0	25570	790	409	18	6.25E+01
X15DP_A01_19	8.771929825	0.721579377	0.1888	0.00340215	0.884	593.8	47.6	696	57	1405	122	2732	49	50.46996154	BA0	27090	460	804	21	3.37E+01
X15DP_A01_20	9.718172983	0.826841116	0.1727	0.00150408	0.879	549.3	45.6	631	54	1292	111	2584	23	51.13668494	BA0	4.88E+04	1.60E+03	1215	43	4.02E+01
X15DP_A01_21	7.042253521	0.556949922	0.195	0.00170459	0.897	728.9	55.9	856	68	1632	131	2785	24	47.55664162	BA0	32220	830	12260	320	2.63E+00
X15DP_A01_22	13.29787234	1.09301708	0.14102	0.00059688	0.867	421.5	34.1	467	39	942	80	2240	9	50.4075429	BA0	34820	800	876	24	3.97E+01
X15DP_A01_23	24.03846154	2.172081732	0.1279	0.00170198	0.853	239.4	21.4	263	24	562	62	2069	28	53.23381501	BA0	8.86E+04	2.80E+03	2419	93	3.66E+01
X15DP_A01_24	7.102272727	0.399719069	0.2184	0.00370265	0.896	699.6	38.4	849	48	1703	110	2569	50	50.13294395	BA0	8.18E+04	2.50E+03	2167	59	3.77E+01
X15DP_A01_25	14.55604076	0.919623436	0.1921	0.00190399	0.882	373.7	23.2	428	27	978	60	2761	49	56.20425506	BA0	32790	990	3880	260	8.45E+00
X15DP_A01_26	9.225092251	0.688013004	0.1922	0.00190399	0.882	562.8	41.0	663	49	1371	105	2761	27	51.62411914	BA0	14390	270	526	12	1.274E+01
X15DP_A01_27	23.4741784	1.587603129	0.12541	0.00080403	0.853	245.8	16.4	269	18	582	38	2035	13	53.78670138	BA0	40420	860	988	20	4.09E+01
X15DP_A01_28	5.405405405	0.332743176	0.17184	0.00094643	0.917	971.2	57.7	1094	67	1733	115	2376	14	36.8324623	BA0	12650	320	881	11	4.50E+01
X15DP_A01_29	8.673026886	0.508091775	0.16996	0.00094629	0.885	615.9	35.1	703	41	1323	79	2557	14	46.82707828	BA0	29580	570	583	13	5.02E+01
X15DP_A01_30	4.633920297	0.196894311	0.19094	0.00095485	0.931	1098.2	45.1	1260	54	1948	84	2750	14	35.3338267	BA0	19730	270	370.7	7.2	5.3E+01
X15DP_A01_31	31.44654088	1.197652264	0.11732	0.00081348	0.849	186.0	7.0	202	8	422	16	1916	13	52.23304406	BA0	31430	550	950	19	3.31E+01
X15DP_A01_32	13.22751323	1.019344799	0.1813	0.00230293	0.868	401.6	30.4	470	36	1098	90	2655	34	57.23001463	BA0	4.41E+04	1.00E+03	1120	51	3.94E+01
X15DP_A01_33	12.0369434	0.582733356	0.2012	0.00160519	0.871	428.7	20.4	515	25	1227	62	2836	23	58.38629984	BA0	5.66E+04	1.00E+03	1381	25	4.40E+01
X15DP_A01_34	14.24501425	1.039686325	0.1862	0.00220324	0.865	371.0	26.6	437	32	1042	81	2709	32	58.01982519	BA0	5.20E+04	2.50E+03	1352	35	3.85E+01
X15DP_A01_35	14.45086705	0.68710421	0.1837	0.00240289	0.865	362.0	17.2	431	21	1036	50	2687	35	58.36489127	BA0	28330	700	1010	34	2.80E+01
X15DP_A01_36	33.44481605	2.299202949	0.1583	0.00110467	0.848	165.9	11.3	190	13	514	33	2438	17	63.0503103	BA0	34200	860	1052	27	3.25E+01
X15DP_A01_37	4.975124378	0.170535719	0.19612	0.00074075	0.924	1018.3	33.8	1181	81	1899	134	2794	11	37.8683373	BA0	19100	900	1622	39	1.18E+01
X15DP_A01_38	2.793286089	0.105672421	0.18511	0.00071985	0.999	1810.5	66.8	1973	73	2369	79	2699	10	16.72293863	BA0	8310	180	226.4	4.7	3.67E+01
X15DP_A01_39	4.405286344	0.206372375	0.17002	0.00073809	0.936	1185.9	53.6	1319	62	1861	92	2558	11	29.12385801	BA0	11300	290	287	19	3.94E+01
X15DP_A01_40	3.900350033	1.209542969	0.11089	0.00096263	0.848	178.8	6.5	192	7	384	14	1814	16	49.83202341	BA0	33290	380	156	19	2.10E+01
X15DP_A01_41	9.99000999	0.561943101	0.11797	0.000230301	0.878	529.7	29.1	615	35	1286	76	2850	32	52.19398745	BA0	3.92E+04	1.30E+03	1047	31	3.74E+01

15DP-A02

Sample/Analysis	238/206	±	207/206	±	207 corr. age	±	206/238 age	error	207/235 age ±	207/206 Age ±	% discordance				
15DP_A02_095	2.419549964	0.031065031	0.15839	0.003148298	1.03	2183.48272	29.5	2229.98936	28.6	2338.00621	56	2438.5482	48	4.620041137	GOOD
15DP_A02_093	2.236135957	0.033032249	0.1641	0.003188476	1.04	2351.825176	37.4	2382.79026	35.2	2443.97162	59	2498.35191	49	2.503357863	GOOD
15DP_A02_125	2.229654404	0.020431217	0.16533	0.003170741	1.04	2355.454841	24.3	2388.57838	21.9	2453.29556	52	2510.91606	48	2.636540147	GOOD
15DP_A02_084	2.428363283	0.037182457	0.16783	0.003240844	1.03	2151.539235	34.3	2223.14386	34	2390.44388	59	2536.12017	49	6.998701085	GOOD
15DP_A02_037	2.245677072	0.01821042	0.18564	0.003554981	1.04	2280.800789	21.5	2374.32134	19.3	2547.87466	53	2703.91657	52	6.811689901	GOOD
15DP_A02_094	2.051702913	0.018567062	0.18619	0.003594967	1.06	2507.13828	27.2	2559.41525	23.2	2639.71436	57	2708.79816	52	3.041962325	GOOD
15DP_A02_019	2.222716159	0.027208852	0.18649	0.003578741	1.04	2302.727397	30.9	2394.80594	29.3	2539.91603	58	2711.45384	52	5.713184679	GOOD
15DP_A02_090	1.953125	0.038166936	0.18838	0.003644957	1.07	2639.93174	59.8	2665.15987	52.1	2703.31078	75	2728.07209	53	1.411266032	GOOD
15DP_A02_054	1.9462826	0.023517885	0.1919	0.003782461	1.07	2637.842083	38.5	2672.8296	32.3	2720.17566	61	2758.51638	54	1.740551519	GOOD
15DP_A02_002	2.265518804	0.024165554	0.19192	0.003688005	1.04	2242.949896	26.6	2356.90283	25.1	2618.36919	58	2758.68751	53	9.98584764	GOOD
15DP_A02_064	1.990049751	0.024586034	0.1922	0.003949512	1.07	2572.03169	37.7	2624.52886	32.4	2702.60196	62	2761.08128	57	2.888812184	GOOD
15DP_A02_117	2.174858634	0.026051337	0.1928	0.003888717	1.05	2336.986654	31.3	2438.67279	29.2	2638.2045	63	2766.19279	56	7.563163022	GOOD
15DP_A02_102	1.938735944	0.023336107	0.19318	0.003719304	1.08	2644.868981	38.5	2681.34084	32.3	2736.07916	61	2769.42797	53	2.000611864	GOOD
15DP_A02_097	1.846722068	0.027989477	0.1956	0.003938921	1.09	2789.668483	53.3	2789.72183	42.3	2788.23011	66	2796.76379	56	-0.053500433	GOOD
15DP_A02_103	1.85528757	0.031001007	0.1934	0.003809968	1.09	2783.029589	57.8	2779.25858	46.4	2779.72218	64	2771.29705	55	0.016678078	GOOD
15DP_A02_021	1.907304978	0.019681131	0.1955	0.003937127	1.08	2686.140827	35.1	2717.38874	28	2729.88568	63	2788.99493	56	0.457782614	GOOD
15DP_A02_110	1.857700167	0.033840659	0.1941	0.004021675	1.09	2775.903879	62.6	2776.32582	50.6	2794.07874	68	2777.21944	58	0.635376433	GOOD
15DP_A02_078	1.89000189	0.016475046	0.19731	0.003813657	1.08	2707.755633	31.1	2737.6565	23.9	2777.74865	58	2804.07617	54	1.443332445	GOOD
15DP_A02_096	1.892147588	0.026520618	0.19677	0.003793137	1.08	2706.23644	46.3	2735.12651	38.3	2776.43082	68	2799.59348	54	1.487676586	GOOD
15DP_A02_087	1.92566917	0.023393346	0.19643	0.003790142	1.08	2653.453353	32.9	2696.20851	32.8	2754.4361	62	2796.76379	54	2.113956872	GOOD
15DP_A02_079	1.920491646	0.019585568	0.19659	0.003802026	1.08	2661.016067	33.9	2702.14599	27.6	2761.15162	59	2798.09611	54	2.136993509	GOOD
15DP_A02_047	1.949697797	0.016013025	0.1947	0.003922775	1.07	2622.672266	27.9	2668.99588	21.9	2727.81277	64	2782.278	56	2.156192349	GOOD
15DP_A02_116	1.932740626	0.019835719	0.19564	0.003763928	1.08	2645.289349	33.7	2688.14174	27.6	2765.15972	61	2790.16715	54	2.785299448	GOOD
15DP_A02_108	2.044989775	0.029302395	0.19566	0.003770674	1.06	2485.37642	40.3	2566.34594	36.8	2713.88411	62	2790.33453	54	5.436241154	GOOD
15DP_A02_109	2.0733983	0.025397808	0.19677	0.003783634	1.06	2445.34491	34.1	2537.27381	31.1	2699.05042	64	2799.59348	54	5.993834408	GOOD
15DP_A02_044	2.242152466	0.075422027	0.1969	0.004341599	1.04	2253.040452	78.7	2377.44276	80	2607.52594	102	2800.67393	62	8.278211147	GOOD
15DP_A02_088	2.259887006	0.030165653	0.19573	0.003799524	1.04	2238.164161	32.3	2361.82051	31.5	2600.49363	63	2790.92021	54	9.177992826	GOOD
15DP_A02_030	1.953888238	0.029803488	0.19839	0.003886632	1.07	2603.357396	46.4	2664.30711	40.6	2732.643	65	2812.99945	55	2.500725153	GOOD
15DP_A02_099	2.191540653	0.023095246	0.1995	0.003837968	1.05	2299.188258	27.4	2423.1984	25.5	2643.47923	57	2822.11269	54	8.332988933	GOOD
15DP_A02_050	1.948937829	0.0167581	0.19958	0.003818868	1.07	2606.556577	28.5	2669.84801	23	2752.41275	57	2822.76256	54	2.999722429	GOOD
15DP_A02_059	2.133105802	0.026879652	0.2	0.003863959	1.05	2363.277103	33.3	2478.29436	31.2	2671.64495	61	2826.19878	55	7.237136404	GOOD
15DP_A02_071	1.96155355	0.015824168	0.20005	0.003838191	1.07	2586.234628	26.8	2655.77334	21.4	2750.38537	58	2826.60674	54	3.439955139	GOOD
15DP_A02_053	1.934235977	0.016506904	0.20047	0.00383497	1.08	2625.624291	28.7	2686.44219	22.9	2762.48942	58	2830.02903	54	2.752851334	GOOD
15DP_A02_017	1.948178453	0.032663645	0.20053	0.003845893	1.07	2604.342418	50.7	2670.70004	44.8	2731.26528	69	2830.51726	54	2.217479372	GOOD
15DP_A02_014	2.087246921	0.038796168	0.2007	0.003970571	1.06	2415.856763	49.2	2523.34221	46.9	2668.71666	71	2831.89966	56	5.447354246	GOOD
15DP_A02_058	2.008032129	0.02100577	0.20106	0.003849585	1.07	2517.121129	31.4	2605.19284	27.3	2729.19518	59	2834.82268	54	4.543549566	GOOD
15DP_A02_060	1.934610176	0.019126969	0.20119	0.003917792	1.08	2622.47777	32.4	2686.01723	26.6	2765.15972	63	2835.87673	55	2.86213091	GOOD
15DP_A02_010	1.850823617	0.019902578	0.20177	0.003937404	1.09	2757.616644	38.5	2784.70159	29.9	2796.02082	61	2840.56997	55	0.404833499	GOOD
15DP_A02_013	2.166377816	0.018354583	0.20255	0.003876533	1.05	2317.967685	23.4	2446.61661	20.7	2638.95971	55	2846.87854	54	7.288959553	GOOD
15DP_A02_082	1.716148962	0.01682245	0.28873	0.005531746	1.11	2645.296942	37.4	2959.75412	29	3233.68921	71	3410.78203	65	8.471287121	GOOD
15DP_A02_029	1.438848921	0.022791295	0.361	0.007176473	1.15	2886.057019	70.8	3401.6586	53.9	3606.26224	97	3754.07015	72	5.673565099	GOOD
15DP_A02_062	39.3081761	0.680312079	0.238	0.004735866	0.85	130.8969516	2.4	161.945317	2.8	610.277683	15	3106.64703	62	73.46366719	BAD
15DP_A02_105	35.13703443	0.102624669	0.212	0.004190259	0.85	151.239889	4.4	180.902587	5.21	615.829273	21	2914.77818	58	70.2455539	BAD
15DP_A02_055	34.50655625	0.357875738	0.1911	0.003843795	0.85	157.5556408	1.79	184.161134	1.91	575.220957	12	2902.62682	55	67.98427947	BAD
15DP_A02_033	26.92514809	0.283247364	0.1884	0.003718337	0.85	202.3061555	2.31	235.080702	2.47	681.741162	15	2728.24692	54	65.51760189	BAD
15DP_A02_063	24.72799209	0.391654989	0.23307	0.004488611	0.85	208.4669106	3.5	255.559496	4.05	841.297593	21	3073.2522	59	69.62317524	BAD
15DP_A02_121	23.67984485	0.331172064	0.2136	0.00423399	0.85	222.8587671	3.32	266.640535	3.73	830.599866	21	2933.06126	58	67.89783552	BAD
15DP_A02_114	23.3426704	0.137016492	0.16327	0.003117161	0.85	239.8518637	1.66	270.412408	1.59	694.373996	14	2489.81135	48	61.05666263	BAD
15DP_A02_056	21.4178625	0.43599874	0.17364	0.003358492	0.86	258.0073231	5.29	294.167704	5.99	757.63057	22	2593.04345	50	61.17587444	BAD
15DP_A02_020	20.04008016	0.213226989	0.22879	0.0043931	0.86	257.912616	3.1	313.907365	3.34	940.891664	21	3043.60498	58	66.63272667	BAD
15DP_A02_067	19.70831691	0.233383231	0.2059	0.004065643	0.86	269.6073443	3.45	319.062921	3.78	900.295529	19	2873.54854	57	64.56020158	BAD
15DP_A02_115	18.4706317	0.21184366	0.15857	0.003031237	0.86	303.7010286	3.6	339.888629	3.9	802.891426	18	2440.47173	47	57.66692503	BAD
15DP_A02_104	17.75883502	0.14550652	0.17733	0.00388016	0.86	308.9564444	2.81	353.145244	2.89	882.570185	18	2628.05897	50	59.98672398	BAD
15DP_A02_026	17.2621302	0.247567191	0.19976	0.003863096	0.86	309.4396047	4.62	363.024146	5.21	954.467575	23	2824.23892	55	61.96579589	BAD
15DP_A02_074	15.57632399	0.119291548	0.17615	0.00387097	0.86	351.9157715	3.03	401.117099	3.07	953.673997	20	2616.95425	50	57.3980954	BAD
15DP_A02_003	15.31393568	0.398795711	0.1624	0.003245029	0.86	363.5075926	9.39	407.776926	10.6	931.603942	30	2480.80458	50	57.29851004	BAD
15DP_A02_007	14.36781609	0.330419405	0.19191	0.003689295	0.86	373.9997038	8.61	433.744976	9.97	1055.56165	37	2758.60195	53	58.98068183	BAD
15DP_A02_035	14.23892923	0.13816138	0.21805	0.004219582	0.87	365.7251316	4.02	437.540826	4.25	1145.19731	25	2966.3495	57	61.79341135	BAD
15DP_A02_006	14.12429379	0.199695264	0.20153	0.003890819	0.87	376.0211126	5.54	440.973243	6.23	1110.08259	27	2838.62982	55	60.27563648	BAD
15DP_A02_068	14.08450704	0.357182931	0.19644	0.003843461	0.87	379.3428602	9.61	442.177166	11.2	1087.37229	34	2796.8471	55	59.3252532	BAD
15DP_A02_022	13														

15DP_A02_039	5.151983514	0.050536655	0.19263	0.003697099	0.92	1010.576571	10.5	1143.54625	11.2	1838.26766	39	2764.74962	53	37.79217934	BAD
15DP_A02_072	5.015045135	0.135850634	0.19094	0.003723319	0.92	1039.045563	27.4	1172.09526	31.8	1857.51799	61	2750.27757	54	36.89992438	BAD
15DP_A02_076	4.840271055	0.068010673	0.18297	0.003551866	0.93	1084.814745	15.3	1210.67737	17	1854.74349	44	2679.97896	52	34.72534761	BAD
15DP_A02_091	4.828585225	0.065353937	0.1825	0.003610441	0.93	1087.911294	14.9	1213.34813	16.4	1848.84294	43	2675.72346	53	34.3725691	BAD
15DP_A02_049	4.582951421	0.056783209	0.11833	0.002333248	0.93	1226.862259	14.9	1272.35578	15.8	1540.21845	38	1931.16061	38	17.39121295	BAD
15DP_A02_107	4.528985507	0.075947277	0.15862	0.003034358	0.93	1188.088591	19.5	1286.09967	21.6	1803.97632	50	2441.00559	47	28.70750838	BAD
15DP_A02_016	4.502476362	0.075061436	0.271	0.005267642	0.93	1046.115616	18.3	1292.96064	21.6	2241.12831	60	3311.82317	64	42.30760321	BAD
15DP_A02_112	4.278990158	0.049510247	0.18989	0.003686761	0.94	1211.150203	14.4	1353.86047	15.7	2009.65328	43	2741.21158	53	32.63213722	BAD
15DP_A02_001	4.217629692	0.04100005	0.11165	0.002154394	0.94	1337.789551	12.8	1371.60193	13.3	1603.05907	34	1826.44939	35	14.43846593	BAD
15DP_A02_046	3.92003136	0.052305295	0.19517	0.003806163	0.95	1309.174363	17.8	1464.72236	19.5	2094.02008	48	2786.22803	54	30.05213374	BAD
15DP_A02_098	3.913894325	0.075101729	0.19611	0.003782444	0.95	1309.720076	24.8	1466.77651	28.1	2097.37161	58	2794.09541	54	30.06596921	BAD
15DP_A02_120	3.800836184	0.057835323	0.19154	0.003715472	0.95	1354.109783	20.6	1505.68134	22.9	2121.5334	54	2755.43239	53	29.02862912	BAD
15DP_A02_075	3.639010189	0.039793693	0.18349	0.003523664	0.96	1424.810401	16.1	1565.11907	17.1	2105.06394	48	2684.67248	52	25.64980837	BAD
15DP_A02_085	3.558718861	0.070956737	0.167	0.00393781	0.96	1482.949057	29	1596.39524	31.8	2051.29966	64	2527.80123	51	22.17640004	BAD
15DP_A02_032	3.50877193	0.123134772	0.19883	0.003899624	0.96	1449.72905	49.3	1616.49318	56.7	2196.60185	95	2816.61889	55	26.40936825	BAD
15DP_A02_018	3.497726478	0.079552304	0.19843	0.003849798	0.96	1454.795071	32.5	1621.00659	36.9	2183.68182	62	2813.32887	55	25.76727169	BAD
15DP_A02_077	3.465003465	0.036085249	0.18254	0.003526678	0.97	1495.011794	16.2	1634.5279	17	2143.04419	48	2676.08613	52	23.72868867	BAD
15DP_A02_065	3.151591554	0.059628448	0.16965	0.003271486	0.98	1661.971874	31	1776.5283	33.6	2153.69195	54	2554.19512	49	17.5124234	BAD
15DP_A02_122	3.049710278	0.036324024	0.1881	0.003702272	0.98	1679.87683	20.7	1828.19342	21.8	2303.93322	57	2725.62229	54	20.64902709	BAD
15DP_A02_043	3.019323671	0.031964107	0.19514	0.003799019	0.99	1682.444365	18.9	1844.19369	19.5	2322.45389	51	2785.97623	54	20.59288223	BAD
15DP_A02_080	2.960331557	0.050863082	0.2003	0.003901279	0.99	1704.567674	29.5	1876.07559	32.2	2368.01972	59	2828.64481	55	20.77449495	BAD
15DP_A02_111	2.906131938	0.059991899	0.18901	0.003644355	0.99	1758.361358	36.1	1906.36191	39.4	2354.12374	64	2733.56884	53	19.02031843	BAD
15DP_A02_040	2.849002849	0.105533984	0.1921	0.003876179	1	1786.184335	64.9	1939.3702	71.8	2361.09551	96	2760.22682	56	17.86142515	BAD
15DP_A02_119	2.841716397	0.044450729	0.1863	0.003679904	1	1802.573865	28.6	1943.66319	30.4	2361.09551	64	2709.77248	54	17.67960299	BAD
15DP_A02_089	2.808199944	0.029232072	0.1898	0.003802284	1	1816.307104	20.2	1963.65946	20.4	2373.91742	57	2740.43181	55	17.28189691	BAD
15DP_A02_106	2.787068004	0.062166941	0.19642	0.0037833	1	1815.614287	40.3	1976.48152	44.1	2415.21056	73	2796.68048	54	18.16525007	BAD
15DP_A02_083	2.756339581	0.042581128	0.28222	0.00540647	1.01	1650.982625	27.5	1995.43041	30.8	2756.45543	69	3375.25826	65	27.60882721	BAD
15DP_A02_038	2.564760195	0.026361854	0.20257	0.003885658	1.01	1955.366628	21.9	2122.36275	21.8	2505.20593	55	2847.01809	55	15.28190484	BAD
15DP_A02_057	2.564102564	0.02241237	0.18681	0.003603131	1.01	1992.812739	19.3	2122.82653	18.6	2430.15667	52	2714.28114	52	12.64651529	BAD
15DP_A02_081	2.44977952	0.05283518	0.19574	0.003823519	1.02	2063.140747	45.4	2206.68494	47.6	2531.55892	66	2791.00386	55	12.83296165	BAD
15DP_A02_070	2.418964683	0.046251252	0.19757	0.003848452	1.03	2084.790107	41.1	2230.44547	42.6	2542.40981	69	2806.22948	55	12.27041913	BAD
15DP_A02_015	2.369668246	0.061786754	0.2839	0.005628915	1.03	1908.180247	51.1	2269.55056	59.2	2876.79722	93	3384.51341	67	21.10842768	BAD
15DP_A02_008	1.87722921	0.018363107	0.36011	0.006903039	1.08	2159.933716	32.2	2752.81561	26.9	3354.77734	73	3750.3209	72	17.9434183	BAD
15DP_A02_009	1.620745543	0.036789686	0.3614	0.007031797	1.12	2512.31581	69	3097.96725	70.3	3504.02595	102	3755.75187	73	11.58834739	BAD

Appendix C: (U-Th)/He Apatite Data

sample name	notes1	notes2	sample/run type	He date	pmol He	1s ± pmol He	% 1s ± He	U+Th date	(238/233)m	(238/233)m 1s ±	(232/229)m	(232/229)m 1s ±	(152/147)m	(152/147)m 1s ±	(44/42)m
17A421_16BC_VT1_Ap1	0	0	ap	3/2/2017	0.052141975	0.000783157	1.501970999	3/14/2017	0.1299	0.0007	0.1494	0.001	0.4167	0.003	0.2549
17A422_16BC_VT1_Ap2	0	0	ap	3/2/2017	0.009403052	0.000158676	1.687492628	3/14/2017	0.1245	0.0005	0.0327	0.0003	0.2052	0.0006	0.1187
17A423_16BC_VT1_Ap3	0	0	ap	3/3/2017	0.034569023	0.000418143	1.209587599	3/14/2017	0.5599	0.0031	0.0245	0.0007	0.3494	0.0022	0.2457
17A424_16BC_VT1_Ap4	0	0	ap	3/3/2017	0.007830846	0.00011733	1.498310645	3/14/2017	0.173	0.0009	0.0222	0.0002	0.205	0.0015	0.1179
17A425_16BC_VT1_Ap5	0	0	ap	3/3/2017	0.137400379	0.001618728	1.178110313	3/14/2017	1.0673	0.0023	0.2538	0.0013	0.7065	0.0029	0.5132
17A426_16BC_VT1_Ap6	0	0	ap	3/3/2017	0.074046301	0.000865735	1.169181114	3/14/2017	1.277	0.0038	0.0443	0.0002	0.8468	0.0038	0.5431
17A427_16BC_VT2_Ap1	0	0	ap	3/3/2017	0.034060283	0.00040392	1.185898579	3/14/2017	0.399	0.001	0.0041	0.0001	0.4351	0.0015	0.2412
17A428_16BC_VT2_Ap2	0	0	ap	3/3/2017	0.005403044	0.000107033	1.980977447	3/14/2017	0.087	0.0003	0.0032	0.0001	0.3092	0.0017	0.182
17A429_16BC_VT2_Ap3	0	0	ap	3/3/2017	0.004307755	7.63462E-05	1.772295664	3/14/2017	0.0168	0.0001	0.0023	0.0001	0.083	0.0004	0.0573
17A430_16BC_VT2_Ap4	0	0	ap	3/3/2017	0.012083585	0.000203667	1.685482936	3/14/2017	0.1006	0.0004	0.0223	0.0002	0.3608	0.0014	0.2278
17A431_16BC_VT2_Ap5	0	0	ap	3/3/2017	0.001746081	5.80003E-05	3.321738607	3/14/2017	0.032	0.0002	0.0051	0.0001	0.1963	0.0014	0.1303
17A432_16BC_VT2_Ap6	0	0	ap	3/3/2017	0.009851693	0.000150138	1.523981008	3/14/2017	0.1378	0.0007	0.0174	0.0002	0.533	0.0019	0.3856
17A434_16BC_VT3_Ap1	0	0	ap	3/3/2017	0.005231018	8.84234E-05	1.69036744	3/14/2017	0.1408	0.0009	0.1165	0.001	0.3234	0.0018	0.1718
17A435_16BC_VT3_Ap2	0	0	ap	3/3/2017	0.016901087	0.000215525	1.275214614	3/14/2017	0.3001	0.0012	0.1502	0.0006	0.4015	0.0022	0.1789
17A436_16BC_VT3_Ap3	0	0	ap	3/3/2017	0.002445703	4.66241E-05	1.906368921	3/14/2017	0.0824	0.0005	0.0356	0.0003	0.2648	0.0028	0.125
17A437_16BC_VT3_Ap4	0	0	ap	3/7/2017	0.003031309	6.0648E-05	2.000719391	3/14/2017	0.0483	0.0002	0.0238	0.0004	0.1421	0.0007	0.0794
17A438_16BC_VT3_Ap5	0	0	ap	3/7/2017	0.027922742	0.000286919	1.027546419	3/15/2017	0.3128	0.0013	0.0738	0.0003	0.0684	0.0005	0.1993
17A439_16BC_VT3_Ap6	0	0	ap	3/7/2017	0.019087752	0.000196002	1.026847942	3/15/2017	0.3197	0.0011	0.0399	0.0003	0.1669	0.0008	0.3513
17A440_16BC_VT4_Ap1	0	0	ap	3/7/2017	0.399219142	0.003381302	0.846979022	3/14/2017	2.4469	0.0035	0.8808	0.0012	0.7296	0.0027	0.5706
17A441_16BC_VT4_Ap2	Likes a blk	0	ap	3/8/2017	4.93773E-05	9.01524E-06	18.25787199	3/14/2017	0.0043	0.0012	0.002	0.0005	0.0038	0.0002	0.0139
17A442_16BC_VT4_Ap3	0	0	ap	3/8/2017	0.318114188	0.001868932	0.587503415	3/14/2017	2.9304	0.0062	1.0059	0.0039	0.9634	0.0026	0.861
17A443_16BC_VT4_Ap4	0	0	ap	3/8/2017	0.153367148	0.00088445	0.576687874	3/14/2017	1.2513	0.0041	0.2428	0.0014	0.504	0.0026	0.3873
17A444_16BC_VT4_Ap5	0	0	ap	3/8/2017	0.256140671	0.001429618	0.558137652	3/14/2017	2.6188	0.0046	0.2552	0.0014	0.6145	0.0038	0.3995
17A445_16BC_VT4_Ap6	0	0	ap	3/8/2017	0.247931027	0.001392143	0.561504158	3/14/2017	1.0524	0.0031	0.1939	0.0011	0.4822	0.0024	0.3739
17A446_16BC_VT5_Ap1	0	0	ap	3/8/2017	0.161682667	0.000957339	0.59210961	3/15/2017	1.1607	0.0025	0.4109	0.0013	0.2018	0.0013	0.2727
17A447_16BC_VT5_Ap2	0	0	ap	3/8/2017	0.007679637	8.36154E-05	1.088793064	3/15/2017	0.0958	0.0006	0.0289	0.0006	0.0379	0.0004	0.1703
17A448_16BC_VT5_Ap3	0	0	ap	3/8/2017	0.043479422	0.000357183	0.821500072	3/15/2017	0.5019	0.0007	0.1044	0.0005	0.1356	0.0009	0.2819
17A449_16BC_VT5_Ap4	0	0	ap	3/8/2017	0.136149662	0.000833371	0.612099297	3/15/2017	1.0217	0.0029	0.0307	0.0003	0.1356	0.0011	0.2918
17A420_DG_Dur_1	0	0	ap	3/2/2017	0.102706023	0.001514817	1.474905463	3/14/2017	0.2361	0.0007	3.2227	0.0085	0.5157	0.0023	0.6685
17A433_DG_Dur2	0	0	ap	3/3/2017	0.039310082	0.000467087	1.188210547	3/14/2017	0.0841	0.0002	1.5694	0.0044	0.2332	0.0012	0.2723
17A450_SC17_Dur_Ap7	0	0	ap	3/8/2017	0.189809745	0.001100048	0.579552985	3/15/2017	0.426	0.0013	6.8604	0.0163	0.6442	0.0018	0.7897
Nblk								3/14/2017	0.0028	0.0001	0.0011	0.0001	0.0037	0.0002	0.0137

(44/42)m 1s ±	ng U	1s ± ng U	% 1s ± ng U	ng Th	1s ± ng Th	% 1s ± ng Th	ng Sm	1s ± ng Sm	% 1s ± ng Sm	ng Ca	1s ± ng Ca	% 1s ± ng Ca	Th/U	raw date (Ma)	1s ± date (Ma)
0.0003	0.062349541	0.000905184	1.451789022	0.081585751	0.001185095	1.452575846	1.41204917	0.021284295	1.507333851	1716.017698	26.54351458	1.546808906	1.342379923	115.0388756	2.158679644
0.0003	0.059703551	0.000861283	1.442598654	0.017369988	0.000259477	1.493821595	0.596585137	0.00867772	1.45456527	713.7128445	11.08317995	1.552890639	0.298465231	26.98873938	0.574179555
0.0023	0.273048741	0.003962944	1.451368634	0.012857826	0.00025305	1.96806175	1.126493138	0.016776446	1.48926303	1645.4274	26.62211558	1.617945318	0.048308302	23.08939001	0.423613385
0.0005	0.083468461	0.001210087	1.449753779	0.01159222	0.000174758	1.507542789	0.595917365	0.008907784	1.494801884	708.0852497	11.06831313	1.563132848	0.14247498	16.70224555	0.336230065
0.0045	0.521673797	0.007476162	1.433110473	0.139033272	0.002000799	1.439079413	3.049000441	0.045080495	1.478533557	3893.481546	62.96850744	1.617280234	0.273409822	45.51403343	0.798671345
0.0065	0.624426407	0.008967084	1.436051316	0.023753046	0.000342429	1.441619608	4.204980582	0.062929646	1.49655022	4172.633193	70.07421792	1.679376419	0.039024059	21.60816059	0.38803731
0.0023	0.19420804	0.002785681	1.434379963	0.001632449	4.63707E-05	2.840560649	1.495079185	0.021846883	1.46125254	1611.058118	26.10822914	1.620564079	0.008623166	32.11176558	0.582275933
0.0022	0.041328621	0.000595469	1.440816277	0.001137211	4.32841E-05	3.806161206	0.968351907	0.014308758	1.477640328	1168.378805	19.45113749	1.664797189	0.028228299	23.41142035	0.561133247
0.0006	0.006930751	0.000106594	1.537980496	0.000641974	4.11794E-05	6.414502109	0.217830705	0.003193541	1.466065659	290.0601087	4.863199257	1.676617746	0.095023637	107.8472339	2.461520044
0.0019	0.047992596	0.000692558	1.443052393	0.011647246	0.000175494	1.50674471	1.172964514	0.017164025	1.463303008	1509.325438	24.19820663	1.603246458	0.248967935	42.84721723	0.910243026
0.0009	0.014378723	0.000212722	1.479420253	0.002182712	5.07325E-05	2.324285458	0.567032049	0.008460257	1.492024416	795.6400229	12.63413445	1.58792093	0.155729385	20.7713365	0.743580342
0.0018	0.066220526	0.000959744	1.449314279	0.008950955	0.000139976	1.563814513	1.977905629	0.028970199	1.464690669	2768.286791	43.31398144	1.564649356	0.138666363	25.80504986	0.519265071
0.0017	0.067690521	0.000988291	1.460013291	0.063482079	0.000935204	1.473177604	1.023218722	0.015133134	1.478973515	1093.840552	17.79605906	1.626933562	0.962094373	11.55329175	0.2372321
0.0005	0.145747224	0.002100725	1.441348301	0.082025962	0.001174829	1.432264985	1.345125526	0.019926873	1.481413672	1145.672204	17.78864561	1.552681957	0.577358325	18.78119017	0.332338495
0.0004	0.039074629	0.000570277	1.459456602	0.018965752	0.000281116	1.482229214	0.803411629	0.012470002	1.552131074	758.1316838	11.79651878	1.555998652	0.4979315	10.18617826	0.231904204
0.0009	0.022365693	0.000324422	1.450536075	0.012472642	0.000205138	1.64470565	0.393971495	0.005781416	1.467470755	440.6418329	7.367130587	1.671909029	0.572098075	21.77588661	0.511721158
0.0014	0.14932101	0.002148095	1.438575124	0.039438076	0.000569463	1.443943247	0.177468878	0.002605967	1.468407984	1290.837084	20.04916961	1.553191325	0.270950019	32.53990698	0.541622635
0.0018	0.152643535	0.002190001	1.434715763	0.020992483	0.000312627	1.489233096	0.475707318	0.006868056	1.443756673	2476.93164	37.98086092	1.533383494	0.141084655	22.36186254	0.376963141
0.0065	1.197675231	0.017141995	1.431272368	0.484048556	0.006881749	1.421706265	3.21818413	0.047428448	1.473764281	4434.931851	74.03464112	1.669352396	0.414614277	56.0397883	0.854407784
0.0004	0.000805775	0.000265222	32.91509431	0.000476895	0.000127249	26.68288549	0.000116737	0.000237702	203.6219043	0.381194804	1.267550087	332.5202946	0.607160684	9.967872754	3.33075737
0.0042	1.434589331	0.020557252	1.432971122	0.552886534	0.00791159	1.430960826	5.466259278	0.080377568	1.470430946	7577.425828	119.2868732	1.574240065	0.395369176	37.44656119	0.52343632
0.003	0.611833455	0.008794293	1.437367143	0.132980373	0.001920254	1.444013046	1.82718695	0.027086888	1.482436595	2782.612325	44.46458579	1.597943968	0.222971172	43.94256501	0.632393757
0.0093	1.281905911	0.018356884	1.431999334	0.139803641	0.00201566	1.441779309	2.441480273	0.036804687	1.507474264	2885.92501	56.92231725	1.972411516	0.111881099	35.97223173	0.524013583
0.0063	0.514372825	0.007386068	1.435936682	0.106072482	0.001531087	1.443435064	1.718307555	0.025412545	1.478928791	2670.156941	47.50308932	1.779037351	0.21155296	84.36367148	1.214435081
0.0015	0.557606352	0.007970437	1.429402085	0.22286018	0.003193339	1.432889127	0.590284019	0.008625475	1.461241437	1848.342575	28.39979864	1.53650081	0.410014444	48.91354	0.684147482
0.0007	0.04483001	0.000653141	1.456928122	0.015007187	0.000264443	1.762108777	0.091941459	0.001399377	1.522030781	1077.955239	16.45235172	1.526255556	0.343419422	29.32747379	0.499022971
0.0024	0.240377453	0.003431563	1.427572774	0.05608808	0.000810572	1.445176299	0.377074882	0.005509745	1.461180574	1920.182413	30.19366083	1.57243711	0.239370834	31.68130139	0.4888936
0.0015	0.490674329	0.007025521	1.431809385	0.015986599	0.000245178	1.533647271	0.377074882	0.005578693	1.479465648	1997.991868	30.63381931	1.53323043	0.033423901	50.84858032	0.76460934
0.0039	0.114387343	0.001643053	1.436393858	1.772710906	0.025266013	1.425275435	1.887165054	0.027816637	1.473990697	5414.534409	85.60512137	1.581024607	15.89843348	35.41460943	0.664176677
0.0034	0.039907626	0.000573221	1.436370544	0.862960078	0.012305099	1.425917485	0.691772686	0.010179338	1.471486024	1850.728528	30.95858328	1.672778196	22.18345569	29.67255726	0.503851505
0.0078	0.20382968	0.002920512	1.432819924	3.732147826	0.053354672	1.429596952	2.650607597	0.038084054	1.436804688	6727.535207	109.1107842	1.621853782	18.78390172	32.19026586	0.425761559

1s ± date %	morph comments	Ft 238U	Ft 235U	Ft 232Th	Ft 147Sm	Rs (um)	corr date (Ma)	1s ± date (Ma)	comment	1s ± date %	ppm eU (morph)	ppm eU w/ Sm (morph)	ppm U (morph)
1.876478394	subhedral	0.755	0.722	0.722	0.921	58.63	152.97	2.88		1.88	16.19	17.49	12.38
2.12747823	subhedral	0.671	0.627	0.627	0.893	42.37	40.30	0.86		2.13	29.80	31.10	27.89
1.834666852	subhedral; rounded edges	0.735	0.698	0.698	0.915	53.69	31.45	0.58		1.84	58.24	59.35	57.60
2.013082997	subhedral	0.660	0.616	0.616	0.889	40.92	25.32	0.51		2.02	45.94	47.43	44.49
1.754780415	subhedral, possible inclusion in core	0.810	0.784	0.784	0.939	76.93	56.24	0.99		1.76	46.16	47.35	43.44
1.795790567	subhedral	0.814	0.788	0.788	0.941	78.73	26.53	0.48		1.80	45.76	47.19	45.35
1.813279098	subhedral	0.762	0.729	0.729	0.924	60.34	42.11	0.76		1.81	30.74	31.85	30.68
2.396835555	subhedral	0.760	0.727	0.727	0.923	59.95	30.65	0.73		2.40	9.35	10.37	9.29
2.282413703	subhedral	0.739	0.703	0.703	0.916	54.60	144.71	3.31	very little Ca; prob not ap	2.28	1.59	1.82	1.55
2.124392398	subhedral	0.784	0.754	0.754	0.931	67.04	54.50	1.16		2.13	6.32	7.01	5.98
3.579838698	poor subhedral	0.682	0.640	0.640	0.897	44.04	30.14	1.08		3.58	5.22	6.15	5.04
2.012261454	poor subhedral, irregular edge	0.783	0.753	0.753	0.931	66.67	32.82	0.66		2.01	7.71	8.76	7.48
2.053372368	subhedral, possible crack	0.689	0.647	0.647	0.899	45.10	16.90	0.35		2.06	27.98	29.59	22.93
1.769528404	subhedral-poor	0.738	0.702	0.702	0.916	54.36	25.58	0.45		1.77	40.89	42.44	36.12
2.276655662	subhedral, irregular edge	0.690	0.649	0.649	0.900	45.34	14.77	0.34		2.28	16.33	17.73	14.65
2.349944078	subhedral, irregular edge	0.682	0.640	0.640	0.897	44.04	32.01	0.75		2.35	12.22	13.11	10.80
1.664487347	subhedral	0.705	0.665	0.665	0.904	47.79	46.35	0.77		1.67	44.83	45.05	42.21
1.685741251	subhedral, irregular edge	0.777	0.746	0.746	0.929	64.72	28.83	0.49		1.69	21.39	21.69	20.72
1.524644918	subhedral	0.817	0.791	0.791	0.941	79.74	68.79	1.05		1.53	92.04	93.07	84.06
33.41492666	subhedral	0.729	0.692	0.692	0.913	52.40	13.79	4.63	no Ca; not ap	33.59	0.22	0.22	0.19
1.397822131	subhedral	0.843	0.820	0.820	0.950	93.68	44.53	0.62		1.40	68.56	69.67	62.87
1.439137103	subhedral	0.763	0.730	0.730	0.924	60.62	57.71	0.83		1.44	92.15	93.36	87.67
1.456716912	subhedral, possible crack	0.774	0.743	0.743	0.928	63.94	46.52	0.68		1.46	152.30	153.61	148.49
1.439523742	subhedral	0.771	0.739	0.739	0.927	62.83	109.54	1.58		1.45	74.65	75.75	71.20
1.39868732	subhedral	0.755	0.721	0.721	0.921	58.58	65.03	0.91	age-eU corr??	1.41	110.77	111.24	101.26
1.701554573	subhedral	0.693	0.652	0.652	0.901	45.81	42.51	0.73	age-eU corr??	1.71	17.15	17.30	15.90
1.543161356	subhedral	0.714	0.676	0.676	0.908	49.54	44.50	0.69	age-eU corr??	1.55	65.22	65.66	61.83
1.503698502	euهدral	0.732	0.696	0.696	0.914	53.14	69.49	1.05	age-eU corr??	1.51	98.96	99.31	98.21
1.875431321		0	1.000	1.000	1.000		35.41	0.66		1.88			
1.698038698		0	1.000	1.000	1.000		29.67	0.50		1.70			
1.322640704		0	1.000	1.000	1.000		32.19	0.43		1.32			

d ppm U (morph)	ppm Th (morph)	d ppm Th (morph)	ppm Sm (morph)	d ppm Sm (morph)	nmol 4He/g (morph)	d nmol 4He/g (morph)	mol Ca	d mol Ca	mass ap (g)	d mass ap (g)	ppm U (Ca)	d ppm U (Ca)	ppm Th (Ca)
0.18	16.20	0.24	280.45	4.23	10.36	0.16	4.28E-08	6.62E-10	4.32E-06	6.68E-08	14.44	0.31	18.90
0.40	8.12	0.12	278.72	4.05	4.39	0.07	1.78E-08	2.76E-10	1.80E-06	2.79E-08	33.25	0.70	9.67
0.84	2.71	0.05	237.64	3.54	7.29	0.09	4.10E-08	6.64E-10	4.14E-06	6.70E-08	65.95	1.43	3.11
0.65	6.18	0.09	317.65	4.75	4.17	0.06	1.77E-08	2.76E-10	1.78E-06	2.78E-08	46.85	1.00	6.51
0.62	11.58	0.17	253.92	3.75	11.44	0.13	9.71E-08	1.57E-09	9.80E-06	1.58E-07	53.25	1.15	14.19
0.65	1.73	0.02	305.40	4.57	5.38	0.06	1.04E-07	1.75E-09	1.05E-05	1.76E-07	59.48	1.31	2.26
0.44	0.26	0.01	236.16	3.45	5.38	0.06	4.02E-08	6.51E-10	4.05E-06	6.57E-08	47.91	1.04	0.40
0.13	0.26	0.01	217.67	3.22	1.21	0.02	2.91E-08	4.85E-10	2.94E-06	4.89E-08	14.06	0.31	0.39
0.02	0.14	0.01	48.83	0.72	0.97	0.02	7.24E-09	1.21E-10	7.30E-07	1.22E-08	9.50	0.22	0.88
0.09	1.45	0.02	146.15	2.14	1.51	0.03	3.77E-08	6.04E-10	3.80E-06	6.09E-08	12.64	0.27	3.07
0.07	0.76	0.02	198.69	2.96	0.61	0.02	1.98E-08	3.15E-10	2.00E-06	3.18E-08	7.18	0.16	1.09
0.11	1.01	0.02	223.29	3.27	1.11	0.02	6.91E-08	1.08E-09	6.97E-06	1.09E-07	9.51	0.20	1.29
0.33	21.50	0.32	346.60	5.13	1.77	0.03	2.73E-08	4.44E-10	2.75E-06	4.48E-08	24.59	0.54	23.07
0.52	20.33	0.29	333.33	4.94	4.19	0.05	2.86E-08	4.44E-10	2.88E-06	4.48E-08	50.56	1.07	28.45
0.21	7.11	0.11	301.31	4.68	0.92	0.02	1.89E-08	2.94E-10	1.91E-06	2.97E-08	20.48	0.44	9.94
0.16	6.03	0.10	190.31	2.79	1.46	0.03	1.10E-08	1.84E-10	1.11E-06	1.85E-08	20.17	0.45	11.25
0.61	11.15	0.16	50.16	0.74	7.89	0.08	3.22E-08	5.00E-10	3.25E-06	5.04E-08	45.97	0.97	12.14
0.30	2.85	0.04	64.58	0.93	2.59	0.03	6.18E-08	9.47E-10	6.23E-06	9.56E-08	24.49	0.51	3.37
1.20	33.97	0.48	225.87	3.33	28.02	0.24	1.11E-07	1.85E-09	1.12E-05	1.86E-07	107.33	2.36	43.38
0.06	0.11	0.03	0.03	0.06	0.01	0.00	9.51E-12	3.16E-11	9.59E-10	3.19E-09	840.10	2807.15	497.21
0.90	24.23	0.35	239.56	3.52	13.94	0.08	1.89E-07	2.98E-09	1.91E-05	3.00E-07	75.24	1.60	29.00
1.26	19.06	0.28	261.83	3.88	21.98	0.13	6.94E-08	1.11E-09	7.00E-06	1.12E-07	87.39	1.88	18.99
2.13	16.19	0.23	282.81	4.26	29.67	0.17	7.20E-08	1.42E-09	7.26E-06	1.43E-07	176.54	4.30	19.25
1.02	14.68	0.21	237.85	3.52	34.32	0.19	6.66E-08	1.19E-09	6.72E-06	1.20E-07	76.56	1.75	15.79
1.45	40.47	0.58	107.20	1.57	29.36	0.17	4.61E-08	7.08E-10	4.65E-06	7.15E-08	119.90	2.52	47.92
0.23	5.32	0.09	32.61	0.50	2.72	0.03	2.69E-08	4.10E-10	2.71E-06	4.14E-08	16.53	0.35	5.53
0.88	14.43	0.21	96.99	1.42	11.18	0.09	4.79E-08	7.53E-10	4.83E-06	7.60E-08	49.75	1.06	11.61
1.41	3.20	0.05	75.47	1.12	27.25	0.17	4.98E-08	7.64E-10	5.03E-06	7.71E-08	97.60	2.05	3.18
							1.35E-07	2.14E-09	1.36E-05	2.15E-07	8.40	0.18	130.12
							4.62E-08	7.72E-10	4.66E-06	7.79E-08	8.57	0.19	185.32
							1.68E-07	2.72E-09	1.69E-05	2.75E-07	12.04	0.26	220.48

d ppm Th (Ca)	ppm Sm (Ca)	d ppm Sm (Ca)	nmol 4He/g (Ca)	d nmol 4He/g (Ca)	ppm eU (Ca)	ppm eU w/ Sm (Ca)	eU (morph)/eU (Ca)
0.40	327.03	7.06	12.08	0.26	18.88	20.40	0.86
0.21	332.21	7.07	5.24	0.12	35.52	37.07	0.84
0.08	272.09	5.98	8.35	0.17	66.68	67.96	0.87
0.14	334.48	7.23	4.40	0.10	48.38	49.94	0.95
0.31	311.23	6.82	14.03	0.28	56.59	58.03	0.82
0.05	400.51	9.01	7.05	0.14	60.01	61.89	0.76
0.01	368.82	8.05	8.40	0.17	48.00	49.74	0.64
0.02	329.39	7.33	1.84	0.05	14.15	15.70	0.66
0.06	298.47	6.65	5.90	0.14	9.70	11.10	0.16
0.07	308.86	6.70	3.18	0.07	13.36	14.81	0.47
0.03	283.24	6.17	0.87	0.03	7.44	8.77	0.70
0.03	283.96	6.09	1.41	0.03	9.81	11.14	0.79
0.51	371.77	8.17	1.90	0.04	30.01	31.74	0.93
0.60	466.62	10.01	5.86	0.12	57.25	59.41	0.71
0.21	421.17	9.26	1.28	0.03	22.82	24.79	0.72
0.26	355.34	7.90	2.73	0.07	22.82	24.48	0.54
0.26	54.64	1.17	8.60	0.16	48.83	49.07	0.92
0.07	76.33	1.61	3.06	0.06	25.28	25.64	0.85
0.95	288.39	6.42	35.78	0.67	117.52	118.83	0.78
1658.64	121.71	474.56	51.48	171.44	956.94	957.02	0.00
0.62	286.70	6.18	16.68	0.28	82.06	83.38	0.84
0.41	260.97	5.69	21.90	0.37	91.85	93.06	1.00
0.47	336.23	8.35	35.27	0.72	181.06	182.62	0.84
0.36	255.76	5.92	36.90	0.69	80.27	81.46	0.93
1.01	126.92	2.69	34.77	0.57	131.16	131.71	0.84
0.13	33.90	0.73	2.83	0.05	17.83	17.98	0.96
0.25	78.05	1.68	9.00	0.16	52.48	52.84	1.24
0.07	75.01	1.60	27.08	0.45	98.35	98.70	1.01
2.77	138.52	2.99	7.54	0.16	38.97	39.50	
4.07	148.55	3.31	8.44	0.17	52.12	52.63	
4.77	156.59	3.39	11.21	0.19	63.85	64.37	

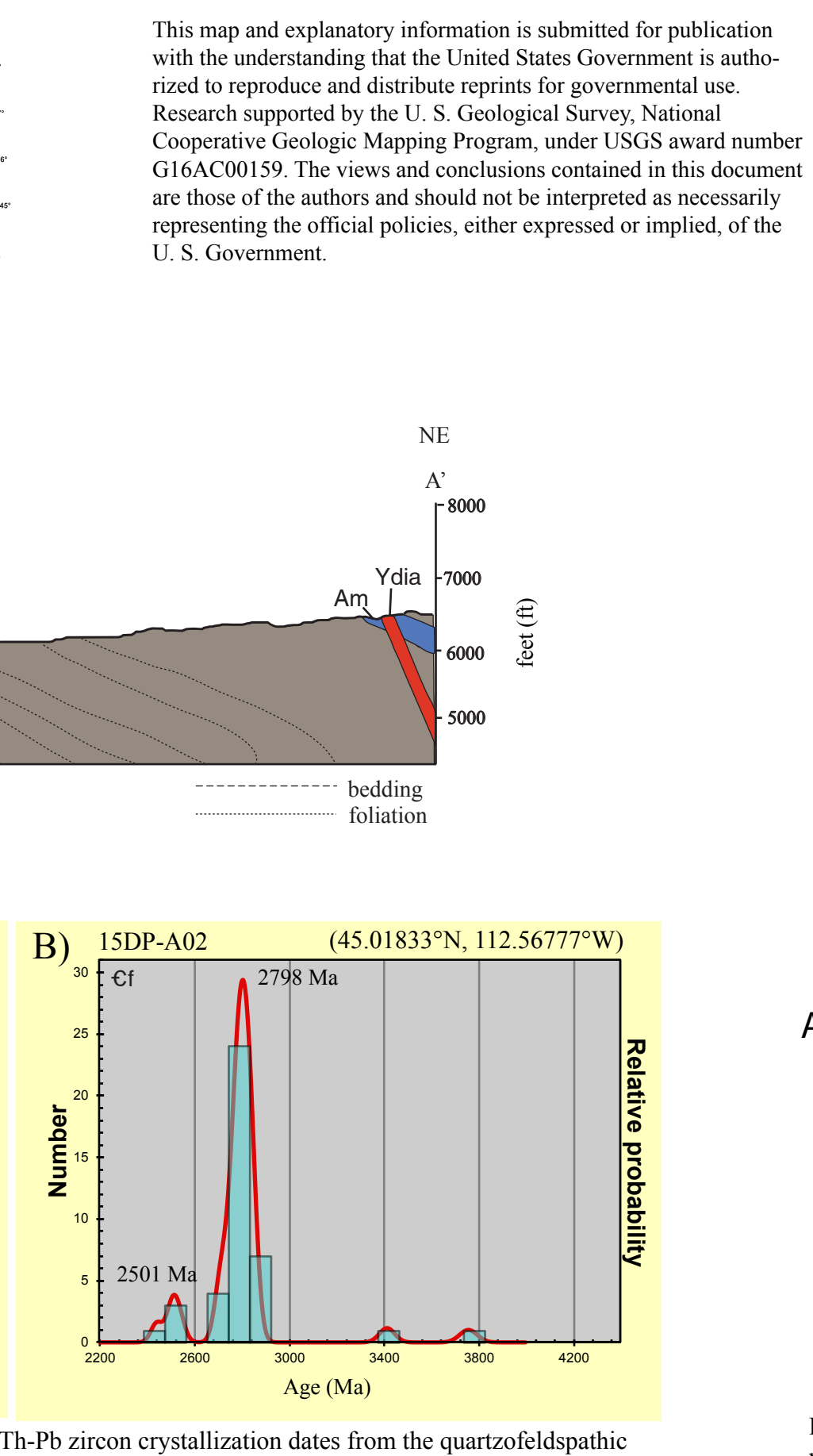
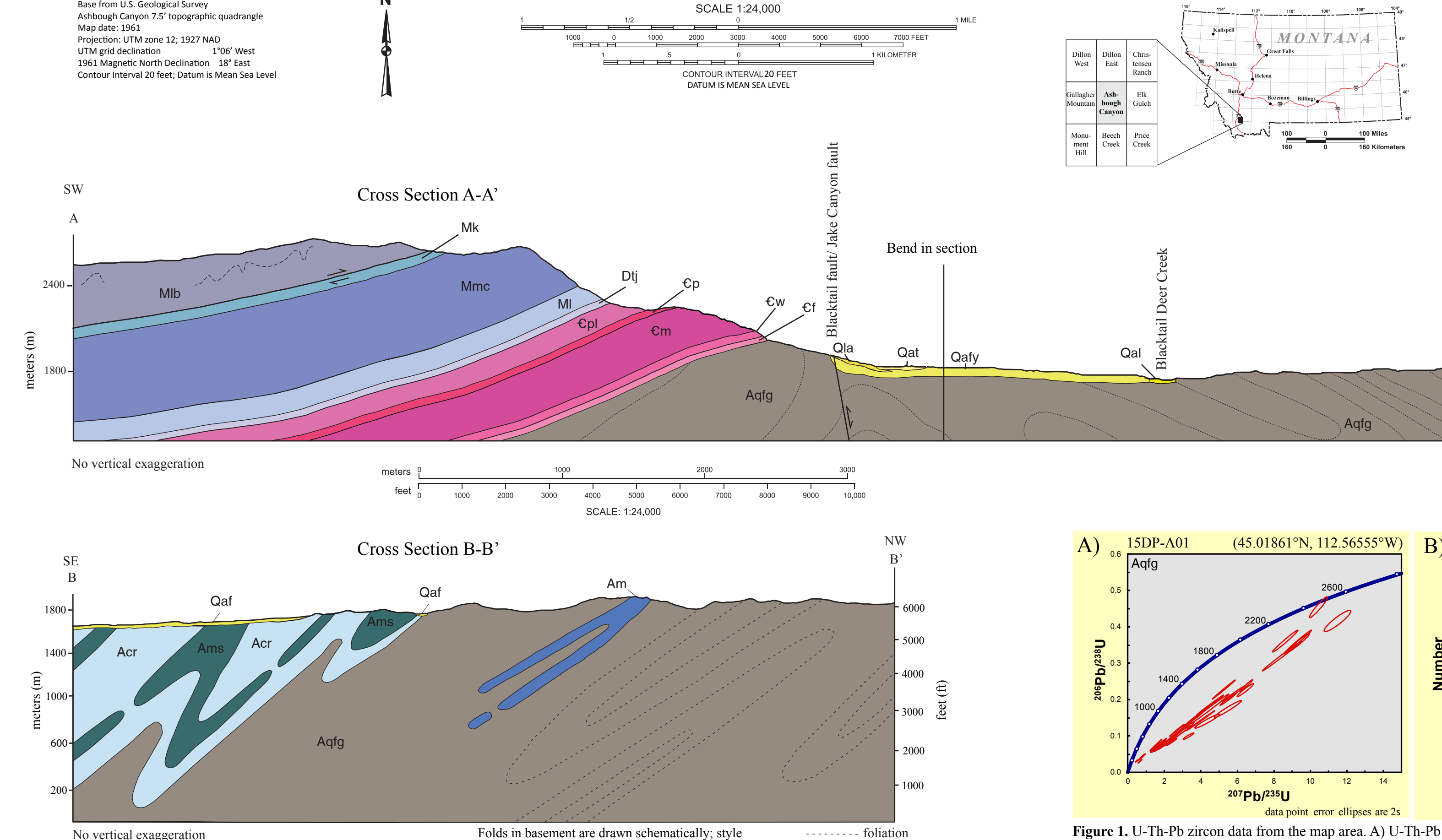
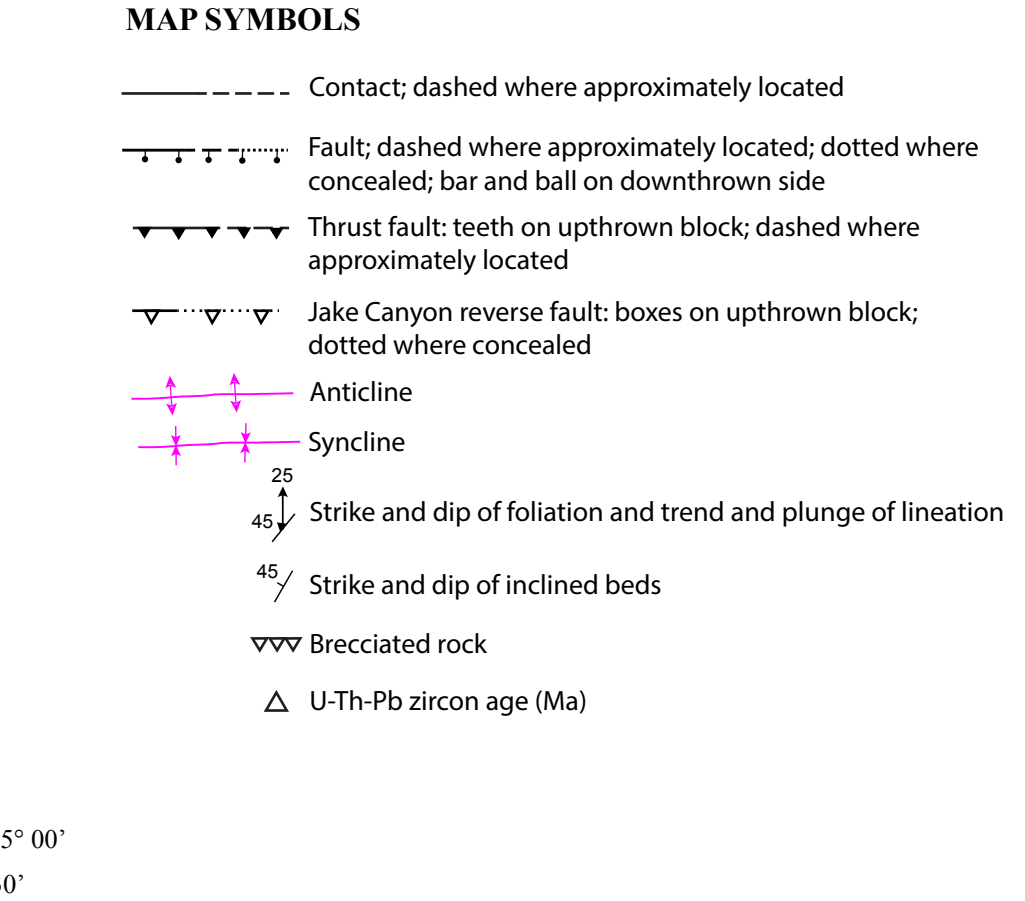
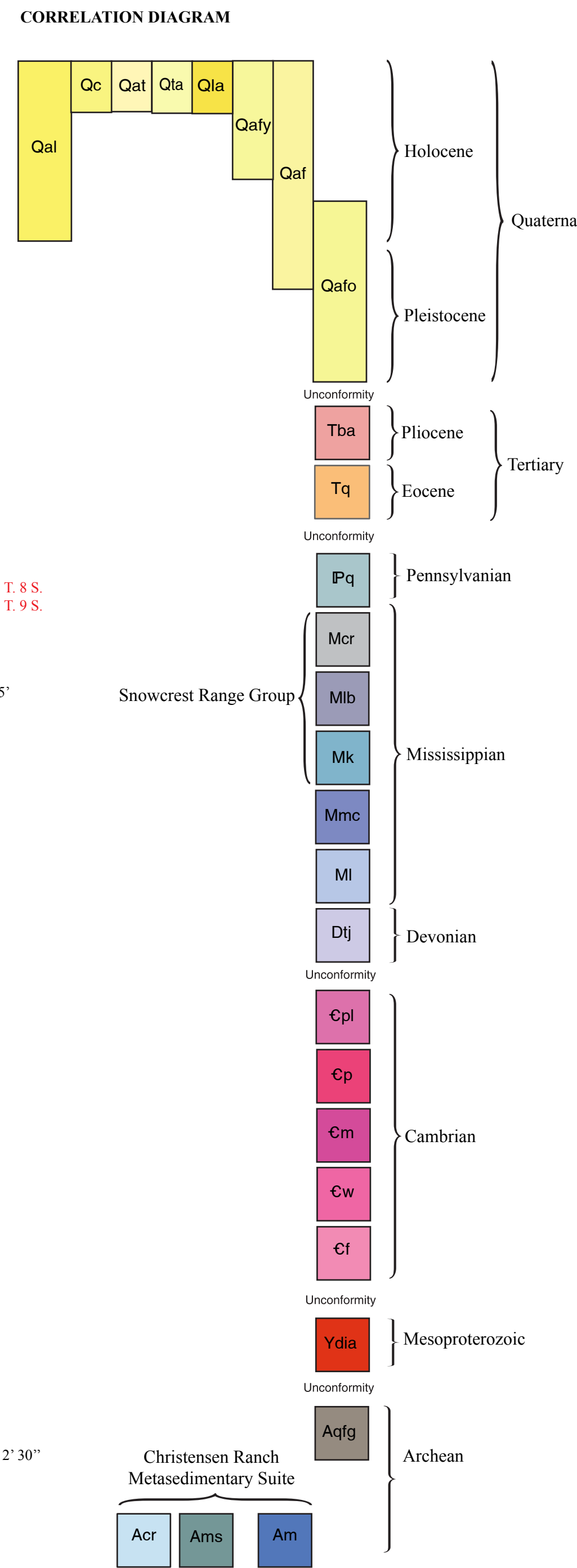
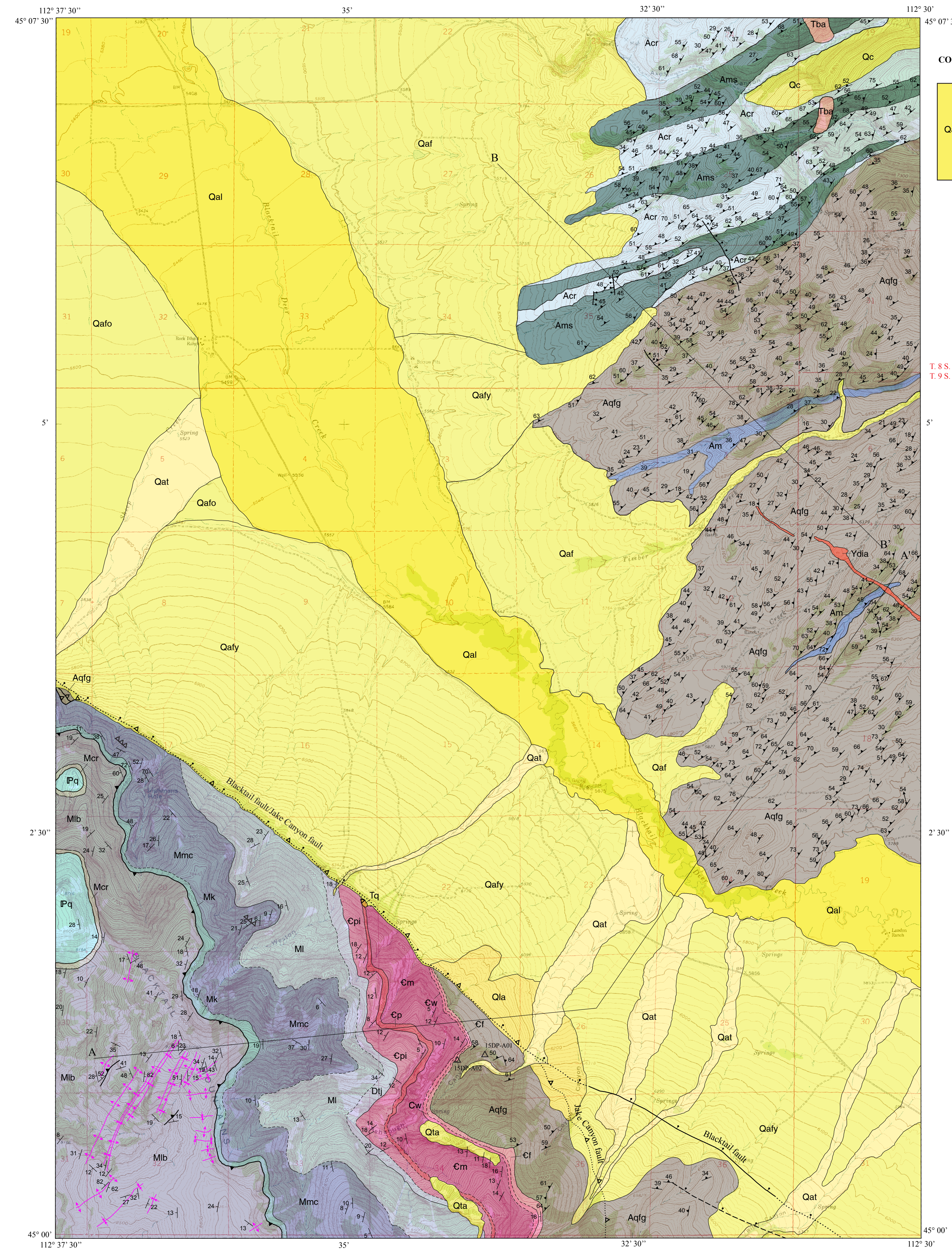


Figure 1. U-Th-Pb zircon data from the map area. A) U-Th-Pb zircon crystallization dates from the quartzofeldspathic gneiss (Aqfg). 15DP-A01 are highly discordant, which may indicate multiple lead loss events since initial crystallization. Discordant dates suggest the presence of an ~2700 Ma or older age population. Cramer (2014) and Jones (2008) documented a crystallization age of ~2770 Ma (or older) and a metamorphic age of ~2450 Ma from U-Th-Pb dating of zircons and monazites from the quartzofeldspathic gneiss elsewhere in the Ruby Range. B) U-Th-Pb dates of detrital zircons from a sample of the Flathead Sandstone (Cf, 15DP-A02) directly above the nonconformity at Ashbough Canyon, do not display the regionally prevalent ~1780 Ma age-peak seen in other middle Cambrian units in the northern Rockies (May et al., 2013) and instead show two prominent age-peaks at ~2501 Ma and ~2798 Ma, which may suggest a local provenance.

INTRODUCTION
The Ashbough Canyon quadrangle was mapped during the summer of 2016 as a part of a M.S. thesis at Idaho State University. It was funded by the USGS EDMAP program (#G16AC00159).

GEOLOGIC SUMMARY
The oldest rocks exposed in the area are in the southern Ruby Range and central Blackfoot Mountains and include ortho- and paragneisses of likely Archean age. The structurally deepest rocks are a quartzofeldspathic gneiss (the Dillon gneiss of Heinrich, 1960), with apparent screens of metasedimentary rocks. U-Th-Pb zircon data from quartzofeldspathic gneisses at Ashbough Canyon and elsewhere in the Ruby Range, suggest an intrusive age of ~2700 Ma or older, and the occurrence of a metamorphic event at ~2450 Ma referred to as the Tendency orogeny (Jones, 2008; Cramer, 2015; this study) (Figure 1A). These quartzofeldspathic rocks are structurally overlain in the northwestern Ruby Range by paragneisses, schists, and marbles contained within the Christensen Ranch Metasedimentary Suite (Acr) (Karasevich et al., 1981). Foliation data from the quartzofeldspathic gneiss (Aqfg) and the Christensen Ranch Metasedimentary Suite (Acr) are nearly identical, indicating that they were both metamorphosed during the Big Sky orogeny (Figure 2) (Cramer, 2015). Isoclinal folds, with axial surfaces that are parallel to these foliations were identified at the outcrop scale and used to infer the geometry of regional-scale folds.

In the central Blackfoot Mountains, in the southwestern map area, metamorphic rocks are overlain nonconformably by Middle Cambrian through Mississippian sedimentary rocks that dip gently northward. The Upper Mississippian rocks are intensely folded and deformed above the contact between the Kibbey Sandstone (Mk) and the Lombard Limestone (Ml). Prior mapping in the Lombard Limestone (Ml) showed many of these folded locations as thrust faults, meant to indicate the location of fault propagation folds related to Sevier-style shortening (Pecora, 1981; Tysdal, 1988a).

A Pliocene basalt is also exposed in the northwestern Ruby Range, and overlies Christensen Ranch Metasedimentary Suite (Acr) rocks and related marbles (Ams) (James, 1990).

Quaternary surficial deposits constitute a large portion of the mapping area. Three episodes of alluvial fan formation have been identified based on their stratigraphic relationship to other Quaternary units. The oldest alluvial fan is deposited in the northwestern corner of the map and is heavily obscured, buried, and incised by all other Quaternary units. The two younger fan surfaces (Qaf and Qafy) were identified based on the gradient of their surfaces, the amount of incision by creeks (Qat), and the relationship with Blacktail Deer Creek. The oldest alluvial fan (Qafo) surface is incised by the active Blacktail Deer Creek, which is the site of active deposition of alluvium (Qat). Quaternary fans (Qaf) contain material shed by the northeastern flank of the Blackfoot Mountains. Active Quaternary terrace (Qat) deposits are formed through these fans and carry material to the Blacktail Deer Creek.

Structure
The Ashbough Canyon quadrangle is located on the boundary between thin-skinned, Sevier-style thrusting and basement-involved, Laramide-style deformation (Schmidt and Garhan, 1983; Tysdal, 1988b). Prior work in the region recognized the northeast-dipping, Laramide-style, Jake Canyon reverse fault (Pecora, 1981; Tysdal, 1988a), as juxtaposing Archean quartzofeldspathic gneiss (Aqfg) over Paleozoic strata (Acharf, 1981).

Abundant folds are present in Mississippian Lombard Limestone (Ml). Stratigraphically lower Cambrian through Mississippian units did not accommodate major shortening, which indicates decoupling between structurally higher and lower levels. This is interpreted to indicate a decollement horizon at the base of the Lombard Limestone (Ml) related to the Sevier-style shortening in southwestern Montana. This decollement horizon was mapped as a thrust fault in the map area.

The northeast-dipping Jake Canyon reverse fault merges along-strike to the north into the northeast-dipping, normal-slip, Basin and Range extensional province, and was previously suggested to be active, with activity concentrated along the southern Blackfoot Mountains. This suggests that the Blacktail fault is likely a reactivated fault. The Blacktail fault occurs within the northern Basin and Range extensional province, and was previously suggested to be active, with activity concentrated along the southern Blackfoot Mountains. This suggests that the Blacktail fault is likely a reactivated fault. The Blacktail fault occurs within the northern Basin and Range extensional province, and was previously suggested to be active, with activity concentrated along the southern Blackfoot Mountains.

PREVIOUS MAPPING
Portions of the Ashbough Canyon quadrangle have been mapped by Klepper (1950) and Scholten et al. (1955). More recent mapping includes work on the gneisses in the Ruby Range by Garhan (1979), and Karasevich et al. (1981), and in the Blackfoot Mountains by Clark (1987). The Blackfoot Mountains were mapped by Pecora (1981) (1:24,000) with a focus on the Mississippian stratigraphy, and by Tysdal (1988a) (1:24,000), who focused on the interaction between the Sevier and Laramide deformation in the region. The Paleozoic unit thicknesses within the description of map units are taken from Tysdal (1988a). The most recent published map of the region is by Ruppel et al. (1993), at the 1:250,000-scale.

DESCRIPTION OF MAP UNITS
Qal Alluvium (Holocene)—Unconsolidated gravel, sand, silt, and clay in channels of modern rivers and streams. Classes generally subrounded to well-rounded. Thickness varies but is generally less than 10 m (33 ft). Primarily deposited along the edges of the Blacktail Deer Creek. Alluvial surfaces are heavily obscured and has been buried by prograding alluvial fans originating from the Ruby Range as well as from younger alluvial terraces (Qat) in the Blackfoot Mountains.
Qafo Landslide deposit (Holocene and Pleistocene)—Mass wasting deposits of unconsolidated earthflow containing a mixture of Archean and Paleozoic units derived from the Blackfoot Mountains. Identified on the basis of hummocky topography near the mouth of Ashbough Canyon.
Qta Talus deposit (Holocene and Pleistocene)—Boulder- to cobble-sized, angular blocks and debris. Occurs at the bases of cliff-forming Paleozoic units in the Blackfoot Mountains.
Qc Colluvium (Holocene and Pleistocene)—Cobble to silt clasts and soils forming slumps adjacent to hillsides of unconsolidated material in the Ruby Range.
Qat Alluvial-terrace deposit (Holocene)—Boulders, gravels, pebbles, sand, and soils deposited adjacent to drainages that cut through Qaf and Qafy.
Qafy Alluvial-fan deposit, younger than Qaf (Holocene)—Gravel, sand, silt, and clay with sparse boulders in fan-shaped deposits. Unconsolidated clays and soils are derived from adjacent units in both the Blackfoot Mountains and the Ruby Range. Youngest alluvial fan surfaces within the mapping area, which overlies both the older alluvial-fan deposits (Qafo) and the main north-south-trending alluvial fan surface along the Blacktail Deer Creek (Qaf).
Qaf Alluvial-fan deposit (Holocene and Pleistocene)—Boulders, gravels, sand, and silt deposited in fan-shaped deposits. Loosely consolidated deposits formed from clasts derived from the Quartzofeldspathic Gneiss (Aqfg) in the Ruby Range, and clasts of the Archean through Paleozoic rocks in the Blackfoot Mountains.
Qafo Alluvial fan, older than Qaf (Holocene and Pleistocene)—Unconsolidated gravel, sand, silt, and clay deposited in low gradient fan in the northwestern portion of the mapping area. Material is heavily obscured as several ranches and farms have used this surface for their purposes. Surface was identified due to its low elevation, and incision and burial by all other Quaternary units.
Tba Basalt (Cenozoic; Pliocene)—Red to black, porphyritic, basalt. Highly weathered to iron-stained red. Overlies Archean units in the Ruby Range in a roughly north-south oriented lava flow. Thickness is 15 m (49 ft).
Tq Quartz (Cenozoic; Eocene)—White-beige to red, quartz and jasperoid. Replaces quartzofeldspathic gneiss (Aqfg) adjacent to the Jake Canyon fault (Tysdal, 1988a).
Pq Quadrant Sandstone (Pennsylvanian and Upper Mississippian)—Tan to pale-yellow, fine-grained quartz sandstone. Some weathered surfaces have a red to light pink tint. Limited exposure on the southeastern edge of the map. The contact between the Quadrant Sandstone and underlying Conover Ranch Formation is sharp and conformable. Thickness is 210 m (690 ft).
Mcr Conover Ranch Formation (Upper Mississippian)—Red to beige, very fine- to fine-grained, well to moderately-sorted quartz sandstone. Lower exposure of this unit is a matrix-supported conglomerate containing small pebbles of chert, limestone, and lithic fragments ranging from 0.3-4 cm. Unit forms poorly exposed outcrops on low gradient slopes. Lower contact is sharp and unconformable with the underlying Lombard Limestone. Thickness ranges from 6.9 m (20-30 ft).
Mlb Lombard Limestone (Mississippian)—Upper yellow-tan to beige, fossiliferous, micritic limestone, and tan-beige, micritic limestone, with calcareous shale interbeds, thin- to thick-bedded, thickness 210 m (690 ft), and lower gray to tan-gray micritic limestone, medium-bedded to massive, thickness 140 m (500 ft). Upper part forms the cliffs and talus slopes adjacent to Mount Ashbough and contains flat, horizontal calcite veins up to 50 cm thick, with brachiopods and crinoids. Lower part locally forms cliffs with occasional micritic fine to medium sand-sized fossil layers ranging from 1-4 cm thick, but in the southeastern portion of the map, the unit becomes very subbed and is exposed in limited locations within low grassy topography. In contrast to the underlying largely undeformed Kibbey Sandstone, the Lombard Limestone is highly folded. The lower contact with the Kibbey Sandstone is thus interpreted to be a decollement (i.e., bedding-parallel fault) horizon. Total thickness is at least 350 m (1152 ft).
Mk Kibbey Sandstone (Mississippian)—Tan to yellow, very fine- to fine-grained, well-sorted quartz sandstone, thin-bedded. Lower sandstone contains black chert grains. Exposure of unit is very limited in the field area. Contact is sharp and conformable with the underlying Mission Canyon Limestone. Thickness is ~30 m (100 ft).
Ml Mission Canyon Limestone (Mississippian)—Gray, micritic, fossiliferous limestone, thin- to medium-bedded, with interbedded gray, micritic to crystalline limestone, and tan-beige calcareous siltstone, thin-bedded. Commonly slope-forming and weathers to orange, black, and purple. Upper 35 m of unit has 1-5 mm thick lenses of brown to gray calcareous shale. Unit erodes a field small when broken. Fossils found throughout the unit are commonly in discrete layers (1-4 cm thick) and include crinoids (<1 mm), minor fusulinids, brachiopods (>2 mm), and rugosan corals. Contact with underlying Jefferson is not observed but is thought to be conformable. Thickness is 220 m (720 ft).
Dj Devonian
Cpl Cambrian
Cp Cambrian
Cm Cambrian
Cw Cambrian
Cf Cambrian
Ydia Mesoproterozoic
Aqfg Archean
Acr Christensen Ranch Metasedimentary Suite
Ams Archean
Am Archean

Figure 2. Stereograms showing the poles to foliations of gneisses in the Ruby Range. Kamb contours for the poles to foliation utilize a contour interval of five with deeper colors indicating higher contours. A) Poles to foliation in the quartzofeldspathic gneiss (Aqfg) define an average pole that plunges at 41°, with a trend of 137°. B) Poles to foliation in the Christensen Ranch Metasedimentary Suite (Acr) define an average pole that plunges at 37°, with a trend of 140°.

These stereograms suggest that the Christensen Ranch Metasedimentary Suite (Acr) and quartzofeldspathic (Aqfg) gneisses have statistically indistinguishable foliation orientations and reflect one deformational event, the orientation and timing of deformation constrained for similar rocks to the north (Harms et al., 2004) suggests that all units in the Ruby Range were metamorphosed together during the ~1.78-1.72 Ma Big Sky orogeny.

Three Forks Formation and Jefferson Formation undivided—Poorly exposed in the map area. Total thickness is 54 m (180 ft).
Three Forks Formation (Lower Mississippian and Upper Devonian)—Gray-blue calcareous shale. Limited exposure in the field area, observed as float above cliffs of the Pilgrim Dolomite, and buried Jefferson Formation. Contact with underlying Jefferson Formation is thought to be unconformable (Pecora, 1981).
Jefferson Formation (Upper Devonian)—Yellow-beige to red to gray-tan when weathered, sugary dolomite with interbeds of fine calcareous shale, fine- to medium-bedded. Forms small outcrops. Limited exposure near the mouth of Weston Canyon and on the southern boundary of Ashbough Canyon. Lower contact is not exposed but is thought to be unconformable with the underlying Pilgrim Dolomite (Pecora, 1981).
Pilgrim Dolomite (Upper Cambrian)—Gray to pink, fine- to medium-grained, sugary dolomite, medium- to thick-bedded. Forms large cliffs. Lower contact is concealed but is thought to be conformable with the underlying Park Shale. Thickness is 60 m (200 ft).
Park Shale (Middle Cambrian)—Green-gray to gray-tan, argillaceous and micaceous shale, thin- to medium-bedded. Poorly exposed slope-former, observed as float between cliffs of the Meagher and Pilgrim Dolomites. Contact with the underlying Meagher Dolomite is thought to be conformable. Thickness is 30 m (100 ft).
Meagher Dolomite (Middle Cambrian)—Orange to light-pink dolomite that is fine to medium crystalline, medium- to thick-bedded. Exhibits tan to red, mottled texture, oriented roughly perpendicular to bedding and interpreted to result from bioturbation (Thomas and Roberts, 2007). Forms prominent cliffs near Ashbough Canyon. The upper 17 m is orange to gray, and contains minor, gray to green, shale interbeds. Upper layers also display through cross-beds. The underlying contact with the Wolsley Shale is not exposed but is thought to be conformable and gradational (Pecora, 1981). Thickness is 175 m (575 ft).
Wolsley Shale (Middle Cambrian)—Black, gray, and olive-green argillite and micaceous shale, with minor gray silt. Poorly exposed in the mapping area, observed as float between the Flathead Sandstone and the base of cliffs of Meagher Dolomite. Conformable contact with the underlying Flathead Sandstone. Thickness is 24 m (80 ft).
Flathead Sandstone (Middle Cambrian)—Upper light yellow to tan-gray, fine- to medium-grained, moderately to poorly sorted subarkose, arkose, and quartz arenite and quartzite about 9 m (30 ft) thick, and lower maroon to pink, fine- to coarse-grained arkosic sandstone and pebble conglomerate, with 1-5 mm sub-angular to angular quartz and feldspar clasts, about 0.6 m thick (2 ft), medium-bedded. Through cross-bedding is present in the upper sections. Contact with underlying quartzofeldspathic gneiss is sharp and nonconformable, with underlying gneisses dipping 35-40° to the northeast beneath the contact. Detrital zircons separated from basal sandstone indicate derivation from Archaean sources (Figure 1B). Thickness ranges from 6 m (20 ft) to 25 m (82 ft).
Diabase (Mesoproterozoic)—Red-black, aphanitic, dike-like. Forms a tabular, northwest-southeast striking body that intrudes quartzofeldspathic gneiss (Aqfg) and marble (Am) within the Ruby Range. Previous workers have suggested it was emplaced during a regional event around ~1.4 Ga (Wooden et al., 1978; James, 1990).
Quartzofeldspathic Gneiss (Archean)—Includes various quartzofeldspathic gneisses as well as pegmatite, amphibolite, and diorite dikes and sills. Was originally mapped as the Dillon Granite Gneiss (Heinrich, 1960). However, later mapping suggested a sedimentary (Karasevich, 1981) or mixed igneous and sedimentary protolith (James, 1990). Recent work has suggested that this unit was initially a granitic intrusion that crystallized ~2700 Ma (Jones, 2008; Cramer, 2015; this study). Here, gneisses of predominantly quartzofeldspathic composition were mapped separately from apparent screens of marble and associated schist.
Hornblende-garnet-biotite-plagioclase-quartz-microcline gneiss: White-gray to red-pink, medium-grained, moderately foliated gneiss of granitic composition. Pb-Pb zircon crystallization and U-Th-Pb monazite metamorphic ages obtained by Jones (2008), Alcock and Muller (2012), Cramer (2015), and from this study (Figure 1A) indicate likely initial crystallization of the protolith of the orthogneiss at ~2.7 Ga, followed by multiple episodes of metamorphism at ~2.4-2.5 Ga (Tendency orogeny) and 1.8-1.7 Ga (Big Sky orogeny).
Garnet-biotite-quartz-microcline gneiss: White-gray, fine-grained, moderately foliated gneiss. Lithology is commonly observed in the flat-lying areas of the Ruby Range, outcrops display north-west-trending isoclinal folds.
Biotite-quartz-plagioclase-microcline gneiss: White-gray to beige, medium- to coarse-grained, weakly foliated gneiss of granitic composition.
Quartz-microcline-garnet-biotite gneiss: Black to red-black, medium- to coarse-grained, lightly to moderately foliated gneiss.
Sillimanite-quartz-plagioclase-biotite-microcline gneiss: White-brown to white-gray, fine- to medium-grained, moderately foliated gneiss.
Calcite-quartz-garnet-biotite-microcline schist: Dark gray to black, fine-grained schist. Exposed along the contact between the quartzofeldspathic gneiss (Aqfg) and dolomite marble (Am).
Pegmatite: White to pink, quartz and potassium feldspar-rich veins intruding the other lithologies in the quartzofeldspathic gneiss. Intrudes the contact between the quartzofeldspathic gneiss (Aqfg) and the Christensen Ranch Metasedimentary Suite (Acr).
Amphibolite: Black, hornblende-rich, medium- to coarse-grained amphibolite. Exposed as sills within the quartzofeldspathic gneiss lithologies.
Diorite: Black to dark gray, composed of plagioclase, hornblende, and pyroxene. Dikes and sills intrude the various other lithologies in the Ruby Range.
Gabbro: Black, composed of pyroxene and plagioclase. Exposed as dikes and sills intruding various lithologies in the quartzofeldspathic gneiss, primarily in the Blackfoot Mountains.
Marble (Archean)—Includes dolomitic marble and lesser garnet-chlorite-biotite-hornblende-quartz schist preserved as apparent screens within the quartzofeldspathic gneiss (Aqfg). These rocks may be equivalent to the Christensen Ranch Metasedimentary Suite (Ams).
Dolomitic-marble: White-tan, fine- to medium-grained recrystallized dolomitic marble. Contact with surrounding Aqfg unit is interpreted as intrusive based on occurrence of the marble as apparent screens within the surrounding quartzofeldspathic gneiss (Aqfg). May have the same protolith as Marble (Am) that occurs within the Christensen Ranch Metasedimentary Suite on the western side of the Ruby Range (Acr).
Garnet-chlorite-biotite-hornblende-quartz schist: Black to dark gray, fine-grained schist. Exposed adjacent to the dolomitic marble.
Christensen Ranch Metasedimentary Suite—(James, 1990)
Christensen Ranch Metasedimentary Rocks (Archean?)—Includes metasedimentary gneisses and schists, as well as pegmatite, amphibolite, and diorite sills and dikes. Originally mapped as the Cherry Creek Group (Karasevich, 1981), but renamed by James (1990). One U-Pb monazite age suggests that this unit was deposited prior to ~2553 Ma (Jones, 2008).
Quartz-plagioclase-microcline-sillimanite-biotite gneiss: Gray-tan to white, fine- to medium-grained, moderately foliated gneiss. The gneiss is interlayered with other metasedimentary lithologies found in the Christensen Ranch Metasedimentary Suite (Acr). Contact with the underlying quartzofeldspathic gneiss appears to be intrusive, however the contact is obscured by pegmatite and amphibolite sills.
Quartz-sillimanite-biotite-garnet schist: White-tan, fine-grained, aluminous schist.
Pegmatite: White-tan, coarse crystalline, quartz-rich pegmatite. Occurs as sills and dikes that intrude the gneisses, schists, and marble of the Christensen Ranch Metasedimentary Suite (Acr). Some outcrops contain large (1-3 cm thick) biotite books. Some pegmatite dikes display a foliation that is concordant with the regional north-west-trending foliation, indicating they were intruded prior to or during deformation in the Big Sky orogeny (1.71-1.8 Ga) (Jones, 2008; Cramer, 2015).
Amphibolite: Black, medium- to coarse-grained, hornblende-rich amphibolite. Exposed as sills and dikes.
Diorite: Black, fine- to medium-grained diorite sills.
Christensen Ranch Marble (Archean?)—White, white-tan, medium- to coarse-grained, calcitic marble. This marble is part of the Christensen Ranch Metasedimentary Suite (Acr), but was mapped separately (Karasevich, 1981).

REFERENCES
Acharf, J.A., 1981. Folding and faulting in the northern Blackfoot Range, Beaverhead County, Montana. University of Montana, M.S. thesis, 64 p.
Alcock, J., & Muller, P., 2012. A Paleoproterozoic sedimentary basin within the Wyoming craton exposed in the Ruby Range, SW Montana. Montana State University, M.S. thesis, 64 p.
Clark, M.L., 1987. Protholith and tectonic setting of an Archean quartzofeldspathic gneiss sequence in the Blackfoot Mountains, Beaverhead County, Montana. Montana State University, M.S. thesis, 64 p.
Cramer, M., 2015. Proterozoic tectonometamorphic evolution of the Ruby Range, SW Montana, USA: Insights from phase equilibria modeling and in situ monazite geochronology. University of Montana, M.S. thesis, 79 p.
Garhan, J.M., 1979. Geology and structure of the central Ruby Range, Madison County, Montana. Bulletin of the Geological Society of America, v. 90, p. 695-788.
Harms, T.A., Brady, J.B., Burger, H.R., and Cheney, J.T., 2004. Advances in the geology of the Tobacco Root Mountains, Montana, and their implications for the history of the northern Wyoming province. In: Cheney, J.T., and Harms, T.A., eds., Precambrian Geology of the Tobacco Root Mountains, Montana. Geological Society of America Special Paper, v. 337, p. 227-243.
Heinrich, E.W., 1960. Geology of the Ruby Mountains and nearby areas in southwestern Montana. In: Pre-Beltian geology of the Cherry Creek and Ruby Mountains areas, southwestern Montana. Montana Bureau of Mines and Geology Memoir, v. 38, p. 31-62.
James, H.L., 1990. Precambrian tectonics and folded igneous rock deposits of the southwestern Ruby Range, Montana. United States Geological Survey Professional Paper, v. 1495, p. 1-39.
Jones, C., 2008. U-Pb geochronology of monazite and zircon in Precambrian metamorphic rocks from the Ruby Range, SW Montana: Deciphering geological events that shaped the NW Wyoming province. Kent State University, M.S. thesis, 119 p.
Karasevich, L.P., Garhan, J.M., Dahl, P.S., and Okuma, A.F., 1981. Summary of Precambrian metamorphic and structural history, Ruby Range, southwest Montana. In: Montana Geological Society field conference and symposium guidebook to southwest Montana, p. 225-237.
Klepper, K.A., 1950. A geologic reconnaissance of parts of Beaverhead and Madison Counties, Montana. United States Geological Survey Bulletin, v. 969-C, p. 55-85.
May, S.R., Gray, G.G., Summa, L.L., Stewart, N.R., Gehrels, G.E., and Pecha, M.E., 2013. Detrital zircon geochronology from the Big Horn Basin, Wyoming, USA: Implications for tectonostratigraphic evolution and paleogeography. Geological Society of America Bulletin, v. 125, p. 1403-1422.
Pecora, 1981. Bedrock geology of the Blackfoot Mountains, south-western Montana. Wesleyan University, M.S. thesis, 158 p.
Ruppel, E.T., Lopez, D.A., and O'Neill, J.M., 1993. Geologic map of the Dillon 1° x 2° quadrangle, Idaho and Montana: 1:250,000-scale. Schmidt, C.J., and Garhan, J.M., 1983. Laramide tectonic development of the Rocky Mountain foreland of southwestern Montana. In: Lowell, J.D. and Gries, R., eds., Rocky Mountain foreland basins and uplifts: p. 271-294.
Thomas, K.C., and Roberts, S., 2007. A summary of the stratigraphy and depositional setting of Paleozoic rocks in the Dillon area. Northwest Geology, v. 36, p. 35-56.
Scholten, R., Keenon, K., and Kupchik, W., 1955. Geology of the Lima region, southwestern Montana and adjacent Idaho. Geological Society of America Bulletin, v. 66, p. 345-404.
Stickney, M.C., 2007. Historic outcrops and seismicity in southwestern Montana. Northwest Geology, v. 36, p. 167-186.
Stickney, M.C., and Bartholomew, M.J., 1987. Seismicity and late Quaternary faulting of the northern Basin and Range province, Montana and Idaho. Bulletin of the Geological Society of America, v. 97, p. 1602-1625.
Tysdal, R.G., 1988. Geologic map of the northern flank of the Blackfoot Mountains, Beaverhead County, Montana: 1:24,000-scale.
Tysdal, R.G., 1988. Deformation along the northeast side of Blackfoot Mountains salt, southwestern Montana. In: Schmidt, C.J., and Perry, W.J., eds., Intersection of the Rocky Mountain Foreland and the Cordilleran Thrust Belt. Geological Society of America Memoir, v. 171, p. 203-216.
Wardlaw, B., and Pecora, W., 1985. New Mississippian-Pennsylvanian stratigraphic units in southwest Montana and adjacent Idaho. In: W.J. Sandoz ed., Mississippian and Pennsylvanian stratigraphy in southwest Montana and adjacent Idaho. United States Geological Survey Bulletin, v. 1656, p. B1-B9.
Wooden, J.L., Vitaliano, C.J., Koehler, S.W., and Ragland, P.C., 1978. The late Precambrian mafic dikes in the southern Tobacco Root Mountains, Montana - geochemistry, Rb-Sr geochronology, and relationship to the Proterozoic Canadian Journal of Earth Sciences, v. 15, p. 467-479.



MBMG Open-File Report XXX
Geologic Map of the Ashbough Canyon 7.5' Quadrangle, Beaverhead County, Montana

Brandon M. Crawford and David M. Pearson
Idaho State University